

**Force-Detected NMR in a Homogeneous Field: Experiment
Design, Apparatus, and Observations**

Thesis by

Louis A. Madsen

In Partial Fulfillment of the Requirements

for the Degree of

Doctor of Philosophy

California Institute of Technology

Pasadena, California

2002

(Submitted February 19, 2002)

© 2002

Louis A. Madsen

All Rights Reserved

Acknowledgments

A great many people have contributed to my success as a graduate student at Caltech. In a general sense, the most important of these are my wife Christine Kaestle, my parents Ernie and Helen, and my advisor Dan Weitekamp. Christine had the love and durability to come with me to the thick atmosphere of Los Angeles, and to stay with me and enthusiastically support me in times of trial. She contributed immensely to my happiness, well being, and intellectual development at every stage. Her intellectual insights have continually astounded me, and I sometimes even wondered if Dan wanted her as a graduate student.

I have come to increasingly appreciate my parents' teachings on all disciplines of life, including independence, friendliness and forthrightness, intensity and perseverance, interpersonal interactions, sense of humor, and myriad others. They provided me with extremely valuable fodder as a child, such as surrounding me with parks and friends, seemingly limitless machines and tools, and musical training and instruments. They always encouraged me to think through my own path and then do my will, even if it sometimes went against their better judgement.

Dan Weitekamp has been a wonderful source of intellectual interactions in broad areas of science, and many other topics, from skiing and family, to his pet interest in socio-technological topics (*e.g.*, fiber optics to every house, and sweaters over the internet). He has been supportive and stimulating, has demanded excellence at every turn, and has also given me tremendous leeway and shown great faith in my research. I thank him also for recognizing (even on my admission application!) the utility inherent in my lifelong hobby of machine building, notably auto repair and modification, and for showing interest in my musical endeavors at Caltech.

In the Weitekamp lab, I have also had the pleasure of working with some of the smartest and liveliest people I know. Gary Leskowitz and I are basically a match made in heaven as regards scientific research. Our complementary ideas and efforts led to the success of the BOOMERANG project, which will hopefully continue to benefit from our perspectives and experiences. Luckily enough, we have shared a love of jazz.

musicianship, and our meetings in this venue have produced some of my most enjoyable moments at Caltech.

Jim Kempf was my main companion in experiments in the Weitekamp group, and our constant discussions in lab were highly enjoyable and thought provoking. We shared many other tremendous experiences outside research as well: from camping in Yosemite and King's Canyon, to Kickin' Buck soccer, to many evenings of dinner and discussion.

Paul Carson was always friendly and engaging, and always showed me the upper limits of scientific thought. I also have many fond memories of interactions with Len Mueller and John Marohn, and the newer graduate students in our group: Valerie Norton, Bruce Lambert, and Ramez Elgammal, and Mark Butler, who will carry the group torch onward. I would also like to thank undergraduates who participated in BOOMERANG at Caltech: Christophe Maquestiaux, Donna Daigdigan, and Abel Bourbois.

In the area of BOOMERANG collaborations at MDL-JPL, many individuals deserve thanks. Thomas George and Weilong Tang have been with us from the start of microfabrication efforts, and have both been supportive, full of knowledge and ideas, and extremely fun (insert raucous laughter here). Other outstanding cast members were: Amy Chang-Chien, who was effective beyond belief, Kevin King, who taught me microfabrication and helped revise our first gargantuan process, and Kyung-ah Son and Dan Miller, who have shown great interest in BOOMERANG and are carrying on our efforts at MDL. I would also like to thank: Doug Elliot, Emily Wesseling, Demarus Tevuk, Nosang Myung, Sam Elliot, and Lynn Kim.

Professor Jack Roberts provided me with many enjoyable interactions during the course of my teaching assistanceships for Chem 143, and I will remember his enthusiasm and insightfulness always.

I would like to thank my dear friends Pete Mao and Deirdre Scripture-Adams for providing constant and incredible companionship while living in Westwood, and occasional automotive overdoses. Thanks to my great friend Mike Roy for expanding my fabrication skills, helping me with both lab projects and with building my cars, and sometimes for just shootin' the bull. My jazz musicianship was greatly expanded in the cohort of Bill Bing, Gary Leskowitz, Matt Ashman, Jay Bartroff, Rob Peters, Clancy Rowley, Tom Lloyd, Marc Kuchner, and many others. Derek Debe (ya, you betcha!) has

grounded me in good midwestern values, and shown me good times on the slopes and everywhere else. I would like to thank all members of Caltech Rugby Football Club for excellent friendships and for increasing my skill at the game, notably: Calum Chisholm, Al Preston, Steve Callander, Donal Gallagher, James Gleeson, Bob Gingrich, and Matt Trewella. Finally, I would like to thank Richard Duff for being a great friend and neighbor and for giving me a home in these final days.

Abstract

Here I present motivation, experimental progress, and theoretical aspects of the BOOMERANG (*better observation of magnetization enhanced resolution and no gradient*) method of force-detected NMR, a general approach to extending arbitrary NMR experiments to the micron scale and below. Enabling quality of BOOMERANG is that its sensitivity scales much more favorably than traditional inductive detection for small samples. A reduction in the sample size accessible by NMR is strongly motivated by such goals as massively parallel analysis in support of combinatorial chemistry, portability in support of planetary exploration, and the general advantage of highest sensitivity per unit cost.

The key design insight is that the spin-dependent forces are independent of the field homogeneity across the sample. However, throughput is optimized only by providing field homogeneity during detection sufficient to allow coherent control over all target spins in a sample. I present our BOOMERANG design concepts and strategies, which allow detectors with high geometrical efficiency and good prospects for low mechanical dissipation.

The design principles are quantitatively confirmed using a prototype mm-scale spectrometer. Our experimental results, which include proton and fluorine FT-NMR spectra in solids and liquids, heteronuclear J spectra, and liquid-state spin echoes with sub-Hz linewidths, emphasize BOOMERANG's general spectroscopic applicability.

Fabrication of a high-sensitivity spectrometer optimized for 60-micron samples is underway in conjunction with the Microdevices Laboratory (MDL) at the NASA Jet Propulsion Laboratory (JPL). Using state-of-the-art lithography and electrodeposition

techniques, we have fabricated magnets and mechanical oscillator structures that show promise for incorporation into spectrometers for *in-situ* planetary exploration, and for massively parallel analysis.

As the sample size decreases, sensitivity is dominated by quantum-statistical noise in the sample, or spin noise. This fundamental problem is mitigated by the CONQUEST measurement paradigm involving multiple time-correlated measurements on a spin system of interest. This is an essential ingredient in converting polarization fluctuations to coherent time-domain spectroscopy or to images with arbitrary numbers of spins in each pixel.

Table of Contents

<i>Acknowledgments</i>	<i>iii</i>
<i>Abstract</i>	<i>v</i>
<i>Table of Contents</i>	<i>vii</i>
<i>Standard Symbols, Terms and Abbreviations</i>	<i>x</i>
<i>List of Figures</i>	<i>xii</i>
<i>List of Tables</i>	<i>xiii</i>
<i>Chapter 1: BOOMERANG Force-Detected NMR in a Homogeneous Field</i>	<i>1</i>
1.1 Traditional Nuclear Magnetic Resonance Spectroscopy.....	1
1.2 Force-Detected NMR in a Homogeneous Field.....	4
1.2.A Introduction to Force-Detected NMR.....	4
1.2.B Spin-Dependent Forces and Mechanical Oscillators.....	6
1.2.C Homogeneous-Field Magnet Assembly BOOMERANG.....	10
1.2.D Encoding Time-Domain NMR into Mechanical Oscillations.....	14
1.2.E Sensitivity and Scaling: BOOMERANG and Inductive NMR.....	18
1.2.F Mechanical Dissipation.....	22
1.2.G BOOMERANG for Microscale and Nanoscale NMR.....	27
1.3 BOOMERANG-Related Concepts and Instrumentation.....	30
1.3.A BOOMERANG Magnetometry.....	30
1.3.B Spin Noise and the CONQUEST Measurement Paradigm.....	32
References.....	38
<i>Chapter 2: Design of Millimeter-Scale and Micron-Scale BOOMERANG Instruments</i>	<i>43</i>
2.1 Composite Magnet Assembly for Optimal NMR Detection.....	43
2.1.A Detector Magnet for Optimal Detection Sensitivity.....	45
2.1.B Homogeneity, Forces, and Practical Manufacture.....	47
2.1.C Finite-Element Method Calculations for Optimal Field Homogeneity.....	50
2.1.D Negative Magnetic Spring Constant.....	51
2.1.E Permanent Magnet Shims.....	53

2.2 Mechanical Oscillator Structures.....	54
2.2.A Loaded Beams and Plates.....	55
2.2.B Oscillator Suspension Materials.....	57
2.2.C Oscillator Feedback Transducer.....	58
2.2.D Oscillator Design Procedure: A Force Balancing Act.....	62
2.2.E Vibration Isolation.....	64
2.2.F Alternate Mechanical Oscillator Forms	65
2.3 Oscillator Displacement Measurement.....	66
2.3.A Fiber-Optic Interferometry.....	67
2.3 B Transverse Fiber-Optic Interferometry.....	72
2.3.C Other Displacement Sensing Methods.....	73
2.4 Rf Excitation and Data Collection.....	75
2.4.A Rf Excitation System.....	75
2.4.A Data Collection System.....	76
References.....	78

Chapter 3: The Prototype BOOMERANG Spectrometer and Experimental Observations.....	81
---	-----------

3.1 Spectrometer Assembly and Functionality.....	81
3.1.A B_0 Field Permanent Magnets and Spectrometer Supports.....	83
3.1.B Detector Oscillator and Ring Magnet Assembly.....	84
3.1.C B_0 Field Shimming.....	87
3.1.D Fiber-Optic Interferometer and Fiber Position Feedback.....	89
3.1.E Rf Excitation System and Coil.....	92
3.1.F Data Collection System.....	97
3.1.G Vacuum System.....	100
3.2 Experimental Methods and Observations on 3 mm Samples.....	100
3.2.A Measuring Oscillator Resonances.....	101
3.2.B Mechanical Oscillator Dissipation Studies.....	104
3.2.C Thermal-Noise-Limited Detection.....	106
3.2.D Efficient Cyclic Inversion: Adiabatic Rapid Passage and Variants.....	107
3.2.E Continuous-Wave (CW) NMR Experiments.....	113
3.2.F Nutation to Determine Rf Field Strength.....	115
3.2.G Inversion-Recovery Determination of T_1	116
3.2.H Fourier-Transform NMR Spectroscopy.....	117
3.2.I Spin Echoes, Echo Trains, and Use of Composite Pulses.....	118
3.2.J Heteronuclear Echo Trains: J Spectroscopy.....	120
References.....	122

<i>Chapter 4: Fabrication of a BOOMERANG FDNMR Spectrometer for Micron-Scale Samples.....</i>	125
4.1 Fabrication Goals and Reasonable Expectations	125
4.2 Microfabrication Methods Overview.....	129
4.2.A. Basic Concepts in Microfabrication.....	129
4.2.B. General Comments on the Culture of Microfabrication and Science.....	136
4.3 BOOMERANG Microfabrication Process Overview.....	139
4.3.A. Fabrication Process with Two-Step Magnet Deposition.....	140
4.3.B. Simplified Fabrication Process with Single-Step Magnet Deposition	142
4.4 The Refined Microfabrication Process: A Detailed Description.....	144
4.4.A. Double-Side Alignment.....	145
4.4.B. Wafer Trench Etching and the Projection Aligner.....	147
4.4.C. Oxide Sacrificial Layer Definition.....	151
4.4.D. Magnet Patterning and Electrodeposition.....	157
4.4.E. Beam and Buttress Definition.....	165
4.4.F. Final Release.....	173
4.4.G. Concluding Remarks on Processing.....	176
4.5 Microfabrication Results and Testing of BOOMERANG Oscillators.....	176
4.5.A Silicon Oscillator Beams Without Magnets.....	176
4.5.B Device Structures.....	177
4.5.C MEMS Oscillator Testing Apparatus.....	179
4.6 A Proposed Spectrometer Assembly.....	181
References.....	184

<i>Appendix A Additional Experimental Hardware Descriptions and Diagrams.....</i>	186
---	-----

<i>Appendix B BOOMERANG Microfabrication Process Flow.....</i>	192
--	-----

Standard Symbols, Terms, and Abbreviations

NMR	nuclear magnetic resonance
FDNMR	force-detected nuclear magnetic resonance
FT	Fourier transform
ARP	adiabatic rapid passage
EMF	electromotive force
FOI	fiber-optic interferometer
TFOI	transverse fiber-optic interferometer
rf	radiofrequency
rpm	revolutions per minute
TIA	transimpedance amplifier
FWHM	full width at half max
PR	photoresist
DI	deionized
IPA	isopropyl alcohol
TCE	trichloroethylene
Oxide	silicon dioxide (SiO_2)
Stepper	photolithography projection aligner
RIE	reactive-ion etching
DRIE	deep reactive-ion etching
BOE	buffered oxide etchant
CVD	chemical vapor deposition
PECVD	plasma-enhanced chemical vapor deposition
e-beam	electron beam
NiFe	nickel-iron (alloy)
CoNiFe	cobalt-nickel-iron (alloy)

Constants and Parameters

B_0	static magnetic field in NMR experiments
B_1	rf magnetic-field amplitude in NMR experiments
ω_0	nuclear Larmor frequency (rad s^{-1})
γ	nuclear gyromagnetic ratio
ω_h	mechanical oscillator resonance frequency (rad s^{-1})
ν_h	mechanical oscillator resonance frequency (Hz)
ν_h	mechanical oscillator driving frequency (Hz)
τ_h	mechanical oscillator exponential ringdown time
Q_h	mechanical oscillator quality factor
γ_h	full-width at root-half max of the oscillator amplitude resonance, or FWHM/2 of the energy resonance (Hz)

M_z	nuclear spin magnetization
T_1, T_2	time constants of longitudinal and transverse nuclear spin relaxation
T_{1a}	intrinsic time constant of spin relaxation during ARP cyclic inversion
T'_{1a}	observed time constant of spin relaxation during ARP cyclic inversion
T_{1p}	time constant of relaxation of nuclear alignment along a spin-locking axis
t_1	indirect dimension of NMR time evolution in a pointwise-detected experiment
t_2	duration of the cyclic-inversion force detection period
I_x, I_y, I_z	Cartesian components of dimensionless nuclear spin angular momentum operators

Common-Usage Physical Constants

ϵ_0	dielectric permittivity of free space
μ_0	magnetic permeability of free space
k_B	Boltzmann's constant
\hbar	Planck's constant divided by 2π
e	unit of electron charge

List of Figures

1.1.1 - Basic NMR Physics and Apparatus	1
1.1.2 - Nuclear Magnetization	2
1.1.3 - Time-Domain NMR Signals	3
1.2.1 - Magnetic Force between a Sample and Magnetic Dipoles	7
1.2.2 - Spin-Dependent Mechanical Oscillator Driving	9
1.2.3 - Cutaway of BOOMERANG Force-Detected NMR Spectrometer	11
1.2.4 - Idealized Spherical BOOMERANG Magnet Assembly	12
1.2.5 - Encoding NMR into Mechanical Oscillations	16
1.2.6 - SNR Scaling Comparison	21
1.2.7 - Thermoelastic Damping in Rectangular Beams	25
1.2.8 - Parallel Analysis with BOOMERANG	28
1.2.9 - Transverse Detection using Torsional Nano-Oscillators	29
1.3.1 - BOOMERANG Magnetometer	30
1.3.2 - Spin Noise Dominates NMR Signals at Low N	33
1.3.3 - CONQUEST Measurement Scheme and Sensitivity Predictions	36
2.1.1 - BOOMERANG Detector Assembly	44
2.1.2 - Detector Magnet and Relevant Optimization Parameters	46
2.1.3 - Magnetic Force vs. Detector Magnet Displacement	52
2.1.4 - Static Field Magnet with Shim Magnet	53
2.2.1 - Split-Ring Capacitance Transducer	59
2.2.2 - Capacitive Transducer Force on Oscillator	60
2.2.3 - Capacitive Force Transducer Incorporated into the BOOMERANG Detector	61
2.2.4 - Elastic, Capacitive, and Magnetic Potentials for Oscillator Motion	62
2.3.1 - Fiber Optic Interferometer	67
2.3.2 - Interferometer Fringe vs. Fiber tip-Beam Distance	69
2.3.3 - Transverse Fiber-Optic Interferometer	73
3.1.1 - BOOMERANG Prototype Spectrometer Assembly	81
3.1.2 - Cross-Section of BOOMERANG Prototype	82
3.1.3 - Detector Oscillator and Sample	85
3.1.4 - Rf Excitation System Schematic and Coil Probe	94
3.1.5 - Rf Coil Probe	96
3.1.6 - Oscillator Detection Path Schematic	98
3.2.1 - Harmonic Oscillator Amplitude Response Curve	102
3.2.2 - Oscillator Dissipation Tests with Modified Ring Magnets	105
3.2.3 - Thermal Motion Noise Peak	107
3.2.4 - Phase-Cycled Tangent ARP for Broadband and Efficient Spin Inversion	112
3.2.5 - Continuous-Wave (CW) NMR Spectroscopy	113
3.2.6 - Nutation to Measure Rf Field Strength	115
3.2.7 - Inversion-Recovery Determination of T_1	116
3.2.8 - Compensated Spin-Echo Spectroscopy	119
3.2.9 - Heteronuclear J Spectroscopy	120

4.1.1 - Microfabricated BOOMERANG Detector Element	125
4.1.2 - Proposed Microcoil Excitation Probe for MEMS BOOMERANG Spectrometer	127
4.3.1 – Fabrication Process Summary with Two-Step Plating	141
4.3.2 – Fabrication Process Summary with One-Step Plating	144
4.4.1 – Double-Side Align Marks	146
4.4.2 – Backside KOH Etching Process	149
4.4.3 – Oxide Sacrificial Layer Patterning	153
4.4.4 – Pattern Alignment Failure Modes and Remedies	155
4.4.5 – Magnet Lithography and Electrodeposition	164
4.4.6 – Photolithography for Beam/Buttress DRIE	168
4.4.7 – Beam/Buttress DRIE Process	172
4.5.1 – Silicon Beam and Buttress	177
4.5.2 – Microfabricated BOOMERANG Device Structures	178
4.5.3 – Cross Section of Micro-Oscillator Testing Apparatus	180
4.6.1 – BOOMERANG Micro-Oscillator Detector	181
4.6.2 – Cross Section of Micro-BOOMERANG Spectrometer	183
A.1 - Laser Driver Circuit	186
A.2 - Interferometer Fringe Feedback Circuit	187
A.3 - Single-Sideband Mixer	188
A.4 - External Clock Circuit - Fast TTL Comparator	189
A.5 - Vacuum System for BOOMERANG Spectrometer	191

List of Tables

2.2.1 - Material Properties of Oscillator Suspension Materials	58
3.1.1 - BOOMERANG Prototype Spectrometer Assembly	84
4.4.1 – NiFe and CoNiFe Alloy Electrodeposition Conditions and Film Properties	160
4.5.1 – Theoretical Oscillator Frequency Calculations	177

Chapter 1: BOOMERANG Force-Detected NMR in a Homogeneous Field

1.1 Traditional Nuclear Magnetic Resonance Spectroscopy

Nuclear magnetic resonance (NMR) spectroscopy utilizes the intrinsic spin angular momentum in atomic nuclei as a probe of chemical structure and functionality. A nuclear spin in a magnetic field exhibits a Zeeman energy splitting characterized by a Larmor transition frequency ω_0 . We may describe spins $1/2$ in a magnetic field by two quantum states: Spin “up,” or $+1/2$, is the state with the spin parallel to the magnetic field, and “down,” or $-1/2$, is the state with the spin antiparallel to the field. The Larmor transition (resonance) frequency ω_0 depends linearly on the net magnetic field at the site of a given nucleus, which is influenced both by externally applied magnetic fields, and by particular geometries of electrons and nuclei present in the chemical structure

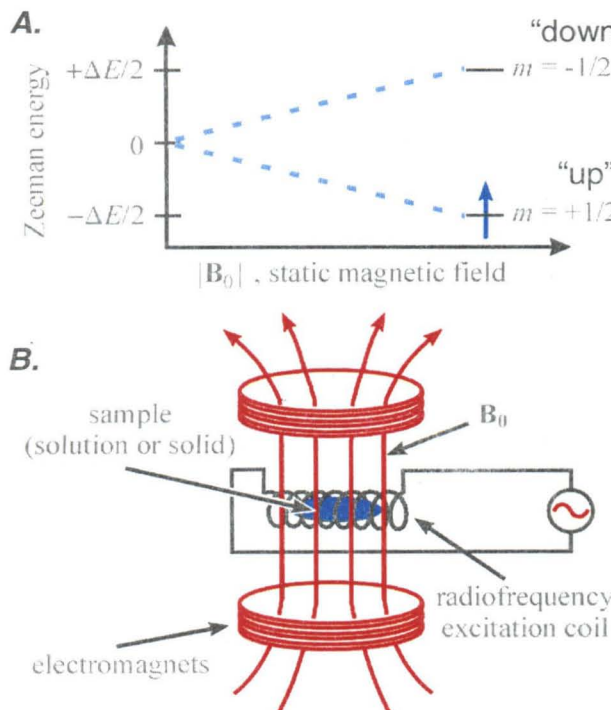


Figure 1.1.1: Basic NMR Physics and Apparatus.

Part A depicts the Zeeman splitting of nuclear spin states when spin-1/2 nuclei are placed in a magnetic field. The energy splitting depends on the gyromagnetic ratio of the nucleus, and linearly on the applied field. The magnetic resonance apparatus in B applies resonant energy to the sample to drive spin transitions. The energy spectrum of the sample spins may be detected by the coil shown, or by other suitable magnetic moment detectors.

surrounding the nucleus. We may elucidate molecular structure information by acquiring the energy spectrum of nuclear spins in a molecule, and interpreting the symmetry and positions of resonance lines in this spectrum. Figure 1.1.1A shows the nuclear Zeeman energy splitting in a magnetic field. In order to observe the nuclear-spin energy spectrum, energy is applied to disturb the spin system and the resulting spin evolution is measured using a suitable magnetic moment detector. Figure 1.1.1.B shows a spin-bearing sample in a static magnetic field produced by electromagnets, and surrounded by an rf coil used to excite spins transitions.

In Fourier-transform NMR (FTNMR) experiments, a short resonant pulse of radiofrequency (rf) magnetic field is applied to the spins in the sample using a coil along an axis perpendicular to the static field. This pulse exerts a torque on the spins, and their

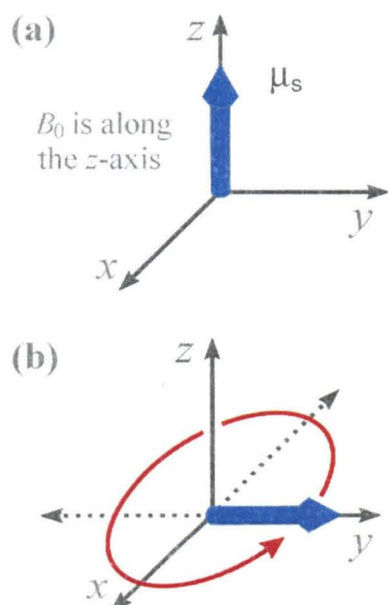


Figure 1.1.2: Nuclear Magnetization. The nuclear energy (Zeeman) splitting and Boltzmann's law determine the net magnetic moment of a spin-bearing sample at equilibrium, which aligns along the z-directed external field in the NMR experiment as shown in part A. After a resonant rf pulse to the spin system, the spins precess about the z axis, as shown in part B.

net magnetic moment μ_s , shown in figure 1.1.2.A, rotates about the applied rf field axis, and then precesses about the static magnetic field axis, as shown in figure 1.1.2.B. In traditional NMR experiments, an inductive coil (usually the same one used for excitation) detects this exponentially decaying Larmor precession, or the “free-induction decay”

(FID), through Faraday's law and yields a voltage signal proportional to $d\mu_s/dt$, as shown in figure 1.1.3. Fourier transforming this time-domain signal gives the energy spectrum of the nuclear spin transitions in the sample. By applying carefully designed sequences of rf pulses to a sample, the spin Hamiltonian may be selectively edited to provide specific chemical or spatial information [1, 2].

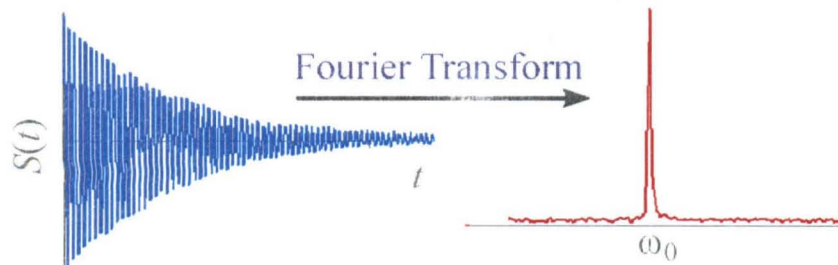


Figure 1.1.3: Time-Domain NMR Signals. Traditionally, we detect the precession depicted in figure 1.1.2 using an inductive coil oriented along one of the transverse-plane axes (x or y). We Fourier transform the NMR "FID" at left to yield the frequency spectrum at right.

Today, multiple-pulse NMR is a non-invasive method of spectroscopy and imaging in solutions and solids with unparalleled flexibility and information content relative to other methods of analysis, such as mass spectrometry, scanning-force microscopies, optical spectroscopy, and X-ray diffraction. The power of NMR as an analytical tool in studies of molecular structure determination and dynamics is largely due to its coherent nature, which allows tremendous flexibility in selectively enhancing or suppressing interactions in a spin system of interest. The homogeneity of the field imposed on the sample is an important factor in determining the degree and the utility of spin coherence in a sample.

The main limitation of NMR has been that of sensitivity. This is due to the low ($\sim 10^{-6}$) fractional polarization afforded by nuclear spin paramagnetism at typical fields and

temperatures, and the relatively low magnetic moment per nuclear spin. Thus, using traditional detection methods, relatively large amounts of sample are needed to conduct detailed analyses. Importantly, sensitivity scales unfavorably for inductive detection with small samples [3].

1.2 Force-Detected NMR in a Homogeneous Field

1.2.A Introduction to Force-Detected NMR

While the detection method of choice for most of the history of NMR has been the above-described induction method of Purcell [4] and Bloch [5], the first method of NMR was a gradient-based method of force detection, the molecular-beam method of Rabi [6]. A torque-detection method was introduced in the 60's by Gozzini, who proposed [7] and demonstrated [8] how torques on a suspended solid sample in a homogeneous field could be used to measure magnetic resonance of samples with very short spin-lattice relaxation times in continuous-wave fashion. Pizarro and Weitekamp [9, 10] proposed to detect ESR and NMR of electromagnetically trapped ions by way of a resonance-induced change in the amplitude of their orbits, an approach with the potential for single-molecule sensitivity even on unpolarized ensembles. Sidles proposed a force-detected method of magnetic resonance using cantilevers and a resonant force between a spin-bearing sample and a gradient-producing ferromagnet [11], which has been experimentally demonstrated with ever-increasing gradients [12-16]. A common aspect of these various recent force-detection methods is the application of the magnetic force resonantly to a harmonic oscillator (*e.g.*, ion motion, suspended sample, suspended magnet) that is well isolated from its surroundings. This increases the interaction time of

the sample with the detector and minimizes thermal noise, which is crucial for measuring weak forces. A historical review of these previous force-detection methods may be found in the Ph.D. Thesis of Garrett M. Leskowitz [17].

Recently, we proposed [3] and demonstrated [18] a new method of force-detected nuclear magnetic resonance (FDNMR) that promises *better observation of magnetization, enhanced resolution, and no gradient* (BOOMERANG) relative to both inductive detection and to other methods of magnetic resonance force detection. BOOMERANG represents a generalized approach to force detection. It is general as regards pulse sequence and sample geometry, and it is independent of the magnetic field gradient across the sample. Our goal is higher sensitivity NMR on small samples, which includes high-throughput parallel analysis of large sample libraries, NMR surfaces studies, and remote sensing with tiny spectrometers.

We have proposed BOOMERANG as a method that will allow application of arbitrary high-resolution multiple-pulse NMR experiments on very small samples [3, 18]. It is based on measurement of small forces between nuclear spin magnetic moments in a sample and a small detector magnet situated near the sample, and thus represents a synergy between modern multiple-pulse NMR and scanning probe methods, such as atomic force microscopy (AFM)[19]. In BOOMERANG, the detector is part of a composite magnet assembly designed to produce field homogeneity throughout the sample while achieving optimal sensitivity to magnetic moments, such as nuclear spins. BOOMERANG exhibits more favorable SNR scaling than traditional inductive detection, so NMR analysis may be extended to smaller samples than those previously accessible.

1.2.B Spin-Dependent Forces and Mechanical Oscillators

We consider the force between a spin-bearing sample and a nearby ferromagnet as arising from the interaction of the dipole moment of the magnet with the dipole moment of the sample. The energy of interaction between two infinitesimal magnetic dipoles can be expressed as the moment of one dipole in the magnetic field of the other. The two equivalent expressions are

$$E = -\mathbf{B}_s(\mathbf{r}_d - \mathbf{r}_s) \cdot \mu_d, \text{ and} \quad 1.2.1A$$

$$E = -\mu_s \cdot \mathbf{B}_d(\mathbf{r}_s - \mathbf{r}_d), \quad 1.2.1B$$

where μ_d and μ_s represent the dipoles of the infinitesimal magnet and sample volume elements at the positions \mathbf{r}_d and \mathbf{r}_s , respectively. $\mathbf{B}_d(\mathbf{r}_s - \mathbf{r}_d)$ and $\mathbf{B}_s(\mathbf{r}_d - \mathbf{r}_s)$ are the magnetic fields due to the ferromagnet and the sample volume elements at distances $(\mathbf{r}_s - \mathbf{r}_d)$ and $(\mathbf{r}_d - \mathbf{r}_s)$, respectively. The force between these two dipoles is given simply by $\mathbf{F} = -\partial E / \partial \mathbf{r} = -\nabla E$, the negative derivative of the potential energy with respect to the relative coordinate \mathbf{r} . More generally, the dipole-dipole energy may be integrated over the sample and detector volumes, and the relevant force will be the negative derivative of this energy with respect to a harmonic oscillator coordinate that comprises the detector mode.

A spherical, uniformly polarized sample produces the same magnetic field as that of a point dipole located at its center. We can now represent the net dipole of the sample as μ_s , which is the same as that for a point dipole. Taking the negative derivative of Equation 1.2.1A with respect to the coordinate \mathbf{r} yields the force \mathbf{F}_d on a magnet dipole element μ_d due to the field of the sample dipole μ_s as

$$\mathbf{F}_d = \frac{\mu_0 \mu_s \mu_d}{4\pi r^4} \left[\cos \theta (9 - 15 \cos^2 \theta) \hat{z} + \sin \theta (3 - 15 \cos^2 \theta) \hat{p} \right]. \quad 1.2.2$$

This force of interaction is illustrated figure 1.2.1.

A static magnetic force exists between these magnetized bodies such that placing a section of the ferromagnet assembly on a flexible suspension allows that magnet section to move toward the sample. Inversion of the sample spin magnetization, *e.g.*, by application of a π rf pulse, would invert the sign of this force and cause the magnet to

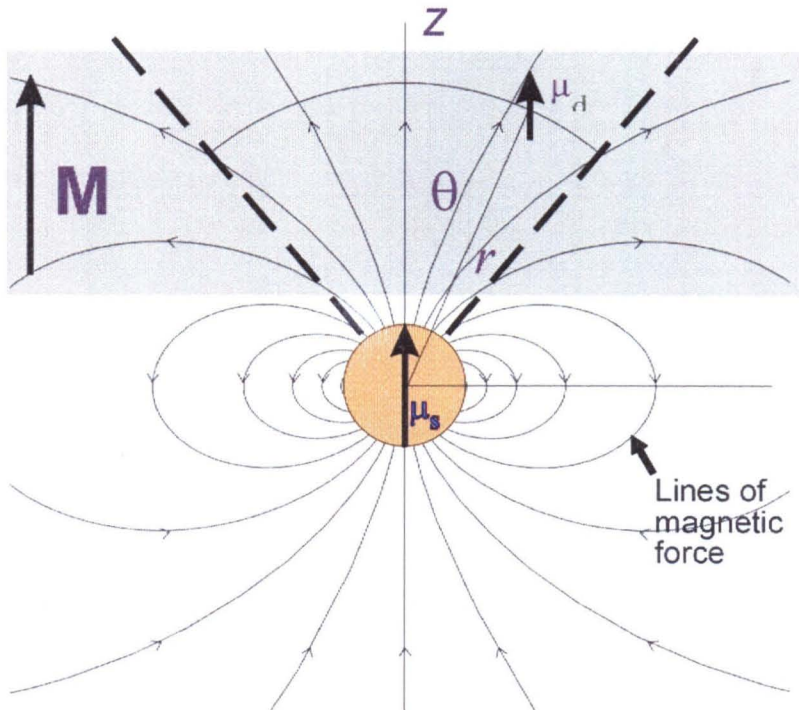
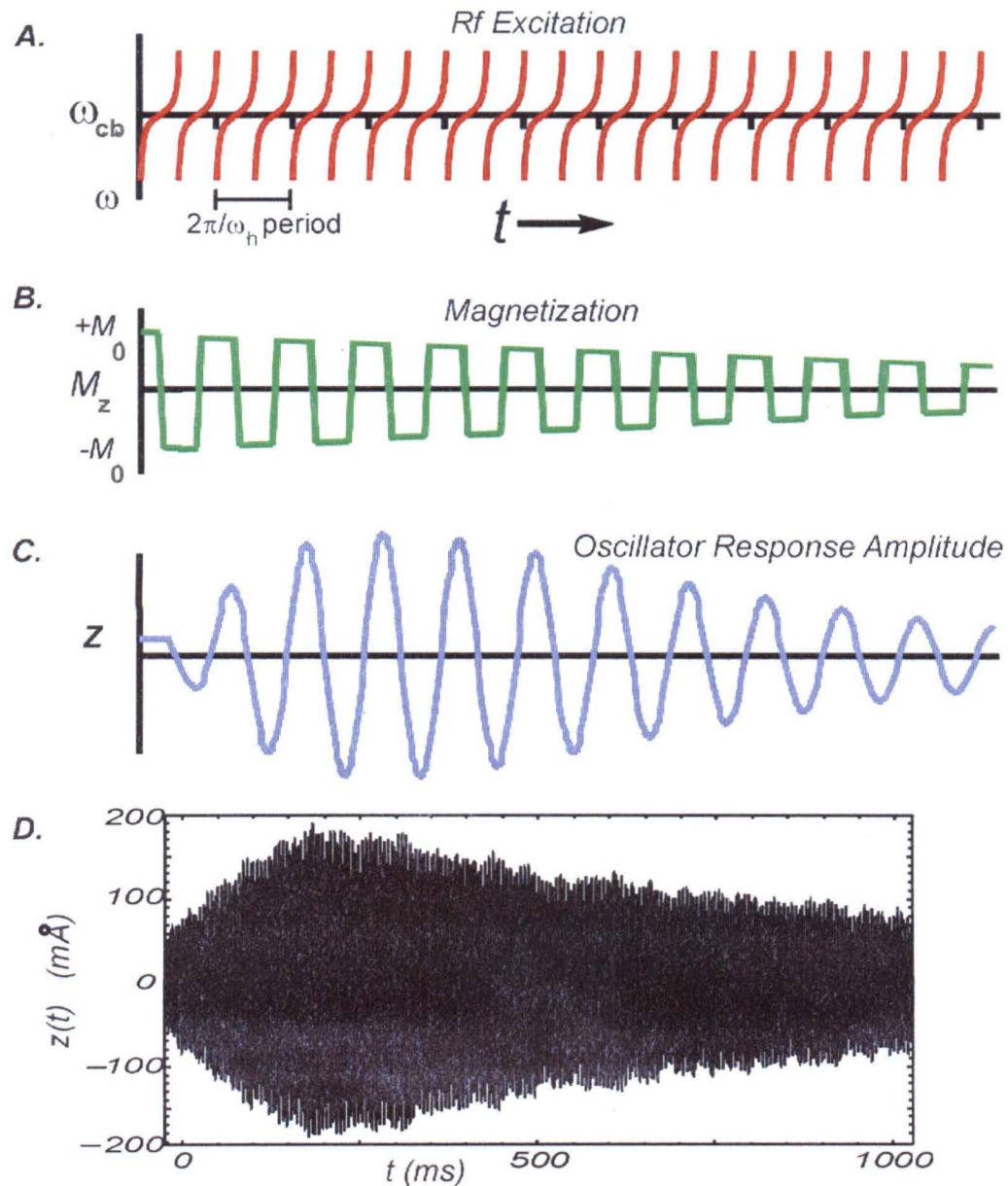


Figure 1.2.1: Magnetic Force between a Sample and Magnetic Dipoles. The gray represents a cross-section of an assembly of z-aligned detector dipoles μ_d at distance r and angle θ from the center of the spherical sample interacting with the sample dipole μ_s . The force \mathbf{F}_m between the two dipoles changes sign at the conical surface with $\theta = \arccos \sqrt{3/5} = 39.2^\circ$, depicted by the heavy dashed line. We use this image as a guide in envisioning novel BOOMERANG detector geometries. I depict the lines of magnetic force produced by the sample when its dipole is aligned along z . A detector magnet designed for optimal coupling to the sample in the z -direction should lie as close to the sample as possible and within the $\theta = 39.2^\circ$ cone.

move away from the sample. These forces are so tiny ($\lesssim 1 \text{ fN}$) that they would be extremely difficult to measure as a dc displacement since the thermal (Brownian) motion of the suspended magnet causes much larger fluctuations in displacement. The key concept in all successful force-detected magnetic resonance methods is that this spin-dependent force must be applied *resonantly* to drive the oscillator at its natural harmonic frequency [3, 10, 20]. By inverting the magnetization of the sample twice per mechanical oscillator period (on resonance), the oscillator rings up to a steady-state amplitude larger than the dc amplitude by approximately a factor Q_h . Figure 1.2.2 shows this oscillator-driving scheme and corresponding oscillator response. The lower the dissipation in the mechanical oscillator, the higher its quality factor Q_h and the longer its ringdown time τ_h , and thus the larger the amplitude of oscillation induced by the spin inversions. Note that the word “resonance” in (nuclear or electron) magnetic resonance refers to resonant transitions between nuclear spin states at MHz – GHz frequencies, and these frequencies are not necessarily directly involved in driving the mechanical oscillator motions, which may be matched to the frequencies of driven oscillations of the spin population differences.

Figure 1.2.2: Spin-Dependent Mechanical Oscillator Driving. A shows the rf frequency sweeps about a centerband frequency ω_{cb} , which produce the cyclic inversions of spin magnetization shown in B. Interaction of the oscillating spin magnetization with the detector magnet resonantly drives oscillator motion, as shown in C. The oscillator response initially follows an exponential growth to “ring up” to a quasi-steady-state amplitude, then decays as M_z relaxes toward an average value of zero. D shows a proton NMR data transient.



1.2.C Homogeneous-Field Magnet Assembly – BOOMERANG

Figure 1.2.3 depicts an experimental realization of a BOOMERANG detector. The ferromagnetic assembly provides a field throughout the sample volume that is nominally homogeneous, and it may be viewed as two cylindrical pole pieces from which the smaller magnets have been carved out. The detector magnet experiences a force that is proportional to the z-component of the sample's magnetization. This magnet is connected to a low-dissipation-material beam, and this composite oscillator exhibits a high-quality harmonic motion along the z-axis. If the magnetization of the sample is modulated at the harmonic frequency of the mechanical oscillator, then the oscillator is driven into resonance. The magnetization is inverted twice per oscillator period by radiofrequency (rf) pulses supplied by the rf coil, and the resulting signal force drives the detector magnet at the resonance frequency of the mechanical oscillator. The whole apparatus is enclosed in a vacuum chamber at ~ 1 mTorr to reduce acoustic noise and viscous atmospheric damping of the oscillator. The sub-angstrom vibrations induced in the oscillator by the force of the sample magnetization are measured by fiber-optic interferometry. The sensitivity of the interferometer as a displacement sensor is below the dominant noise source in the experiment, which is the thermal (Brownian) motion of the harmonic oscillator. This apparatus is thus a sensitive magnetometer - at room temperature, our prototype's sensitivity of $1 \times 10^{-13} \text{ J/T}/\sqrt{\text{Hz}}$ ($1 \times 10^{-11} \text{ emu}/\sqrt{\text{Hz}}$) is 50 times better than that of a commercial SQUID magnetometer operating at 4 K [21]. Magnetometry may be implemented by simply modulating the position of a sample relative to the detector magnet, or otherwise changing the magnetic state of the sample on resonance with the oscillator.

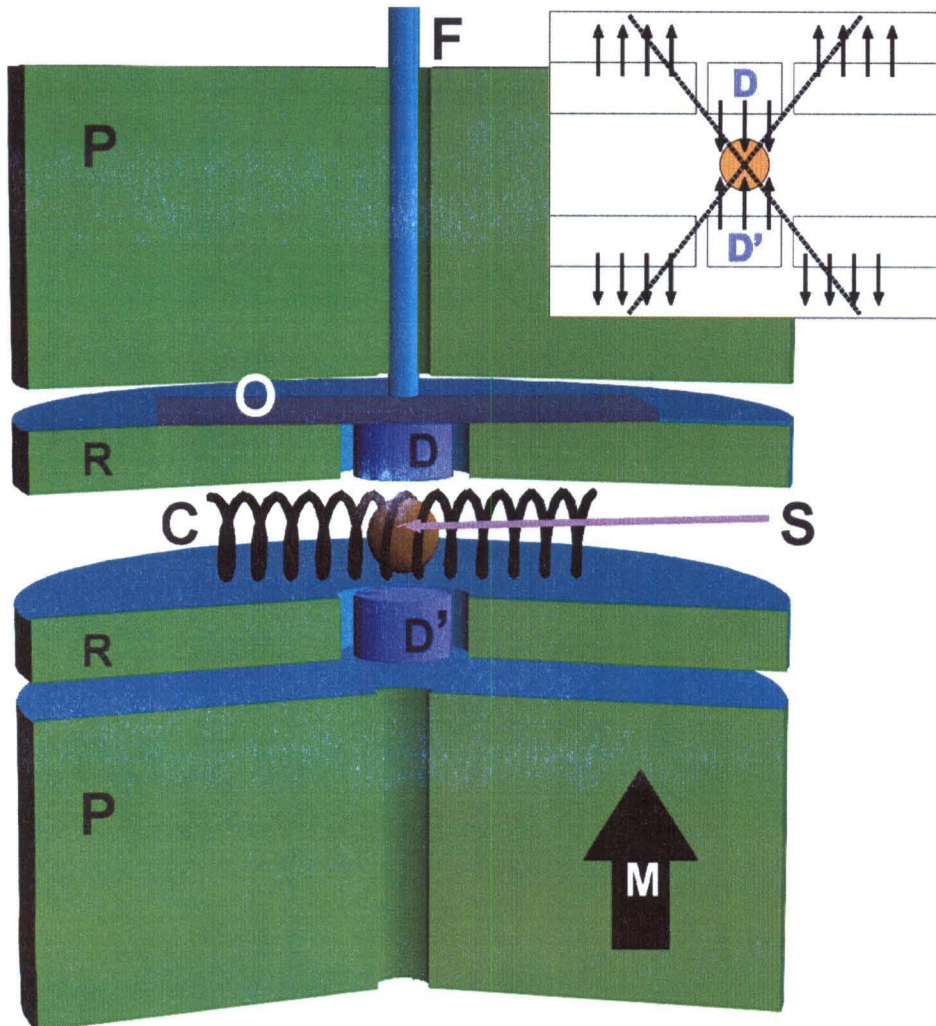


Figure 1.2.3: Cutaway of BOOMERANG Force-Detected NMR Spectrometer. Two NdFeB pole magnets P magnetize a cylindrically symmetric array formed by ring magnets R and detector magnets D and D'. A spherical sample S resides inside coil C, which provides rf pulses to modulate the sample's magnetization. The sum of the magnets, which may be viewed as a pair of pole pieces from which the smaller magnets have been carved out, provides a homogeneous field throughout the sample. One of the detector magnets D is fixed to a single-crystal silicon oscillator O. The inset shows the forces exerted by the sample on the components of the magnet array when the magnetizations of the sample and all the magnets are aligned along vector M. Cyclic inversion of the sample's magnetization induces mechanical oscillations of O, which are detected with fiber-optic interferometer F. Also shown in the inset is a cone-shaped nodal surface where the axial component of the magnetic force vanishes. The cylindrical detector magnet D, optimized for sensitivity, is contained within this cone. A homogeneous external field from, *e.g.*, a cryomagnet may replace the static field generated by the permanent pole magnets P.

Newton's third law implies that the force between the detector magnet and the spin-polarized sample is equal and opposite to the force between the sample and the field-compensating ring magnet. We detect the detector magnet displacement relative to the ring magnet, which is rigidly fixed to the rest of the spectrometer including the displacement sensor, and to the sample. The superposition of the two inhomogeneous fields of the detector and ring magnets along with the fields from their symmetric pair opposite the sample creates a net homogeneous field at the sample.

Figure 1.2.4 shows an idealization of the BOOMERANG detector. Magnetic forces exerted by the sample distort the array in proportion to the sample's magnetization

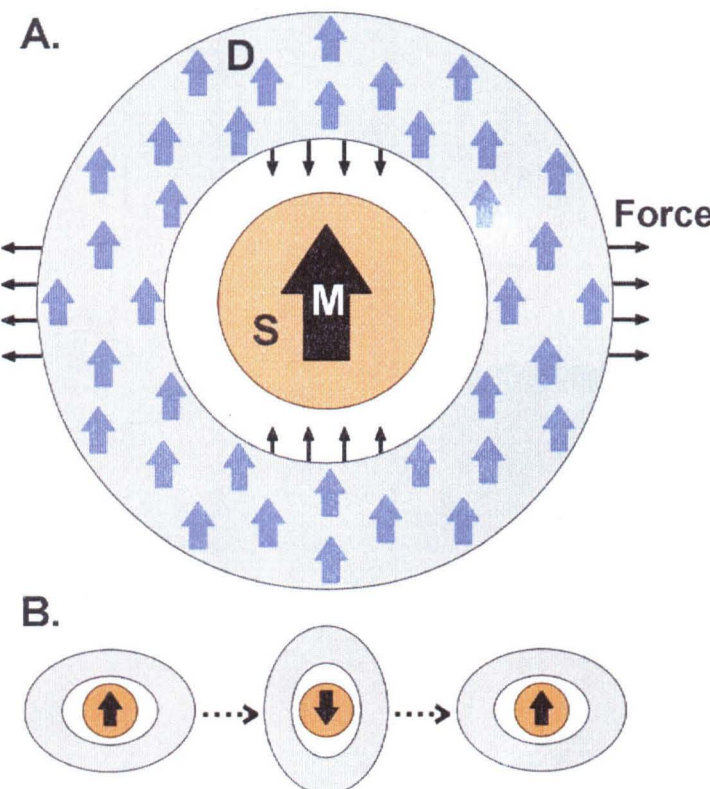


Figure 1.2.4: Idealized Spherical BOOMERANG Magnet Assembly. In A, a flexible spherically symmetric array of detector magnets D surrounds the sample S with magnetization shown by the vector M. Magnetic forces exerted by the sample distort the array in proportion to the magnitude of the sample's magnetization. In B, cyclic inversion of the sample's magnetization at a mechanical resonance frequency of the flexible detector array drives an elliptical "breathing sphere" mode of vibration that is used to measure M. M may be modulated on successive repetitions of the experiment to encode spin dynamics into the mechanical oscillations. The field throughout S remains homogeneous at all times during the elliptical distortions.

M_s . Figure 1.2.4B shows the “squash-and-stretch” mode of vibration that is induced by cyclically inverting M_s . As above, by inverting M_s at the resonance frequency of this mode and measuring the distortion of the magnet array, one may use the device to measure the sample’s magnetization.

This detector configuration is ideal in the sense that the magnetic field produced throughout the sample volume by the magnet assembly is homogeneous at all times, for any oblateness of the array. Field homogeneity is a key feature of BOOMERANG, and it is advantageous for three reasons. First, in NMR, the bandwidth of the spectrum of transition frequencies characterizing the sample is often a very small fraction (a few ppm for proton magnetic resonance in liquids) of the Larmor frequency. Field inhomogeneity present in the detection apparatus can completely obscure the detailed information in chemical shifts and spin-spin couplings, leaving total spin density as the only readily observable quantity.

Second, diffusion of spin-bearing molecules in an inhomogeneous field further enhances irreversible dephasing of the signal. This is especially important with liquid samples, and may also be problematic with samples weakly bound to surfaces. So far, we have measured field homogeneity with BOOMERANG 10^3 times better than that possible using an optimized detector magnet and no field compensation magnets. Since diffusion in a field gradient causes dephasing that scales with $(dB/dz)^2$ [1, 22], this translates into a factor of 10^6 reduction in dephasing for diffusing samples. This dephasing mechanism forces gradient-based methods of force-detection [20] to investigate only solid or frozen samples, dramatically limiting their scope of analysis. For example, in biological problems, freezing removes dynamics and perturbs structures.

Furthermore, BOOMERANG shows promise for achieving homogeneity 10^4 to 10^5 times better than our current experimental efforts.

Third, and most important for force-detected NMR, exposing the sample to rf pulses drives the inversion of magnetization that resonantly excites the detection apparatus, and allows coherent control over the sample's spin Hamiltonian. The Rabi frequency characterizes the strength of these pulses, and it must be comparable to or greater than the inhomogeneous linewidth of the sample in order to invert a substantial fraction of the sample magnetization. When the field inhomogeneity substantially exceeds the Rabi frequency at a given rf power, only the "sensitive slice" of spins in the sample inverted during the pulse contributes to the force signal, thus substantially reducing the signal-to-noise ratio [14]. The paramount advantage of BOOMERANG lies in providing field homogeneity sufficient for coherent spin manipulations and inversions of the *entire* sample magnetization. This allows optimal application of the full scope of modern time-domain NMR spectroscopy and imaging pulse sequences.

1.2.D Encoding Time-Domain NMR into Mechanical Oscillations

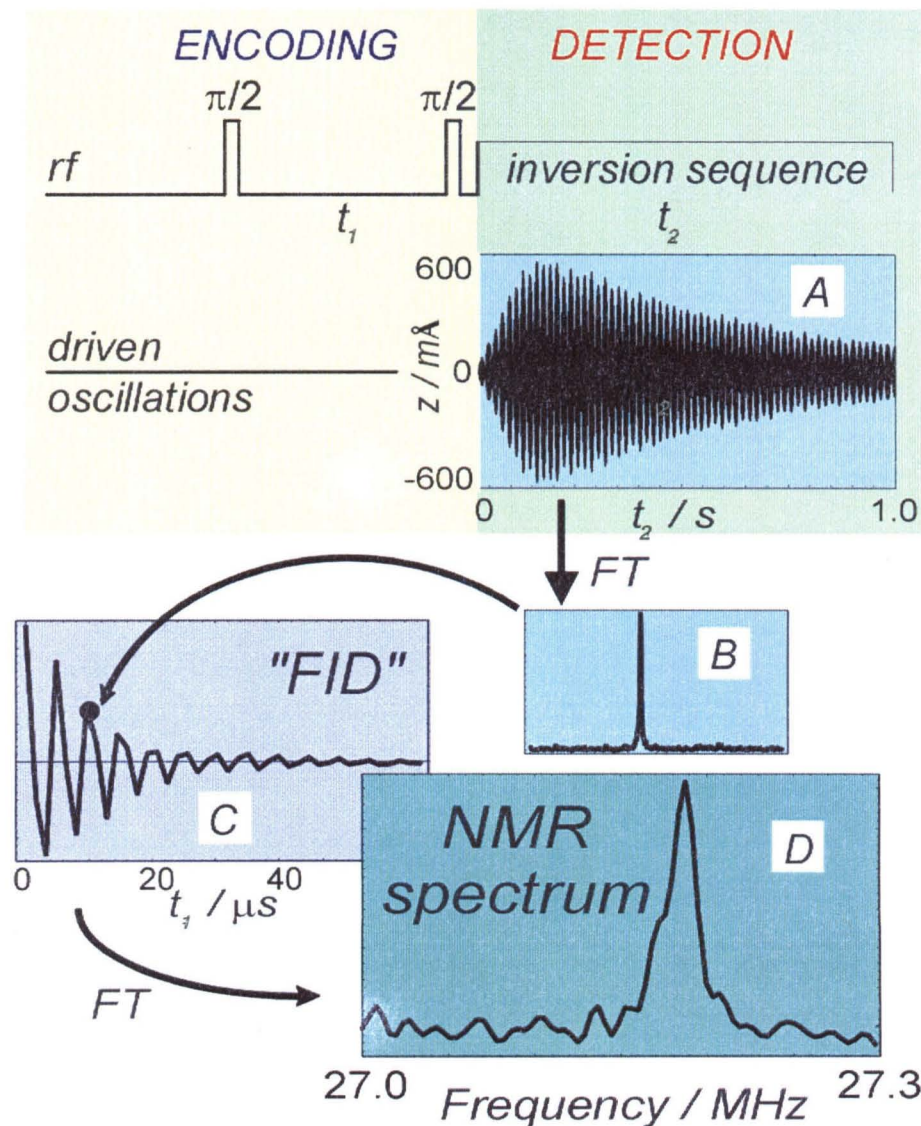
Since prototypical BOOMERANG experiments detect longitudinal magnetization and cannot observe Larmor precession directly, we must make simple modifications to time-domain NMR pulse sequences developed for traditional transverse detection. Our version of time-domain FTNMR is analogous to pulsed spin-lock detection with inductive coils [23, 24], and shares many attributes, such as quadrature-detection encoding schemes, with conventional two-dimensional NMR experiments [25].

The BOOMERANG oscillator is driven with an amplitude and sign (phase) proportional to the sample's longitudinal magnetization M_z present at the start of the cyclic inversion period. To measure an NMR spectrum, this detection period is preceded by a period of spin evolution, which is altered on successive repetitions of the experiment. The parameters of this evolution encoding period and the parameters in the desired spin Hamiltonian to be measured determine the amplitude of the mechanical signal for that repetition.

Figure 1.2.5 depicts the measurement of a time-domain Fourier-transform NMR spectrum using BOOMERANG. During t_1 , transverse magnetization created by the first pulse evolves under the total spin Hamiltonian, which includes both the interaction of a given spin with the static field and any spin-spin interactions. This transverse magnetization, at any given time after the first pulse, is the same as would be observed as a free induction decay (FID) in inductive NMR. After the time t_1 , the second $\pi/2$ pulse converts one component of the transverse magnetization (*e.g.*, M_x or M_y) to longitudinal magnetization M_z , which is measured in the detection period by cyclic inversion. This measured amplitude and sign becomes one point in the "pointwise FID," which results from repeating the pulse sequence for many values of t_1 on successive repetitions of the experiment. This pointwise FID is Fourier transformed to yield the NMR spectrum. All transients shown in figure 1.2.5 were acquired with the prototype on protons in a 2.6 mm sphere of water at 27.2 MHz.

Any modern NMR pulse sequence can be adapted to longitudinal detection with BOOMERANG by simply inserting the desired pulse sequence into the evolution period of this pointwise acquisition protocol. This includes the body of pulse sequences used in

Figure 1.2.5: Encoding NMR into Mechanical Oscillations. The oscillator is driven by cyclic inversion of the sample's nuclear spin magnetization and a mechanical displacement signal A is recorded during the “detection” period t_2 for a given t_1 value. The Fourier transform of A yields a spectrum B with a peak at the mechanical driving frequency. The area of this peak is proportional to the M_z present at the start of the detection period. Weighting of the spectrum B gives a single point in the “FID” C. The NMR pulse sequence in the “encoding” period is used to modulate M_z as a function of t_1 to build up the FID point-by-point. The FT of the encoded FID signal vs. t_1 gives the 1D FT-NMR spectrum D. All data shown were collected on a 2.6 mm sphere of water using our prototype BOOMERANG spectrometer.



modern imaging experiments, such as Fourier zeugmatography and back-projection reconstruction, in which gradient pulses are introduced in the encoding periods with

suitable coils or with controlled displacements of the detector or other magnets. Sensitivity as well as spatial or frequency resolution may be separately optimized, vastly improving throughput and information content relative to MRFM methods [14]. The use of homogeneous fields to acquire signal from the whole sample during imaging detection periods, which was pioneered by Mansfield [26] and Lauterbur [27], was naturally selected in the 1970's as the most sensitive and efficient imaging method over the sensitive-volume method of Damadian [28].

In our experiments, the magnetization is inverted twice per oscillator period using a novel phase-cycled, tangent-frequency-modulated adiabatic rapid passage (ARP) scheme. Using tangent ARP at twice the oscillator resonance frequency, along with sweeping the same direction in frequency (*e.g.*, low to high) on each inversion, reduces spurious driving of the oscillator that is observed when the frequency modulation is simply sinusoidal or otherwise continuous through the NMR line. Sections 3.2.D – 3.2.J below describe the details of these novel spin inversion and NMR spectroscopy experiments.

1.2.E Sensitivity and Scaling: BOOMERANG and Inductive NMR

We may calculate the signal force on an arbitrary detector magnet by substituting $\mu_d = M_d dV_d$ into equation 1.2.1A, where dV_d is the differential volume element of the detector magnet and M_d its magnetization, and integrating over the detector magnet volume. The integration over the sample volume is implicit in that we assume a uniformly z-polarized spherical sample so that the field due to the sample is equivalent to that of a point dipole at its center. For a uniformly magnetized sample and detector magnet, the resulting RMS signal force is [3]

$$F_z = \frac{\kappa_F \mu_0 V_s M_s M_d}{\sqrt{2} R_{max}}, \quad 1.2.3$$

where R_{max} is the distance from the center of the sample to the surface of the detector magnet, and κ_F is a dimensionless factor dependent on the specific geometry of the detector magnet and is found through the volume integration. M_s and V_s are the sample magnetization and volume, respectively, and μ_0 is the vacuum susceptibility. For the geometry of our optimized BOOMERANG detector magnet, $\kappa_F = 0.0723$ [3, 17].

The main source of noise in FDMR experiments is the thermal, or Brownian, motion of the oscillator. The thermal-noise-force spectral density is given by

$$F_n(\omega_h) = \sqrt{8k_B T m / \tau_F} = \sqrt{4k_B T m \omega_h / Q_h}, \quad 1.2.4$$

which is the standard expression for a harmonic oscillator at temperature T with quality factor Q_h , mass m , resonance frequency ω_h , and ringdown time $\tau_h = 2Q_h/\omega_h$ [14, 29], and where k_B is Boltzmann's constant. The steady-state, RMS displacement due to a force at the resonance frequency ω_h is

$$Z = \frac{F(\omega_h)Q_h}{m\omega_h^2} = \frac{F(\omega_h)Q_h}{k}. \quad 1.2.5$$

where the force can be either the signal (eq. 1.2.3) or the noise (eq. 1.2.4). Here, k is the oscillator's harmonic spring constant. For high- Q_h oscillators, this response to both signal force and noise force is sharply peaked at the resonance frequency. The enhancement of the response proportional to Q_h is key to the fact that the thermal motion noise is the dominant noise contribution.

We obtain the RMS signal-to-noise ratio (SNR) for BOOMERANG FDNMR by dividing eq. 1.2.3 by eq. 1.2.4 to give

$$SNR_{BOOM} = \frac{\kappa_F \mu_0 V_s M_s M_d / R_{max}}{\sqrt{16k_B T m \Delta v / \tau_h}}, \quad 1.2.6$$

where Δv is the bandwidth of the measurement. This detection bandwidth is set by the rate of decay of the cyclically inverted longitudinal magnetization. The length-scale parameter R_{max} and the scale-independent factor κ_F summarize the geometry. The dipole moment of the sample ($V_s M_s$), the magnetization of the oscillator M_d , the mass m of the oscillator, and the ringdown time τ_h complete the determination of SNR_{BOOM} . Note that the Q_h and ω_h *per se* of an oscillator do not enter by themselves into the sensitivity, but only the ringdown time τ_h .

For inductive detection, the SNR is given by the comparable expression

$$SNR_I = \frac{\kappa_F \mu_0 V_s M_s \omega_{0f} / R_{coil}}{\sqrt{8k_B T R \Delta v}}, \quad 1.2.7$$

where R_{coil} is the closest distance from the coil conductor to the sample center, R is the resistance of the particular detection coil and accompanying circuit, ω_{0f} is the Larmor

frequency, and κ_i is a dimensionless constant dependent on the coil geometry [3]. This expression comes from taking the EMF signal induced in the inductive coil due to the sample magnetization, and dividing by the Johnson noise in the tuned LCR circuit, which is the dominant noise in the inductive-detection experiment [3, 30].

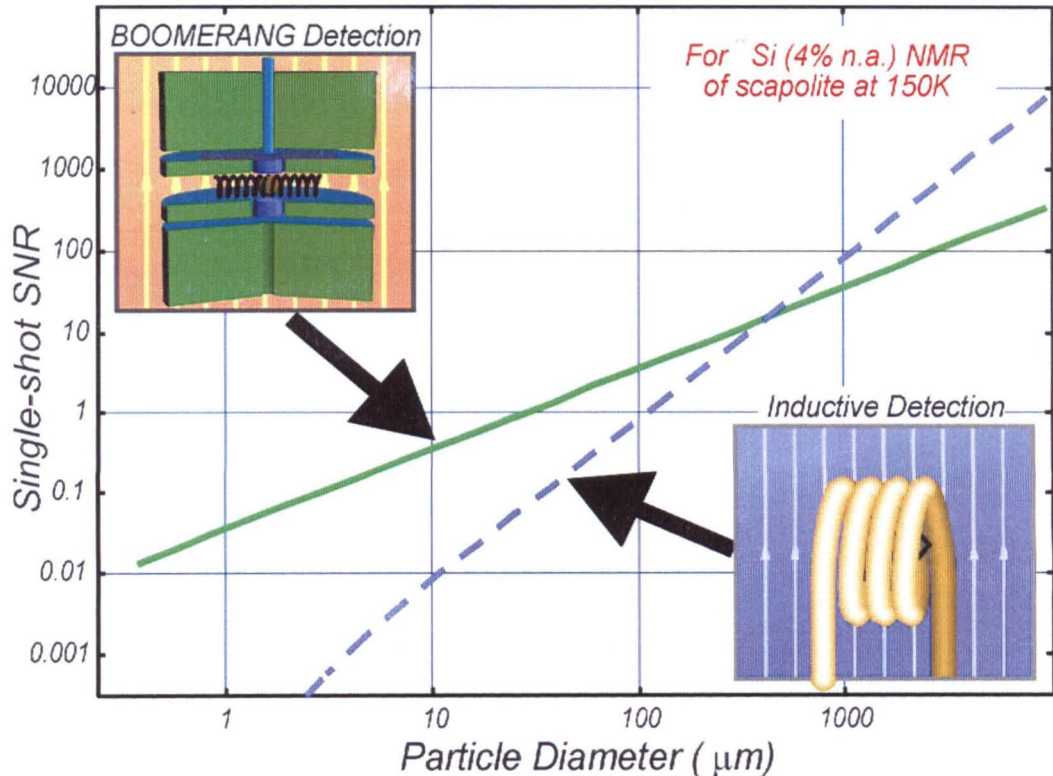
Using the results of this sensitivity analysis, we may compare the scaling properties of BOOMERANG force-detected NMR to inductively detected NMR. Assuming for BOOMERANG detection that the ringdown time τ_h is scale invariant, *i.e.*, that we may scale the ω_h and Q_h of the oscillator together, SNR_{BOOM} scales as $r^{1/2}$. Alternatively, if ω_h scales as $1/r$ while Q_h remains fixed, or τ_h scales as r , then SNR_{BOOM} scales as r . While neither of these assumptions rigorously holds for mechanical oscillators, recent experiments [31-33] suggests that the latter assumption holds, at least for oscillators without provisions for softening their modes as I describe in sections 2.1.D and 2.2.C. While comprehensive theories of dissipation do not exist for mechanical oscillators, inductive coil dissipation is quite well understood. For inductive detection, SNR_I scales as r^2 for coil conductors above the rf skin depth, where the coil resistance R is scale invariant, and as $r^{5/2}$ below the skin depth limit, where R scales as $1/r$. In any case, SNR_{BOOM} scales much more slowly with size than SNR_I so that below a certain size scale, BOOMERANG has better sensitivity than inductive NMR.

If we now fix length scale and compare Larmor frequency dependence, force detection scales more favorably for lower magnetic fields and for nuclei of lower gyromagnetic ratio, thus easing the requirement of high magnetic fields when designing high sensitivity BOOMERANG spectrometers. SNR_I scales as ω_0^{-2} for coils whose diameter is smaller than the rf skin depth, where R is frequency-independent, and as

$\omega_0^{7/4}$ for coil diameters greater than the skin depth, where R is proportional to $\omega_0^{1/2}$. In BOOMERANG, SNR_{BOOM} scales only with the frequency dependence of the equilibrium nuclear magnetization, which is common to the two methods. With the assumption of Curie-law magnetization implicit in the discussion of inductive detection [2], this is a linear dependence on ω_0 . Similar comparisons for the nuclear gyromagnetic ratio γ show that SNR_I scales as γ^3 for coils below the skin-depth limit, and that SNR_{BOOM} scales as γ^2 (only Curie-law dependence).

Presently, NMR is done primarily on millimeter-sized samples with 10^{16} or more target spins. The lower limit on the number of spins of $\sim 10^{12}$ protons in inductive

Figure 1.2.6: SNR Scaling Comparison. Using a situation of probable importance to *in-situ* planetary exploration, we compare the sensitivity of BOOMERANG to inductive detection on ^{29}Si at natural-abundance in a scapolite mineral sample at 2T field strength and $T = 150\text{ K}$ (Mars average temp).



detection with coils of $\sim 40 \mu\text{m}$ diameter come from experiments in the Webb [34] and Pennington [35] groups. Thus, high-resolution NMR has been limited to samples that are large relative to those accessible with other analytical methods having higher sensitivity, but lower information content. Figure 1.2.6 shows predicted sensitivity curves for natural abundance ^{29}Si NMR in a scapolite mineral sample using either BOOMERANG or inductive detection. Below $\sim 0.5 \text{ mm}$ sample diameter, BOOMERANG is predicted to have higher sensitivity than magnetic induction, and at the $60 \mu\text{m}$ scale the SNR advantage is greater than a factor of ten.

1.2.F Mechanical Dissipation

Damping in mechanical oscillators remains an open and incomplete field of study. Here I summarize various sources of dissipation and our current understanding of their importance. In general, damping in a mechanical oscillator occurs from: 1) thermal transport and relaxation processes, 2) sound (phonon) radiation through oscillator supports, 3) interaction with a viscous ambient, 4) surface transport or dislocations, 5) or interaction with damped electric or magnetic fields.

Viscous damping, *e.g.*, from ambient atmosphere or other fluid, presents an often-dominant damping source, but only when the oscillator is used outside a vacuum environment. For micron-scale oscillators, the pressure of air must be below $\sim 1 \text{ mTorr}$ to negate this viscous damping [32]. We design our experiments for vacuum operation, so we may neglect this term. Phonon radiation through the oscillator supports, or “anchors,” poses another significant damping source with some descriptive theory, although possibly not complete [32]. Finite-element method (FEM) engineering

packages [36, 37] may also provide methods for computing dissipation through supports. I briefly discuss possible remedies for anchor losses in section 2.2.F.

Damping due to magnetic properties of the detector oscillator may manifest itself in two forms, hysteresis loss and eddy-current damping. These phenomena are analogous to the losses in electrical ac transformers, which incorporate oscillating currents through solenoids and thus produce oscillating magnetic fields that permeate ferromagnetic cores and other nearby conducting materials [38]. In the case of BOOMERANG, the magnetic field oscillates as the detector magnet moves relative to the rest of the magnet assembly, which also has ferromagnetic elements that electrically conduct. Local changes in orientation or magnitude of the magnetization in the detector and surrounding magnets may cause hysteresis damping. We may ignore this effect under the assumption that when the magnet assembly is saturated, the area inside the hysteresis curve is zero and no damping occurs. Intuitively, we can see that when saturation is reached, all magnetic dipoles in the assembly are perfectly aligned and none will rotate or shrink unless the local magnetic field drops below the saturation level.

This oscillating magnetic field also induces eddy currents in the detector and ring magnets due to the Lorentz force on the electrons in these conducting magnets, and these currents dissipate resistively to heat the magnets and damp the oscillator motion [17, 18, 39]. The EMF for these currents is proportional to the gradient with respect to the (changing) oscillator coordinate of a ferromagnetic element at the position of a conductive element. These gradients are not zero by design. Thus, the most likely scheme for eliminating eddy current damping is to increase the effective electrical resistance of the magnets, either by sectioning the magnets into electrically isolated

pieces, or using an entirely new (and currently unknown) magnetic material with high magnetic saturation and low electrical conductivity. For a quantitative assessment of eddy current damping in BOOMERANG, I refer the reader to the Ph.D. thesis of Garrett M. Leskowitz [17]. An important conclusion is that this mechanism yields a scale-invariant contribution to τ_h , and thus does not pose a barrier to reducing the length scale of BOOMERANG designs. However, using high-effective-resistivity ferromagnets will be important to achieving $\tau_h \sim 1$ sec.

In beam-like oscillator suspensions, thermal relaxation damping, termed *thermoelastic* damping, has a well-developed and experimentally verified theory originated by Zener [40], and recently supplemented by Lifshitz and Roukes [41]. In thermoelastic damping, heat flows in the beam parallel to the direction of beam motion due to the expansion on one side of the beam and compression on the other side, that is, along the thickness dimension of the beam. If local thermal relaxation occurs quickly enough relative to an oscillation cycle, then heat is dissipated in the beam. However, if the relaxation rate is much faster than the mechanical oscillation frequency, then the temperature remains more nearly uniform and less thermal energy dissipates. Thus a thermal relaxation peak occurs in the dependence of Q_h as a function of frequency. Here I review Zener's theory since for our purposes it is simpler to use for analysis and provides accuracy to within 2% of the Lifshitz and Roukes theory.

For the fundamental mode of a rectangular beam, thermal diffusion occurs with a characteristic relaxation time

$$\tau_z = \frac{h^2}{\pi^2 \chi}, \quad 1.2.8$$

where h is the thickness of the beam along the oscillation axis and χ is the thermal diffusivity of the beam material. Zener's simple Lorentzian thermal dissipation is then given by [40]

$$\frac{1}{Q_{hZ}} = \frac{E\alpha^2 T}{C_p} \frac{\omega_h \tau_Z}{1 + (\omega_h \tau_Z)^2}, \quad 1.2.9$$

where Q_{hZ} is the mechanical quality factor due to thermoelastic damping, E is the Young's modulus, T is temperature, C_p is the heat capacity at constant pressure, and α is the linear thermal expansion coefficient. I give these thermal properties for several materials in table 2.2.1 in section 2.2.B.

We may use this result to calculate the curve for the ringdown time τ_h for

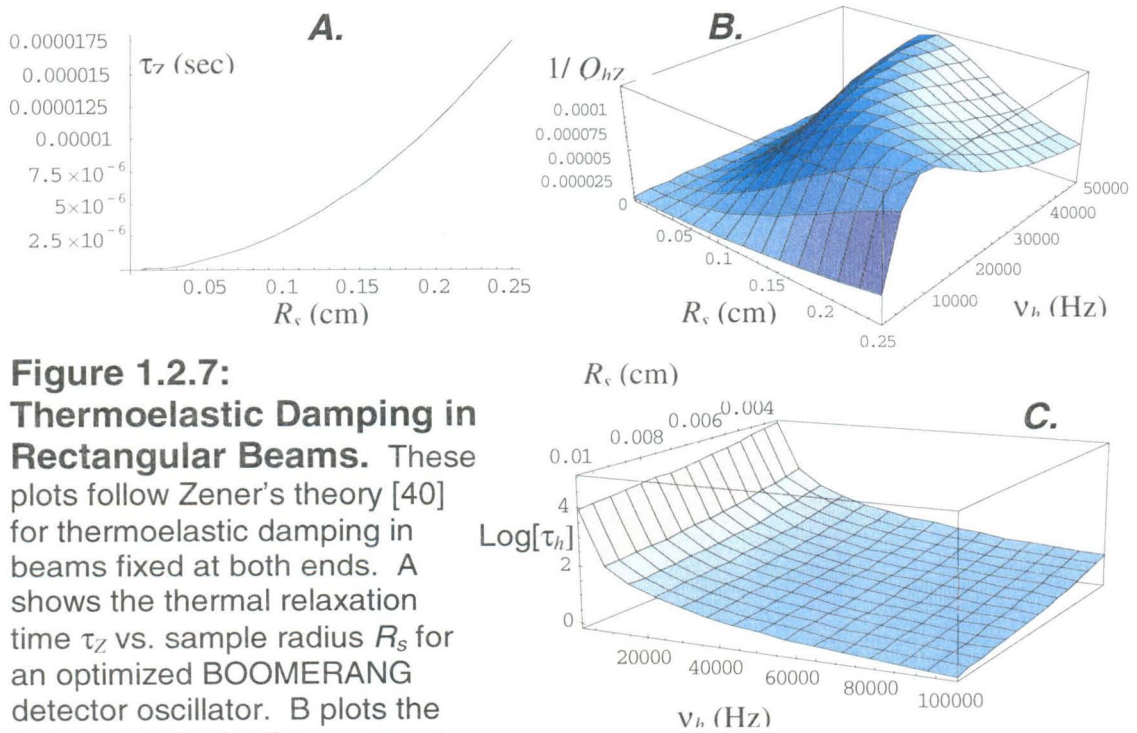


Figure 1.2.7:
Thermoelastic Damping in Rectangular Beams. These plots follow Zener's theory [40] for thermoelastic damping in beams fixed at both ends. A shows the thermal relaxation time τ_Z vs. sample radius R_s for an optimized BOOMERANG detector oscillator. B plots the calculated dissipation constant

maintaining a low resonance frequency for a given size scale in avoiding this damping mechanism. Plot C shows the log of the mechanical ringdown time τ_h due to thermoelastic damping vs. R_s and v_h .

oscillators due to thermoelastic damping. Assuming we can soften the oscillator resonance using the BOOMERANG magnet array and capacitive feedback transducer described in sections 2.1.D and 2.2.C, we expect to achieve approximately linear scaling of h along with the other beam dimensions. Figure 1.2.7 shows plots of τ_Z , $1/Q_{hZ}$, and $\text{Log}[\tau_h]$ vs. sample radius and vs. the resonance frequency v_h in Hz for optimized BOOMERANG detectors with silicon beams, where we assume the beam thicknesses as 0.05 times the sample radius. An important conclusion is that the negative magnetic and/or capacitive force constant contributions to the BOOMERANG designs of Chapter 2 have the advantage of minimizing this loss mechanism. In the case of our micron-scale designs optimized for 60 μm -diameter samples and $\tau_h = 1 \text{ kHz}$, the thermal relaxation time $\tau_Z = 3 \times 10^{-10} \text{ sec}$, and the corresponding mechanical oscillator ringdown time $\tau_h = 9 \times 10^4 \text{ sec}$. If instead the resonance frequency of our oscillator were not softened by design, and had $v_h = 6 \times 10^4 \text{ Hz}$, then τ_h would be limited to 0.6 sec by thermoelastic damping.

Yasumura et al. have asserted that surface-related damping in cantilevers is proportional to the thickness, and researchers in Kenny's and Rugar's group [31, 32, 42] have applied surface-passivation techniques, *e.g.*, terminating silicon surfaces with hydride and *in-situ* heat treatment to drive off impurities, to realize gains of factors of 2 – 6 in Q_h for a given cantilever. This group has also found reductions in damping between room temperature operation and $T = 4 \text{ K}$ or below to be approximately a factor of 5 [31, 32].

1.2.G BOOMERANG for Microscale and Nanoscale NMR

The scaling relations presented above, that the signal to noise ratios for induction and force detection differ, suggest different strategies for enhancing sensitivity in microscopic BOOMERANG *vs.* inductive detection with microcoils. In BOOMERANG, the sensitivity scaling suggests that samples be broken up and distributed among many spectrometers for optimal sensitivity. BOOMERANG thus exhibits the capability to signal average not only in *time*, as in traditional spectroscopy, but also in *space*. While breaking up the sample for distribution among millions of spectrometers may be impractical, the lesson of breaking up the sample may be very practical, particularly with liquid or surface-bound samples. For instance, suppose that a given sample volume is divided to be analyzed by an array of 10^4 detectors, each with length scale smaller by $10^{4/3}$ than a single device needed to measure the whole sample in one detector. If the SNR for each detector scales as r^1 , then the sensitivity with the array is better by $((10^4)^{1/2})/10^{4/3} = 10^{2/3} = 4.6$. If instead we assume that τ_h is scale invariant, or $\text{SNR} \propto r^{1/2}$, then the array has a sensitivity advantage of $((10^4)^{1/2})/((10^{4/3})^{1/2}) = 10^{4/3} = 21.5$ over a single-detector measuring the whole sample.

A further synergy exists in the use of fluctuations in magnetization to enhance the sensitivity of NMR with very small samples, particularly those for which the inverse of the fractional polarization exceeds the square root of the number of molecules. In this case, the fluctuations in magnetization are larger than the mean polarization magnetization upon which the ordinary NMR signal depends. The CONQUEST [43] (see section 1.3.B) measurement paradigm encodes coherent spectroscopy into these fluctuations to conduct spectroscopy with greater sensitivity.

With the construction of BOOMERANG detectors using microfabrication techniques, as described in Chapter 4, parallel fabrication of tiny NMR spectrometers useful at fields accessible by permanent magnets may usher in a new era in low-cost NMR analysis in laboratories, commercial settings, or remote locations. In Chapter 4, I detail our efforts, in conjunction with the Microdevices Laboratory at NASA-JPL, to build a micron-scale *in-situ* spectrometer for extra-terrestrial exploration [39]. This frugality in manufacture will also allow for massively parallel analysis of sample libraries, such as microarrays generated combinatorially in drug discovery efforts. Figure 1.2.8 depicts a representative implementation of an array of parallel BOOMERANG detectors.

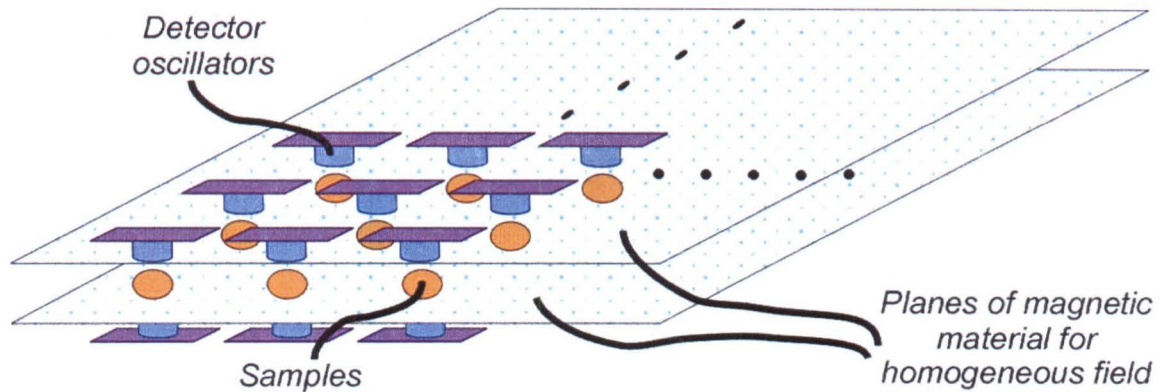


Figure 1.2.8: Parallel Analysis with BOOMERANG. A large array of samples lies between two planes of magnetic material, into which the BOOMERANG detector oscillators are integrated. Rf excitation may be provided simply by a single macroscopic circuit, or by individual microcoils. Multiplexed optical displacement sensing will allow massively parallel signal detection in which many optical signals may impinge upon one photodetector and digitizer, and might be separated in the mechanical frequency domain. Dividing an arbitrary sample gives a sensitivity *gain*, in contrast to inductive detection. The SNR scaling for the array is better than for the single detector by the square root of the number of detectors.

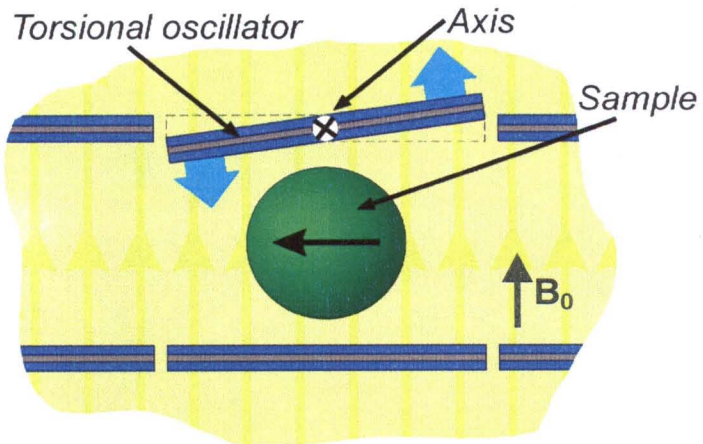
In the quest to best utilize BOOMERANG's strengths, we have contemplated designs for nanoscale mechanical oscillators and magnet assemblies. As described in section 2.1.D below, if we scale all mechanical oscillator dimensions together and the

elastic modulus of the suspension is scale invariant, the resonance frequency v_h scales as $1/r$. While we may endeavor to soften mechanical modes using magneto- and electrostatic forces, at some size scale, v_h may become unacceptably high for longitudinal detection (efficient cyclic inversion) of magnetic resonance. This will necessitate use of direct transverse detection, where the precessing sample magnetization couples to a mechanical oscillator resonant at or near the Larmor frequency. The most sensitive detection method will involve spin-lock detection, where the spin magnetization is prolonged along a certain axis in the rotating frame. As with ARP, the energy supplied to the detector can then exceed that stored in the spin system, in contrast to the case of free precession of the spins.

While nanoscale linear BOOMERANG oscillators present possible candidates for Larmor-frequency detection, we have originated torsional oscillator designs that achieve better coupling to the sample spins and may provide lower dissipation resonances for higher sensitivity detection. Figure 1.2.9 depicts the basic form of this scheme for

Figure 1.2.9:
Transverse Detection
using Torsional Nano-

Oscillators. This cross-sectional view shows a sample's spin magnetization precessing at the Larmor frequency coupling directly via a dipole-dipole torque to a cylindrical detector magnet suspended about a torsion axis. Optimized geometrical factors compare favorably to those of longitudinal-detection case, allowing BOOMERANG SNR scaling down to nanometers.



transverse detection. Garrett M. Leskowitz presents detailed designs for torsional-resonator detectors in his thesis [17].

Another possible method of non-equilibrium sensitivity enhancement at the nanoscale lies in the “freeze-ray” technique proposed by Weitekamp [44], in which both energy and entropy are transferred radiatively from a spin system to a damped mechanical “cavity,” *i.e.*, a damped nanomechanical oscillator (characterized by a low temperature), to order the spins via incoherent spontaneous emission.

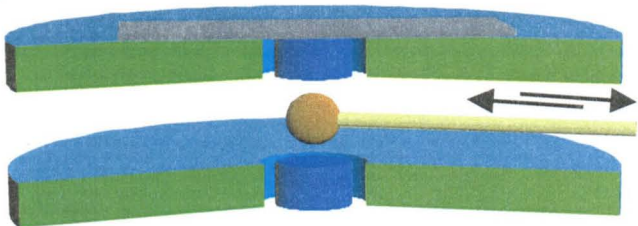
1.3 BOOMERANG-Related Concepts and Instrumentation

1.3.A BOOMERANG Magnetometry

Since BOOMERANG is in essence a sensitive magnetic moment detector, we have investigated its use in observing bulk magnetism and magnetic imaging of arbitrary diamagnetic, paramagnetic, and ferromagnetic samples [45]. Outside the realm of magnetic resonance, magnetic properties are usually measured using Faraday-law inductive coils [46], superconducting quantum interference devices (SQUIDs) [21, 47], and more recently, cantilever-based force detectors [48, 49]. BOOMERANG presents a flexible, relatively low-cost, and high-sensitivity competitor to these other methods. It

Figure 1.3.1: BOOMERANG

Magnetometer. By sweeping the sample past the detector magnet at $v_h/2$, we may drive the oscillator resonance due to the change in coupling force. The sample position might be driven using a rotor, pneumatics, MEMS actuator, etc.



supplies a homogeneous (or even zero) field across the sample, allows excellent spatial resolution, and requires no cryogenic apparatus. While our macro-scale prototype BOOMERANG device has excellent magnetic moment sensitivity (1×10^{-11} emu/rt Hz) at $B_0 = 0.7$ T, as mentioned in section 1.2.C, the predicted sensitivity of the micron-scale BOOMERANG device at $B_0 = 2$ T is far better - 2.3×10^{-16} emu/rt Hz, assuming a τ_h of 1 s. Figure 1.3.1 shows the BOOMERANG magnet assembly with a sample on an actuator arm.

In magnetometry, cyclically shifting the position of the sample relative to the detector magnet produces the force modulation needed to drive the resonant mode of the BOOMERANG detector. The simplest scheme would be to sweep the sample past the detector magnet at $v_h/2$ with an oscillation amplitude of approximately five sample diameters. This modulates the force between the sample and detector magnetic moments at v_h , where the force amplitude oscillates between nearly zero, and the maximum proportional to $\mu_s * \mu_d$. This modulation might be accomplished by mounting a sample, or group of samples onto a rotor, or using a reciprocating sample-position modulator such as a cam/follower or a crank/piston arrangement.

Using hard ferromagnets for the detector and ring magnets, we may also design BOOMERANG magnetometers for magnetically fragile samples that require small or zero field. This prevents remagnetization or saturation of samples with low-coercivity magnetic elements, such as those found in many geological samples [50]. In this scheme, both pairs of detector and ring magnets would be polarized in one direction, and an equal and opposite external field would yield a net zero field across the sample. This has no

effect on the sensitivity of the BOOMERANG detector, except that hard ferromagnets are currently limited to $M_s < 1.4 \text{ T}/\mu_0$.

1.3.B Spin Noise and the CONQUEST Measurement Paradigm

Through nearly the entire history of NMR, noise in the detector has dominated the sensitivity of NMR experiments. As we scale detector size down, and the number of spins in a given sample decreases, we are confronted with the problem of quantum-statistical sample noise, or “spin noise,” becoming the dominant noise source in time-domain NMR experiments [43, 51]. This phenomenon parallels the noise due to counting statistics in a measurement of a quantized sample, *e.g.*, photon shot noise, which is proportional to the square-root of the number of photons impinging on a detector [52]. When observing spins using pointwise time-domain NMR, we may express the SNR due to spin noise in the absence of detector noise as

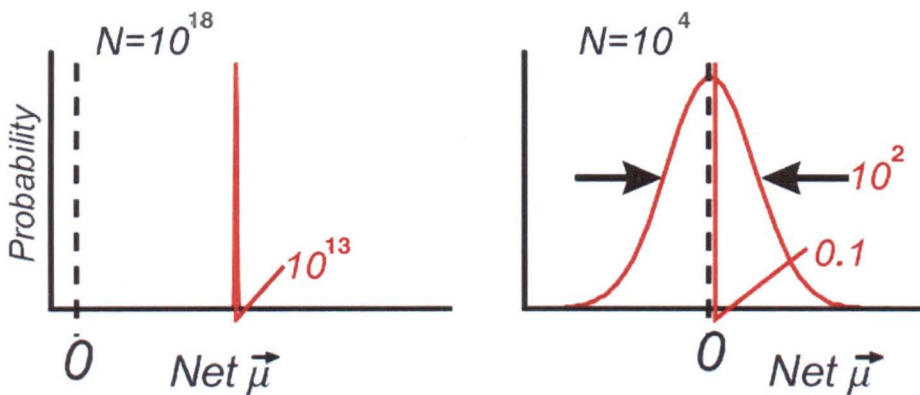
$$SNR_{tg} = \frac{Signal}{Noise} = \frac{PN}{\sqrt{N}} = P\sqrt{N}, \quad 1.3.1$$

where P is the mean polarization of the sample, and N is the number of spins in the sample.

This noise becomes important when $P\sqrt{N} < 1$, which we term the “spin-noise limit.” For proton NMR at typical polarizations of $P \sim 10^{-5}$, this becomes important when the sample contains less than 10^{10} spins. Figure 1.3.2 depicts the spin-noise

Figure 1.3.2: Spin Noise Dominates NMR Signals at Low N .

The graph on the left shows the case of NMR spectroscopy at the macro scale. The graph on the right, at low N , illustrates that the traditional single-quantum time-domain measurement paradigm fails since the mean magnetization is much smaller than the variance in the magnetization.



phenomenon graphically. Several research groups have observed transverse-plane spin noise using concentrated samples and relatively strong coupling between sample and detector [53-55], but to date, spin noise has not been the dominant noise source in any experiment.

This noise may be viewed as initial condition noise occurring for each repetition of a multiple-repetition experiment. The instantaneous spin polarization fluctuates on the timescale of the spin-lattice relaxation time T_1 , and the fluctuations can influence or dominate the initial polarization at the start of each repetition, causing a decrease in SNR in the time-domain signal. When conducting our simple pointwise first-order FTNMR experiment shown in section 1.2.D, the SNR_{1q} due to spin noise, for an isochronous

(chemically equivalent) group of spins and in the limit of small polarization ($P^2 \ll 1$), is given by

$$SNR_{1q}(t_1) \equiv P\sqrt{N} \cos \omega_0 t_1, \quad 1.3.2$$

where ω_0 is the Larmor frequency of the spins, and t_1 is the evolution time in the time-domain experiment [43].

To circumvent this unfavorable SNR scaling, we have developed a new method of pointwise NMR acquisition involving combinations of successive measurements on the spin system. The simplest of these is to measure the spin magnetization prior to each repetition of a pointwise experiment, which we call $I_z(0)$, and multiply it with the usual measurement made after the spin evolution of interest, $I_z(t_1)$. These measurements must take place in a time comparable to or less than T_1 , such that the spin noise is correlated between the two measurements. We combine these measurements to yield a second-order correlation function $S_2(t_1)$, which has analogs in optical intensity interferometry [52], and yields better SNR than first-order measurement schemes. In the Heisenberg representation, we represent the expectation value of this product of first and second measurements as

$$\langle S_2(t_1) \rangle = \text{Tr}\{\rho(0)I_z(0)I_z(t_1)\} = \langle I_z(0)I_z(t_1) \rangle, \quad 1.3.3$$

where $\rho(0)$ is the nuclear-spin density operator at time zero. Indeed, we utilize the fluctuating spin magnetization *as a source of signal*, since in the spin-noise limit the fluctuating magnetization is larger than the mean (Boltzmann) magnetization. The sensitivity SNR_{2q} due to spin noise for this two-quantum measurement, in the limit of $P\sqrt{N} \ll 1$, is given by [43, 56]

$$SNR_{2q} \equiv \frac{\sqrt{N} \cos \omega_0 t_1}{\sqrt{N + (N-2) \cos^2 \omega_0 t_1}}, \quad 1.3.4$$

which has the surprising feature that SNR is approximately unity, and is essentially scale invariant below the spin noise limit. Thus, the potential improvement in SNR by using these second-order correlated measurements is on the order of $(P\sqrt{N})^{-1} \gg 1$. In this way, correlated *observations narrow quantum uncertainty, enhancing spectroscopic transients* (CONQUEST).

Although multiplying the “before” and “after” measurements forms the simplest second-order correlation function, other combinations of the two measurements, such as division or linear combinations of multiplication and division, give useful correlation functions. We have formulated a “dispersive operator” from a combination of multiplication and division by the “before” measurement, which yields better SNR than either multiplication or division over the entire range of N . This operator f_b takes the form [43, 56]

$$f_b(I_z) = \frac{1}{\zeta + \frac{I_z}{\zeta}} = \frac{\zeta I_z}{\zeta^2 + I_z^2}, \quad 1.3.5$$

where ζ is an optimization scaling parameter, which is adjusted to optimize the SNR of the correlation function. In the regime where spin noise dominates, the optimum choice for ζ is roughly equal to the quantum uncertainty in I_z [43]:

$$\Delta I_z = \frac{1}{2} \sqrt{N(1 - P^2)}. \quad 1.3.6$$

Figure 1.3.3 depicts the CONQUEST two-point measurement experiment timeline (1.3.3.A), and the sensitivity curves for single-point and two-point measurements using

the dispersive operator, both in the absence of detector noise (1.3.3.B), and in the presence of detector noise (1.3.3.C). We have confirmed these SNR curves through separate calculations involving Monte Carlo simulations using discrete spin statistics [43, 57], and analytic methods involving powers of the partition function [3].

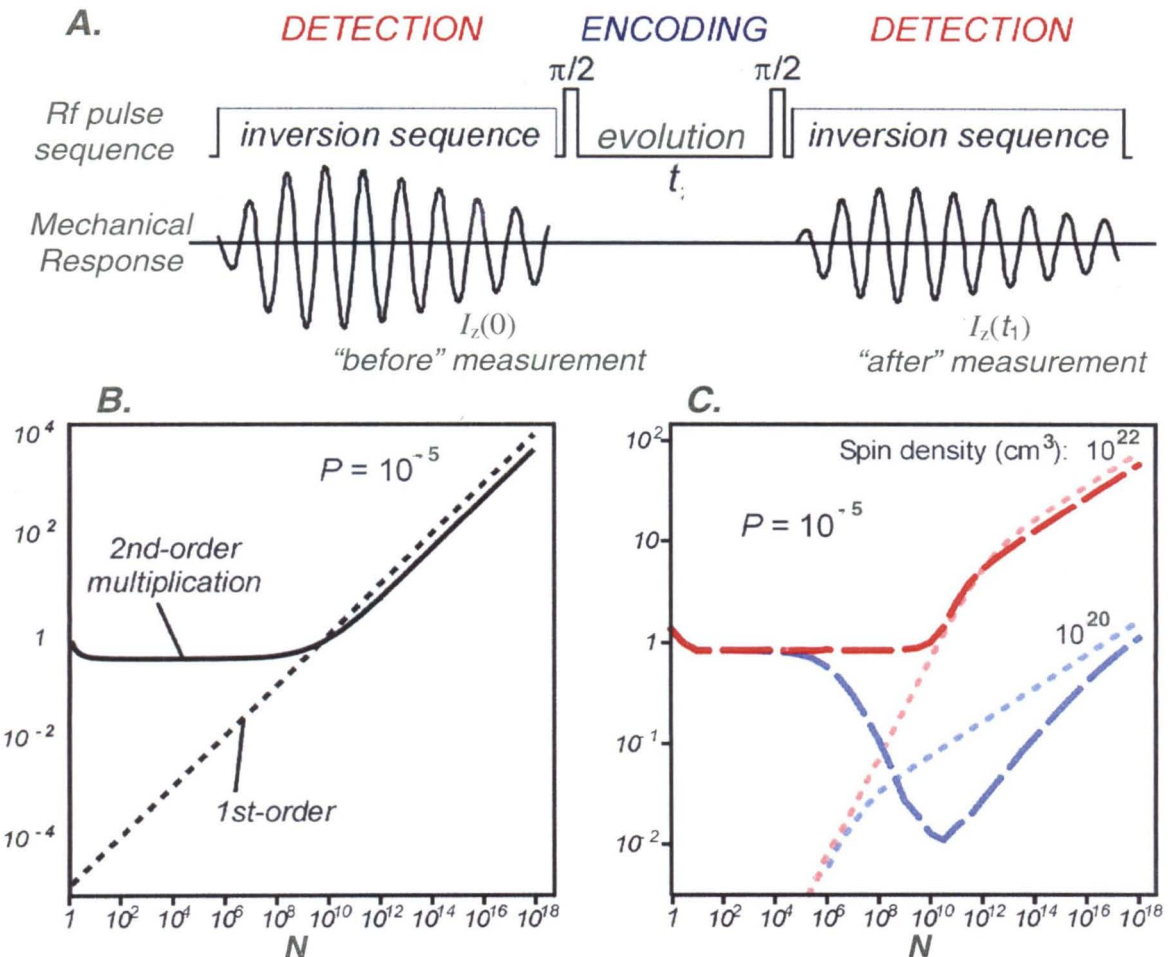


Figure 1.3.3: CONQUEST Measurement Scheme and Sensitivity

Predictions. A shows the timeline for making a 2nd-order CONQUEST measurement using BOOMERANG. B shows the predicted SNR for 1st-order and 2nd-order measurements in the absence of detector noise, while C plots predicted SNR with the addition of BOOMERANG detector noise for oscillators optimized for spherical samples with $10^{22}/\text{cm}^3$ spin density, and with $\tau_h = 100$ ms. In both cases, CONQUEST measurements allow practical NMR on small samples. Dotted lines represent predicted 1st-order experiments, while the solid or dashed lines represent 2nd-order experiments.

CONQUEST applies generally to any method of measuring spin magnetization and possibly other internal properties of molecules or other systems. It becomes important whenever the fluctuations in the observable of interest are comparable to or larger than its expectation value, so pointwise first-order correlation function measurements would suffer from poor reproducibility due to the uncertainty of the initial condition. Finally, since we use this non-equilibrium, fluctuating spin magnetization as our signal, we expect not to require a relaxation delay after measurements to refresh polarization, thus vastly increasing throughput.

References

1. Slichter, C.P., *Principles of Magnetic Resonance*. 3rd Enlarged and Updated ed. Springer Series in Solid-State Sciences 1. 1990, New York: Springer-Verlag.
2. Abragam, A., *Principles of Nuclear Magnetism*. 1961, Oxford: Clarendon Press.
3. Leskowitz, G.M., L.A. Madsen, and D.P. Weitekamp, *Force-detected magnetic resonance without field gradients*. Solid State Nuclear Magnetic Resonance, 1998. **11**(1-2): p. 73-86.
4. Purcell, E.M., H.C. Torrey, and R.V. Pound, *Resonance Absorption by Nuclear Magnetic Moments in a Solid*. Physical Review, 1946. **69**: p. 37.
5. Bloch, F., W.W. Hansen, and M. Packard, *The Nuclear Induction Experiment*. Physical Review, 1946. **70**: p. 474.
6. Rabi, I.I., *et al.*, *A New Method of Measuring Nuclear Magnetic Moment*. Physical Review, 1938. **53**: p. 318.
7. Gozzini, A. *Proc. XII Colloque Ampere*. in *XII Colloque Ampere*. 1963. Bordeaux.
8. Alzetta, G., *et al.*, *Paramagnetic Resonance Experiments at Low Fields with Angular-Momentum Detection*. Il Nuovo Cimento, 1967. **52 B**(2): p. 392.
9. Weitekamp, D.P. and P.J. Pizarro, *Method and apparatus for highly sensitive spectroscopy of trapped ions*, 1991, California Institute of Technology: US.
10. Pizarro, P.J. and D.P. Weitekamp, *Magnetic resonance of trapped ions by spin-dependent cyclotron acceleration*. Bull. Magn. Reson., 1992. **14**: p. 220-223.
11. Sidles, J.A., *Noninductive Detection of Single-Proton Magnetic-Resonance*. Applied Physics Letters, 1991. **58**(24): p. 2854-2856.
12. Zuger, O. and D. Rugar, *1st Images From a Magnetic-Resonance Force Microscope*. Applied Physics Letters, 1993. **63**(18): p. 2496-2498.
13. Rugar, D., *et al.*, *Force Detection of Nuclear-Magnetic-Resonance*. Science, 1994. **264**(5165): p. 1560-1563.
14. Sidles, J.A., *et al.*, *Magnetic-Resonance Force Microscopy*. Reviews of Modern Physics, 1995. **67**(1): p. 249-265.

15. Zuger, O., *et al.*, *Three-dimensional imaging with a nuclear magnetic resonance force microscope*. Journal of Applied Physics, 1996. **79**(4): p. 1881-1884.
16. Bruland, K.J., *et al.*, *Force-detected magnetic resonance in a field gradient of 250 000 Tesla per meter*. Applied Physics Letters, 1998. **73**(21): p. 3159-3161.
17. Leskowitz, G.M., *Force-Detected Magnetic Resonance Independent of Field Gradients*, Chemistry Ph.D. 2002, California Institute of Technology: Pasadena, CA.
18. Madsen, L.A., Leskowitz, G. M., and Weitekamp, D. P., *Observation of Force-Detected Nuclear Magnetic Resonance in a Homogeneous Field*. Manuscript In Preparation, 2002.
19. Sarid, D., *Scanning Force Microscopy*. 1991, New York: Oxford University Press.
20. Yannoni, C.S., *et al.*, *Force Detection and Imaging in Magnetic Resonance*, in *Encyclopedia of Nuclear Magnetic Resonance*, D.M. Grant and R.K. Harris, Editors. 1996, John Wiley: New York.
21. Hibbs, A.D., *et al.*, *A Squid-Based Ac Susceptometer*. Review of Scientific Instruments, 1994. **65**(8): p. 2644-2652.
22. Carr, H.Y. and E.M. Purcell, *Effects of Diffusion on Free Precession in Nuclear Magnetic Resonance Experiments*. Physical Review, 1954. **94**(3): p. 630-638.
23. Weitekamp, D.P., *Time-Domain Multiple-Quantum Nmr*. Advances in Magnetic Resonance, 1983. **11**: p. 111-274.
24. Rhim, W.-K., D.P. Burum, and D.D. Elleman, *Multiple-Pulse Spin Locking in Dipolar Solids*. Physical Review Letters, 1976. **37**(26): p. 1764-1766.
25. Ernst, R.R., G. Bodenhausen, and A. Wokaun, *Principles of nuclear magnetic resonance in one and two dimensions*. International Series of Monographs on Chemistry. 1987, Oxford: Clarendon Press.
26. Mansfield, P. and P.K. Grannell, *NMR 'diffraction' in solids?* Journal of Physics C, 1973. **6**(22): p. L422-L426.
27. Lauterbur, P.C., *Image Formation by Induced Local Interactions: Examples Employing Nuclear Magnetic Resonance*. Nature, 1973. **242**: p. 190.
28. Damadian, R., *Science*, 1971. **171**: p. 1151.

29. McCombie, C.W., *Fluctuation Theory in Physical Measurements*. Rep. Prog. Phys., 1953. **16**: p. 266-320.

30. Hoult, D.I. and R.E. Richards, *The Signal-to-Noise Ratio of the Nuclear Magnetic Resonance Experiment*. J. Magn. Reson., 1976. **24**: p. 71-85.

31. Stowe, T.D., *et al.*, *Attoneutron force detection using ultrathin silicon cantilevers*. Applied Physics Letters, 1997. **71**(2): p. 288-290.

32. Yasumura, K.Y., *et al.*, *Quality factors in micron- and submicron-thick cantilevers*. Journal of Microelectromechanical Systems, 2000. **9**(1): p. 117-125.

33. Roukes, M.L. *Nanoelectromechanical Systems*. in *Solid-State Sensor and Actuator Workshop*. 2000. Hilton Head Island, South Carolina.

34. Webb, A.G., *Radiofrequency microcoils in magnetic resonance*. Progress in Nuclear Magnetic Resonance Spectroscopy, 1997. **31**: p. 1-42.

35. Seeber, D.A., *et al.*, *Design and testing of high sensitivity microreceiver coil apparatus for nuclear magnetic resonance and imaging*. Review of Scientific Instruments, 2001. **72**(4): p. 2171-2179.

36. *Nastran FEM Package*, MSC Software, <http://www.mscsoftware.com/>. 2002, Santa Ana, CA.

37. *Ansys Software Package*, Ansys Inc., www.ansys.com/. 2002, Canonsburg, PA.

38. Terman, F.E., *Radio Engineers' Handbook*. 1943, New York: McGraw-Hill.

39. George, T., *et al.* *MEMS-based force-detected nuclear magnetic resonance spectrometer for in situ planetary exploration*. in *2001 IEEE Aerospace conference*. 2001. Big Sky, Montana.

40. Zener, C., *Internal Friction in Solids. II. General Theory of Thermoelastic Internal Friction*. Phys. Rev., 1938. **53**: p. 90-99.

41. Lifshitz, R. and M.L. Roukes, *Thermoelastic damping in micro- and nanomechanical systems*. Phys. Rev. B, 2000. **61**(8): p. 5600-5608.

42. Stowe, T.D., *et al.*, *Silicon dopant imaging by dissipation force microscopy*. Appl. Phys. Lett., 1999. **75**(18): p. 2785-2787.

43. Carson, P.J., *et al.*, *Method for suppressing noise in measurements*, 1999, California Institute of Technology (Pasadena, CA): United States.

44. Weitekamp, D.P. *Mechanical Cavity Quantum Electrodynamics: Ordering Spins by Enhanced Spontaneous Emission*. in *International Society of Magnetic Resonance in Medicine: Workshop on Sensitivity and Detection*. 2001. San Francisco, CA.
45. Madsen, L.A., G.M. Leskowitz, and D.P. Weitekamp. *Design Principles for a Force-Detected Magnetic Susceptometer*. Bull. Am. Phys. Soc., 1997. **43**: p. 937.
46. Guoy, L.G., Compt. Rend., 1889. **109**: p. 935.
47. Kirtley, J.R. and J.P. Wikswo, *Scanning squid microscopy*. Annual Review of Materials Science, 1999. **29**: p. 117-148.
48. Wickenden, D.K., *et al.*, *Development of miniature magnetometers*. Johns Hopkins Apl Technical Digest, 1997. **18**(2): p. 271-278.
49. Stipe, B.C., *et al.*, *Magnetic dissipation and fluctuations in individual nanomagnets measured by ultrasensitive cantilever magnetometry*. Physical Review Letters, 2001. **86**(13): p. 2874-2877.
50. Weiss, B.P., *et al.*, *A low temperature transfer of ALH84001 from Mars to Earth*. Science, 2000. **290**(5492): p. 791-795.
51. Carson, P.J., *et al.*, *Correlated Observation Narrows Quantum Uncertainty Enhancing Spectroscopic Transients*. Bulletin of the American Physical Society, 1999. **44**: p. 541.
52. Weissbluth, M., *Photon-Atom Interactions*. 1989: Academic Press.
53. Sleator, T., *et al.*, *Nuclear-Spin Noise and Spontaneous Emission*. Physical Review B-Condensed Matter, 1987. **36**(4): p. 1969-1980.
54. McCoy, M.A. and R.R. Ernst, *Nuclear-Spin Noise At Room-Temperature*. Chemical Physics Letters, 1989. **159**(5-6): p. 587-593.
55. Gueron, M. and J.L. Leroy, *Nmr of Water Protons - the Detection of Their Nuclear-Spin Noise, and a Simple Determination of Absolute Probe Sensitivity Based On Radiation Damping*. Journal of Magnetic Resonance, 1989. **85**(1): p. 209-215.
56. Carson, P.J., *et al.*, *Taming Spin Noise by Detecting Multiple Time-Correlated Operators*. In Preparation, 2002.

57. Madsen, L.A., *Simulation of NMR on Single or Few Spins Using Two-Point Measurement to Beat the Boltzmann Average*, 1997, California Institute of Technology: Pasadena, CA, v. 9.

Chapter 2: Design of Millimeter-Scale and Micron-Scale BOOMERANG Instruments

2.1 *Composite Magnet Assembly for Optimal NMR Detection*

We seek to design an assembly of magnets that create a field throughout the sample with homogeneity sufficient for coherent control over all spins in the sample, and with optimal sensitivity to the sample's magnetic moment. These two issues are intertwined in that the BOOMERANG concept allows the possibility of whole-sample coherent spin manipulations, thus providing excellent sensitivity. Our prototypical composite magnet assembly has inherent symmetry to produce vastly superior homogeneity compared with previous schemes designed to optimize the field gradient at the sample [1]. Thus, we recognize, to a good approximation, that it is possible to separately optimize these two aspects, sensitivity and homogeneity. We may optimize our detector first for sensitivity and then fine tune the composite magnet assembly for best homogeneity.

Design of a mechanical oscillator suspension also weighs heavily on the effectiveness of these instruments. In order to maximize sensitivity, we aim for an oscillator suspension light compared to the detector magnet to minimize motional mass. We must also minimize dissipation by using low-loss materials and by considering the dependence of damping on geometry. Several theories of mechanical oscillator losses are available but do not provide adequate predictions for specific oscillator designs, so we have used experimental observations (our own, and those of others) to add to our strategies for improving dissipation quality. Eddy currents in the composite magnet assembly also provide important damping mechanisms that we are striving to understand

and minimize through novel magnet materials and geometric design [2,3,4]. Figure 2.1.1 shows our practical implementation of a BOOMERANG detector assembly in its simplest form.

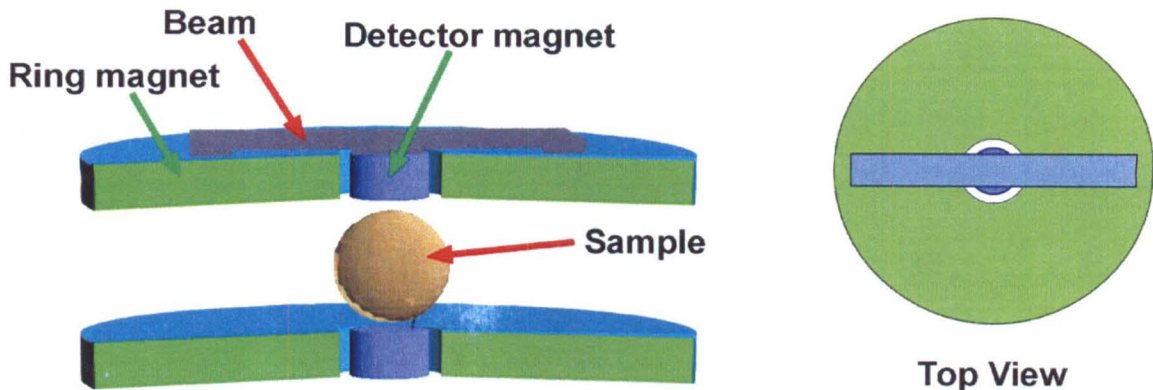


Figure 2.1.1: BOOMERANG Detector Assembly. This diagram depicts the basic elements of the prototypical BOOMERANG detector. The mechanical oscillator consists of the sensitivity-optimized detector magnet mounted on the oscillator suspension, in this case a beam fixed at both ends. The desired sample size determines the size of the detector magnet. The ring magnet and the symmetric pair of magnets below the sample produce a net homogeneous field across the sample, cancelling all odd-order field inhomogeneity terms as well as the second-order term. Ultimately, homogeneity is limited by the gap between the detector magnet and the ring magnet. The height and diameter of the detector magnet, the gap between the detector and ring magnets, the distance from the sample center to the edge of the detector magnet, and the equilibrium position and resonance properties of the detector oscillator are the key adjustable parameters in optimization of this design for sensitivity and homogeneity. The position of the detector magnet shown coplanar with the ring magnet corresponds to the equilibrium position where field homogeneity is optimized.

This detector also requires a sensitive displacement sensor capable of observing the thermal (Brownian) motion of the mechanical oscillator. Although I describe several possibilities for this sensor, the fiber-optic interferometer pioneered by Rugar [5] provides the most convenient method for single-detector BOOMERANG experiments

where the area of the moving parts are much larger than λ^2 for optical wavelength λ . Experiments utilizing arrays of BOOMERANG detectors may encourage other sensor designs. In section 2.3.B, I detail a transverse fiber-optic interferometer, which allows displacement sensing in geometrically restricted BOOMERANG designs, as well as convenient sensing for AFM instruments and other applications [6].

Incorporation of this BOOMERANG detector assembly into an NMR spectrometer also requires design of rf excitation and data acquisition subsystems. Since we have constructed these subsystems using nominally standard designs followed by iterative experimental improvements, I describe these systems in detail in Chapter 3. However, I comment at the end of this chapter on the special requirements and general forms of these systems when used for BOOMERANG detection.

2.1.A Detector Magnet for Optimal Detection Sensitivity

We begin the design procedure by answering the question of the shape and size of the sensor magnet [1]. We must trade off increases in its size, which increases the total force of interaction with the sample, with minimization of its inertial mass, which allows greater displacements by the weak spin-dependent forces. In brief, the quantity to optimize is the ratio of the magnetic force to the square root of the motional mass, as follows from considering the dominant Brownian noise contribution. For ease of manufacture, we constrain the detector magnet shape to be a right circular cylinder. We have found [4] that a “mushroom cap” shape produces better force sensitivity by a factor of ~ 1.5 , but presents more of a fabrication challenge to achieve sufficient field homogeneity. In order to optimize sensitivity, we must also use a magnet material with the highest possible saturation magnetization M_s . Iron and alloys of cobalt, iron, and/or

nickel provide the highest known M_s values, and our goal is to reach $M_s = 2 \text{ T}/\mu_0$ in our devices.

Beginning with equation 1.2.2, we calculate the signal-to-noise ratio for a cylindrical detector magnet with radius a and height b interacting with a spherical sample at distance R_{max} between the center of the sample and the closest point on the surface of the detector magnet. We then fix R_{max} at a reasonable distance, set by the desired sample radius plus the clearance needed for a sample container and other practical considerations. Finally, a plot of SNR vs. both a and b allows us to extract the magnet dimensions. These dimensions are scale-invariant with respect to force sensitivity. That

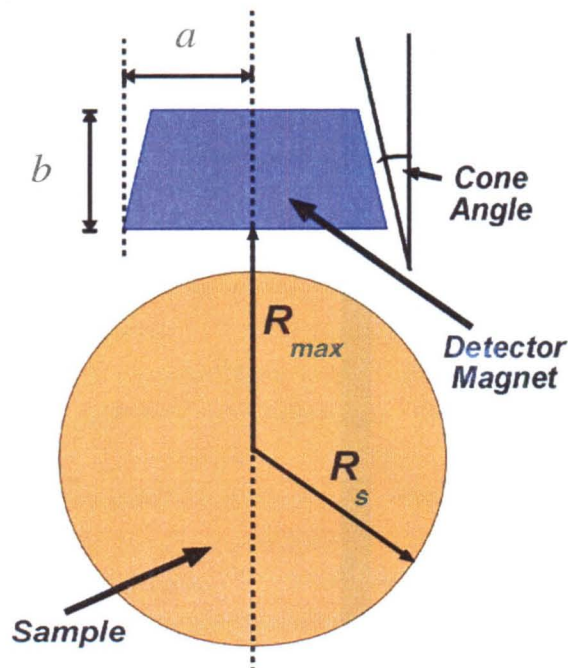


Figure 2.1.2: Detector Magnet and Relevant Optimization Parameters. We optimize the detector magnet dimensions as shown relative to the sample radius R_s , and the distance R_{max} from the sample center to the closest point on the detector magnet. While the cone angle is not included in our analytic optimization or current designs, improvements in sensitivity are possible by adjusting it to remove magnetic material less important to the magnetic force. We may tailor this cone angle freely on the macro scale, and to a lesser extent in microfabricated devices.

is, once we design a detector magnet for a given sample size, the aspect ratio and size of the detector magnet scale proportionally with the desired sample size. I point out these dimensions in figure 2.1.2, with the addition of the cone angle, which we do not optimize in this calculation, but allows modest gains in sensitivity. Addition of this cone angle

complicates matters of static magnetic force and homogeneity since a conical detector magnet at the top of its magnetic potential hill is not coplanar with the ring magnet (see sections 2.1.D and 2.2.D below).

For this optimization, we have also ignored explicit issues of field homogeneity, except in the choice of the detector magnet shape, and we have assumed that the detector magnet dominates the mass of the mechanical oscillator. These assumptions simplify our calculations and provide magnets with approximately the correct dimensions. The next step in this optimization is to include the effective motional mass of the oscillator suspension, which experimentally has been $< 10\%$ of the oscillator motional mass for 3 mm-scale oscillators, but may be as high as 50% of the oscillator motional mass for 60 μm -scale oscillators (see Chapter 4 oscillator designs). We may also make substantial gains in homogeneity for only modest decrease in sensitivity by making the detector magnet shorter but larger in diameter. Indeed, the sensitivity penalty for changing the aspect ratio of the detector magnet is relatively small, such that we have considerable flexibility in detector-oscillator designs should practical issues prevent manufacture of the optimal detector magnet on a low-dissipation suspension. Assuming a right-circular cylindrical detector magnet, $R_{max} = 1.13 R_s$ (see next section), and a negligible suspension mass, we obtain the scale-invariant results that $b = 0.9 a$, and $a = 0.59 R_{max}$. For a more formal discussion of the BOOMERANG detector magnet optimization procedure, I refer the reader to the Ph.D. Thesis of Garett M. Leskowitz [4].

2.1.B Homogeneity, Forces, and Practical Manufacture

Three design criteria, in addition to sensitivity, can be met by modifying the geometry of a BOOMERANG magnet assembly. First, we require that the magnetic field

at the sample be as homogeneous as possible, given machining tolerances and shimming capabilities, in order to provide a narrow NMR spectral line. Second, the magnet array is designed so that the net magnetic force on the detector magnet, at the equilibrium position of the membrane and in the absence of nuclear magnetization in the sample, is less than and opposite to the force that may be applied by a suitable force-feedback transducer, which is present in some, but not all designs. Finally, the dimensions of the membrane are determined so as to counteract the negative-curvature magnetic forces while providing an oscillator resonance frequency of $\sim 1\text{kHz}$, low enough to allow readily achievable efficient spin inversion. A capacitance force transducer described in section 2.2.C below provides the ability both to tune the resonance frequency and the detector magnet's equilibrium position.

By considering a Legendre expansion of the z -axis magnetic field of an assembly of magnets, and relying on the symmetry of two permanent magnet pole pieces, we arrived at the symmetric BOOMERANG detector design. Since the magnet assembly has a symmetry plane passing through the sample center and perpendicular to the z -axis, and has cylindrical symmetry about the z -axis, all odd-order terms in the expansion are zero. By approximating the assembly as a pair of poles with infinitesimally thin cylindrical slices removed, a pole-separation distance exists where the second-order term d^2B/dz^2 is also zero. Thus we are left with only even, fourth-order and higher terms in the magnetic field. This also assumes that the detector and ring magnets on both sides of the sample are perfectly coplanar and concentric. Since practical concerns limit the minimum gap width between the detector and ring (field compensation) magnets, we must balance homogeneity with the need for attaining a practical, low-dissipation (high- Q_h) oscillator.

Forces on the detector magnet arise from: 1) magnetic fields associated with the magnet array, 2) the mechanical membrane to which the sensor magnet is attached, 3) the dipole-dipole force due to the sample dipole moment, 4) thermal (Brownian) noise, 5) gravity, and 6) feedback forces applied by a capacitive or other force transducer. The sum of these contributing terms gives the net force F_{net} on the detector magnet:

$$F_{net} = F_{magnetic} + F_{elastic} + F_{sample} + F_{noise} + F_{gravity} + F_{feedback}. \quad 2.1.1$$

The static force due to gravity $F_{gravity}$ is of the same order as the tiny alternating signal force applied by the sample's magnetization F_{sample} , thus we may neglect it. I describe the sample force F_{sample} and thermal noise force F_{noise} in section 1.2.E above on sensitivity and scaling. I detail the relevant static magnetic, elastic, and feedback forces in sections 2.1.D, 2.2.A, and 2.2.D below.

The distance R_{max} of closest approach of the detector magnet to the sample center should be dominated by the sample radius, but includes additional contributions from the rf coil, sample holder or shuttle, vacuum wall, and any sample spinning apparatus. Our original designs assume that we can make $R_{max} = 1.13 * R_s$ by careful design of the rf probe, sample holder, and vacuum wall. Note that desirable rf coil designs will take no space between the sample and detector magnet, and might consist of rectangular wires defined above and below the sample directly onto the BOOMERANG detector substrate. We have also calculated that a vacuum wall of $< 0.05 * R_s$ covering the detector magnet can adequately isolate it from ambient pressure. We may also increase the distance from sample center to the opposing (possibly unused) detector assembly without penalty except for larger static field magnets needed to maintain homogeneity in the increased gap between the detector assemblies.

2.1.C Finite-Element Method Calculations for Optimal Field Homogeneity

Using Legendre expansions of the magnetic field produced by cylindrically symmetric magnet elements and applying the superposition principle, we began magnet designs by analytically generating z-axis plots of the magnetic field across the sample using Mathematica © [4, 7]. We then optimized the field homogeneity and the net magnetic force due to the assembly by iterative application of the Maxwell © software, a commercial finite-element-method (FEM), electro- and magnetostatic analysis package [8]. This program numerically solve Maxwell's equations for arbitrary magnet geometries and produces magnetic field plots as well as net forces on specified objects. Field plots calculated using Maxwell © agree at the sub-part-per-thousand level with analytically computed field plots for magnet arrays based on right circular cylinders and uniform magnetization. We have carried out these calculations self consistently to verify field convergence to the sub-part-per-million level.

As described, we fix the height of the detector and ring magnets along the z -direction, the diameter of the detector magnet, and the distance between the two opposing detector magnets based on the size of the proposed sample. Decreasing the gap between the detector magnet and the concentric ring magnet improves the field homogeneity. Intuitively, the most homogeneous field would be obtained by making this gap zero, thus yielding a solid circular disk. The lower limit on this gap depends on the minimum fabrication tolerances, such that no frictional contact occurs between the detector magnet and the ring magnet, thus quenching the Q_h of the oscillator.

Centering the detector magnet vertically in the bore of the ring magnet so that their upper and lower surfaces are coplanar produces the best field homogeneity. Modification of the cone angle creates large changes in the magnetic force on the detector magnet, which supports our choice in using the right-cylindrical shape.

Changing the height of the static field magnets changes the field strength, but has little effect on the field homogeneity at the sample, whereas changing the static field magnets' distance from the sample along the z-axis alters both the field strength and the homogeneity dramatically. By increasing the height of the static field magnets and keeping their diameter constant, the field strength may be increased with only a several ppm change in homogeneity at the sample. This effect may be compensated by using the shim magnet described in section 2.1.E below, or by small adjustment of the inter-magnet positions. In general, field homogeneity is most strongly affected by changes in the magnetic material within several sample radii away from the center of the sample. In Chapter 3, I list the optimized prototype spectrometer dimensions as determined by Maxwell simulations, and verified by experiments.

2.1.D Negative Magnetic Spring Constant

The homogeneous-field magnet array of fig. 2.1.1 places the detector magnet in a potential for z -axis displacement with negative curvature. The detector magnet, for small displacements, experiences a magnetic force $F_{magnetic}$ proportional to the distance from the unstable equilibrium position (the top of the potential “hill”), and we may think of this magnetic force as having a “negative” harmonic spring constant $k_{magnetic}$. Thus, using the sign convention of standard harmonic oscillators,

$$F_{magnetic} = -k_{magnetic}z + F_{magnetic}(0),$$

2.1.2

where a negative $k_{magnetic}$ gives a repulsive force from the equilibrium position, and $F_{magnetic}(0)$ represents an offset force on the detector magnet. $F_{magnetic}(0)$ is due to any asymmetry of the magnets along the axis of motion and about the center of the detector magnet, such as the detector magnet cone angle described above. Ideally, $F_{magnetic}(0) = 0$ when the detector magnet sits in its best position for field homogeneity, *i.e.*, when the magnet planes are coplanar with the ring magnet planes, and is approximately the case for right-cylindrical detector and ring magnets. The oscillator's net spring constant k_{net} encompasses the positive elastic force constant $k_{elastic}$ and the negative magnetic force

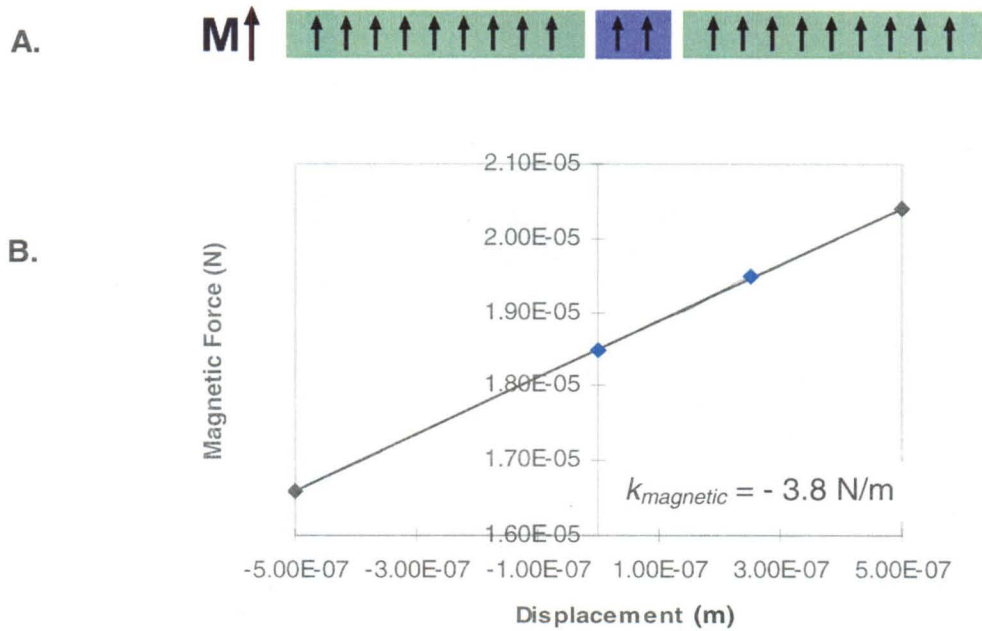


Figure 2.1.3: Magnetic Force vs. Detector Magnet

Displacement. Part A shows a cross-section of the BOOMERANG assembly with magnetization highlighted. The slope of the line plotted in part B is the negative of the magnetic spring constant $k_{magnetic}$ for the oscillator in a micro-scale spectrometer design. This simulation using Maxwell [8] assumes $M = 0.94 \text{ T}/\mu_0$ for the detector assembly, a detector magnet of radius 50 μm and height 50 μm , a cone-angle of 11° , and a detector-ring gap of 1 μm .

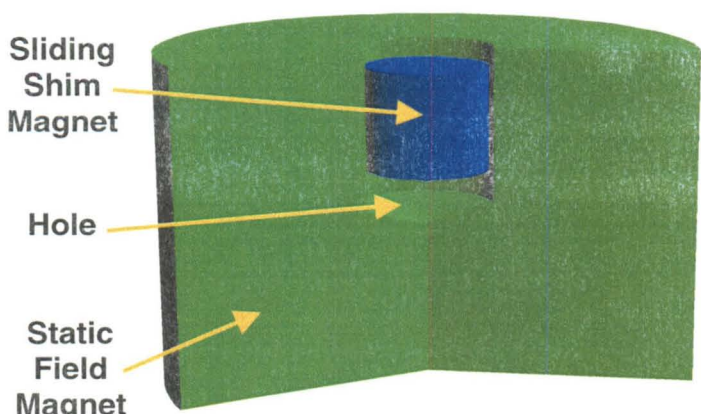
constant $k_{magnetic}$, and the resonance frequency ω_h is given by $\omega_h = \sqrt{k_{net}/m}$. We choose the force constant for the membrane $k_{elastic}$ to be slightly larger in magnitude than the negative magnetic spring constant such that the resonance frequency for the system is $\approx 1\text{kHz}$ (see also section 2.2.D).

For each trial design, I obtained the negative magnetic spring constant numerically using the Maxwell software [8] by calculating the forces on the detector magnet for several positions along its axis of vibration while keeping all other geometric parameters constant. Figure 3 shows a plot of the magnetic force on the detector magnet versus displacement from its equilibrium position, generated for a micron-scale detector design. Note that for small displacements, well within the range of desired oscillator motion, this plot is quite linear. For the macro-scale prototype spectrometer with 1.5 mm-radius detector magnet at $\mathbf{M} = 0.7 \text{ T}/\mu_0$, the predicted $k_{magnetic}$ is -6200 N/m .

2.1.E Permanent Magnet Shims

Based on tolerances set by the microfabrication process and the materials involved, we have investigated the use of permanent magnet shims for post-fabrication

Figure 2.1.4: Static Field Magnet with Shim Magnet. This cutaway view shows one of the static field magnets with a hole drilled in it. A cylindrical magnet inside the hole can slide in or out to allow fine tuning of the magnetic field homogeneity as well as the static force on the detector magnet.



optimization of the magnetic field across the sample. By incorporating a hole and sliding shim magnet into the permanent static-field magnets, as shown in figure 2.1.4, we may null quadratic inhomogeneity terms in the magnetic field after fabrication, or trim the magnetic force on the detector magnet. These benefits come at the cost of removing magnetic material from the main field magnets, which slightly reduces the field strength at the sample. For each combination of detector assembly and static field magnet properties, *i.e.*, sizes, shapes, locations, and magnetizations, numerical optimization of the shim geometry is necessary to achieve best shimming quality and tuning range.

2.2 Mechanical Oscillator Structures

We have investigated several oscillator suspension geometries that are compatible with the optimal BOOMERANG detector. We have required that the suspension constrain the detector magnet motion along the z -axis, that it have torsional rigidity sufficient to prevent the detector magnet from torquing in its bore and touching the ring magnet, and that it allow for low-dissipation oscillations in the desired ~ 1 kHz frequency range given that it must also counteract the negative magnetic force constant inherent in the BOOMERANG magnet assembly. Initially, we designed and experimented with circular membranes clamped around their circumference with the detector magnet fixed to the center of the membrane, but these designs exhibited poor ringdown times. Due to much higher observed ringdown times and ease of fabrication, we have instead chosen to use rectangular beams clamped at both ends with the detector magnet fixed to the center. At the end of this section, I describe several other oscillator designs, such as “xylophone” resonators, which present opportunities for lower dissipation or increased design freedom.

In order to compensate for variances in dimensions and material and magnetic properties in real devices, it will almost certainly be desirable to incorporate a real-time force-feedback system to control oscillator position and frequency. We have designed a novel three-plate capacitive transducer to fulfill this purpose in our prototype spectrometer, as well as in the micron-scale device.

2.2.A Loaded Beams and Plates

Theoretical determination of the elastic spring constant for the mechanical oscillator is required in order to accurately design beam dimensions. We must also counter balance the negative magnetic spring constant due to the magnetic array such that the net force constant k_{net} gives a resonance frequency in the audio range. Here, I outline the issues involved in determining oscillator beam dimensions.

We seek to design oscillator suspensions with the following properties: inertial mass small compared to that of the detector magnet, low mechanical dissipation, high torsional rigidity to counteract magnet rotation, robustness under shock loading, and low internal stress.

Our current beam geometry is that of a beam rigidly fixed at both ends with a mass at its center. In the presence of only elastic forces, we may calculate fundamental-mode resonance frequencies v_h (in Hz) for beams such as these, assuming a point mass at the center, by using the analytically derived formula given by Pilkey [9] as

$$v_h = \frac{4}{\pi} \left(\frac{3EI}{L^3(m_{mag} + 0.37m_{beam})} \right)^{1/2}, \quad 2.2.1$$

where E is the Young's modulus, L is the length of the beam, m_{mag} and m_{beam} are the masses of the magnet and beam, and I is the polar moment of inertia of the plate given by

$$I = \frac{1}{12}wh^3, \quad 2.2.2$$

where w is the width of the beam and h is its thickness. All parameters are in SI units.

This formula uses the Euler-Bernoulli approximations, essentially that there are only very small deflections of the beam and that the beams are purely linearly elastic. The reader should consult Pilkey [9], Leissa [10], or Roark [11] for more information. For our millimeter-scale and micron-scale devices observed to date, this theory agrees to within 5% of the measured values for oscillators with assumedly no internal stress.

In order to guide oscillator suspension design for a given size detector magnet, I note several scaling properties for the fundamental frequencies of these loaded rectangular beams. Assuming that the Young's modulus of the beam material is scale-invariant [12, 13] (see also section 2.2.D) and that a fixed-mass magnet dominates the mass of the oscillator, we examine equations 2.2.1 and 2.2.2 to find that ν_h scales approximately as $w^{1/2}$, as $L^{-3/2}$, and as $h^{3/2}$. We also note that when scaling all oscillator dimensions together (magnet included), ν_h scales as the inverse of the length scale, or $1/r$, a general result which holds when $k_{magnetic}$ is also included. The ratio of positive and negative force constants must be decreased to maintain ν_h at smaller length scales, as detailed in section 2.2.D.

In the existing micron-scale BOOMERANG detector designs discussed in Chapter 4, we incorporate an additional rigid mass in the form of a stress buttress to counteract stress in the electrodeposited detector magnet. Although equation 2.2.1 approximates this case as well, where m_{mag} would also include the stress buttress mass, this structure is

more accurately described as having a rigid strip mass at the center of the beam. If a design requires more accurate frequency predictions, we may follow Leissa's numerical study of this problem [10]. Leissa provides some numerical curves for the fundamental frequency parameter λ , but they do not allow interpretation sufficient for better than 5% accuracy in the range of dimensions for our oscillators. While this method may provide more accuracy, it is likely not necessary given the practical manufacturing tolerances and the tunability afforded by the capacitive feedback transducer described below.

Prior to experiments with circular membranes and rectangular beams, I applied the numerical studies of Leissa [10] and of Grossi *et al.* [14] to determine the thickness and diameter of centrally loaded circular membranes to predict elastic spring constants. Since preliminary experiments indicated that membranes would yield poor, high-dissipation oscillators, we abandoned them in favor of rectangular beams. In the event of renewed interest in membranes, I encourage the reader to consult Pilkey [9] and Leissa [10] for calculation methods.

2.2.B Oscillator Suspension Materials

To optimize the maximum signal power, the ringdown time τ_h of the oscillator (and similarly the quality factor Q_h) should be as large as possible. Oscillator suspensions made of single-crystal silicon have the lowest observed dissipation in MEMS devices, and thus typically have the highest sensitivity to resonant forces [15]. Boron-doped silicon, silicon nitride, silicon dioxide, and gallium arsenide may also form sufficiently low dissipation oscillators, given that many effects, such as eddy currents, contribute to the total mechanical dissipation. These materials may also provide simple fabrication pathways, and may be more robust to shock (*e.g.*, silicon nitride [16]) than single-crystal

silicon. I give the room-temperature material parameters for silicon, silicon dioxide, and silicon nitride in Table 2.2.1, where E is Young's modulus, ν the Poisson ratio, ρ the density, C_p the heat capacity at constant pressure, χ the thermal diffusivity, and α the thermal expansion coefficient [17-20]. These last three properties are important for calculations of thermoelastic damping, as well as possible thermal expansion and conduction issues. While these constants may not accurately simulate the material properties of all microfabricated films, they serve as a guide for determining a given oscillator's elastic spring constant. Material properties for elastic constant predictions should be updated as data or literature becomes available on materials resulting from specific microfabrication processes.

Material	E (GPa)	ρ (g/cc)	ν	C_p (J/m ³ -K)	χ (cm ² /s)	α (1/K)
Si	190	2.33	0.3	1.70E+06	0.9	2.60E-06
Si_3N_4	126	3.44	0.33	1.80E+06	0.018	3.00E-06
SiO_2	72	2.2	0.16	2.20E+6 *	0.01	5.50E-07

Table 2.2.1: Material Properties of Oscillator Suspension

Materials. E , ρ , and ν allow calculations of oscillator elastic properties, while C_p , χ , and α are necessary for thermoelastic damping calculations [17-20]. (* - taken at 533 K).

2.2.C Oscillator Feedback Transducer

We have designed a novel three-plate capacitance transducer array to fill two distinct roles. Its DC voltages are used to make adjustments to the oscillator's

equilibrium position as well as its resonance frequency. In addition, a feedback voltage derived from the displacement sensor signal may be applied to this capacitor to keep the sensor magnet stationary during NMR driving. This voltage would be applied at the oscillator resonance frequency and would be proportional to the sensor magnet's amplitude in the absence of feedback. I optimized the geometry of this "split-ring" transducer design shown in figure 2.2.1 using the Maxwell © electrostatic simulator [8]. The dimensions used for calculations in Maxwell were that the bottom plate (detector magnet) was 60 μm diameter, the inner top plate was 65 μm diameter, and the outer top plate was 85 μm ID and 120 μm OD. For the lower curve, $V_1 = -5 \text{ V}$, $V_2 = +5 \text{ V}$, and $V_3 = -5 \text{ V}$, and for the upper curve, they were $V_1 = -5 \text{ V}$, $V_2 = +5 \text{ V}$, and $V_3 = +5 \text{ V}$.

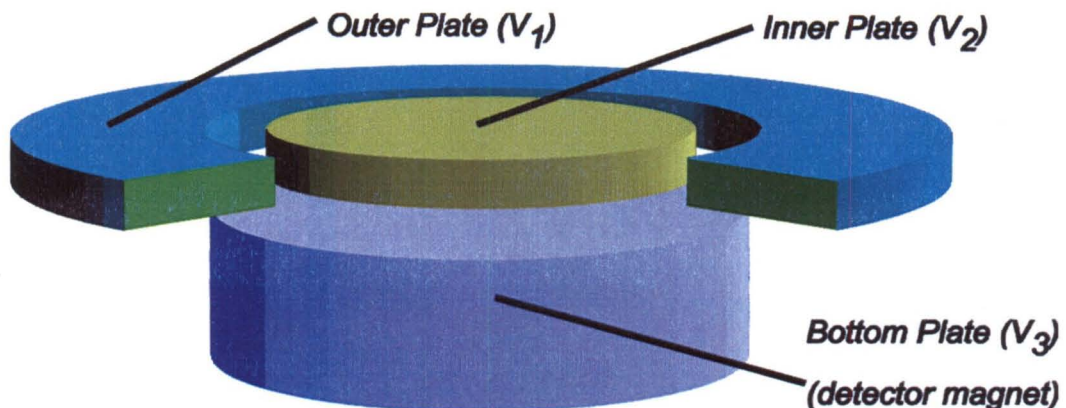


Figure 2.2.1: Split-Ring Capacitance Transducer.

The upper plate consists of an inner disk and a concentric outer ring while the lower plate is simply the conducting detector magnet. We may make forces between the upper and lower plates attractive at small plate separations and repulsive at large separations by choosing the outer upper plate and the lower plate voltages V_1 and V_3 to be the same sign and the middle upper plate voltage V_2 to be of opposite sign. Using these two independent voltage differences, we may tailor the detector magnet's equilibrium position and its resonance frequency.

There are two independent voltage differences chosen by setting the voltages \mathbf{V}_1 , \mathbf{V}_2 , and \mathbf{V}_3 . The resulting potential imposed by this split-ring capacitor has negative-

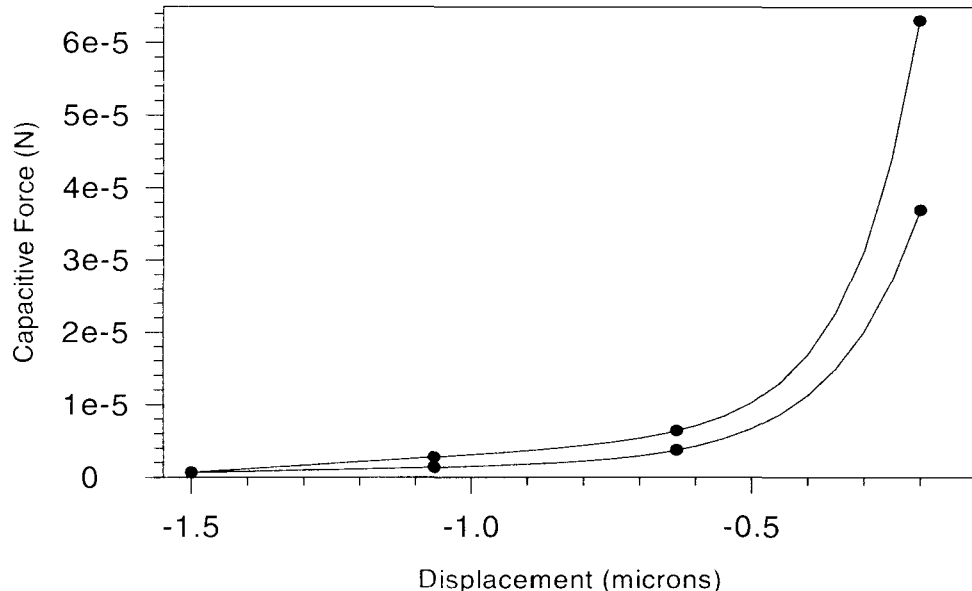


Figure 2.2.2: Capacitive Transducer Force on Oscillator. The abscissa is the distance from the top surface of the detector magnet to the split-ring electrodes (see fig. 2.2.1). The two curves correspond to application of different sets of voltages to the capacitor plates (see text). As evidenced by the curvature in the force vs. distance plots, one can, by judicious application of voltages, tune the negative force constant applied to the sensor magnet/membrane oscillator.

curvature and an approximately exponential dependence on position. A plot of the capacitive force on the sensor magnet, as a result of its being one plate of the capacitor, is shown in figure 2.2.2 as a function of the distance to the other plate containing the concentric disk and ring electrodes of fig. 2.2.1. Though I originally conducted simulations for the split-ring arrangement of capacitor plates, a more efficient and convenient arrangement incorporates three parallel planes as shown in figure 2.2.3. The beam contains one plate, while the other two plates lie in planes on either side of the

beam to greatly increase the applicable force via the increased surface area of the capacitor plates. Experiments on this arrangement are near completion using the prototype 3 mm BOOMERANG spectrometer. Prior to micron-scale implementation, it would be prudent to use Maxwell or similar FEM software to simulate applicable forces using this transducer geometry. Alternatively, the geometry of figure 2.2.3 approximates two parallel-plate capacitors [21], so that we may derive the simple formula

$$F_{capacitive} = \frac{AV^2\epsilon_0}{d^2}, \quad 2.2.3$$

where A is the area of the capacitor plate, V is voltage, d is the distance between the plates, and ϵ_0 is the vacuum permittivity, in order to make estimates of forces using this capacitor.

Using this capacitance transducer allows us to adjust the oscillator's resonance frequency, which eliminates the need for exact prior knowledge of $k_{magnetic}$ and $k_{elastic}$.

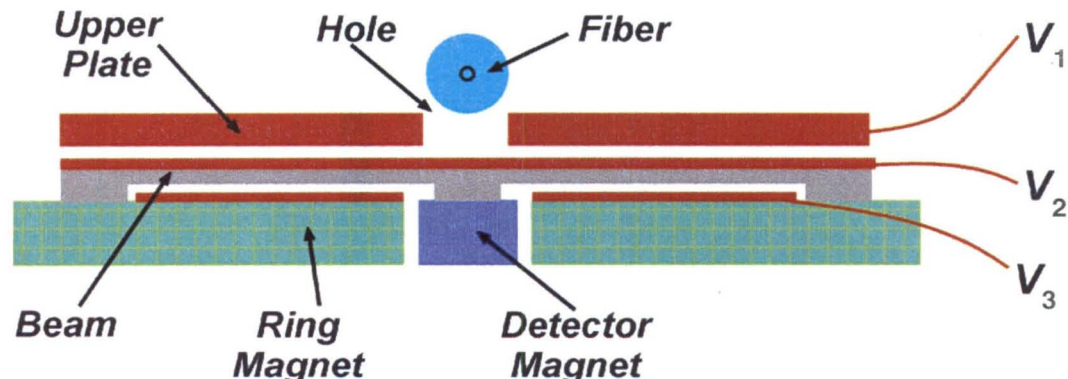


Figure 2.2.3: Capacitive Force Transducer Incorporated into the BOOMERANG Detector. This improved geometry (cross-section shown) for the capacitive force transducer allows application of greater forces because of its great surface area, and it integrates readily into the BOOMERANG detector. Both the ring magnet and the beam have conducting plates attached to them. The upper plate is attached to a support above the ring magnet, such as the static field magnet mount, and has a hole in it to accommodate a displacement sensor.

The negative curvature afforded by the transducer further allows the use of a stiffer, less fragile membrane without compromising the desired low resonance frequency.

2.2.D Oscillator Design Procedure: A Force Balancing Act

Assuming that the elastic modulus of the membrane material is scale invariant, v_h scales inversely with the length scale of the oscillator. This assumption, at least for silicon suspensions, appears to hold even down to the ~ 1 nm length scale [13]. Because of this elastic scaling and the scale-invariance of magnetic fields, for $v_h = 500$ Hz oscillators in the 3 mm design, the membrane force constant is on the order of the magnetic force

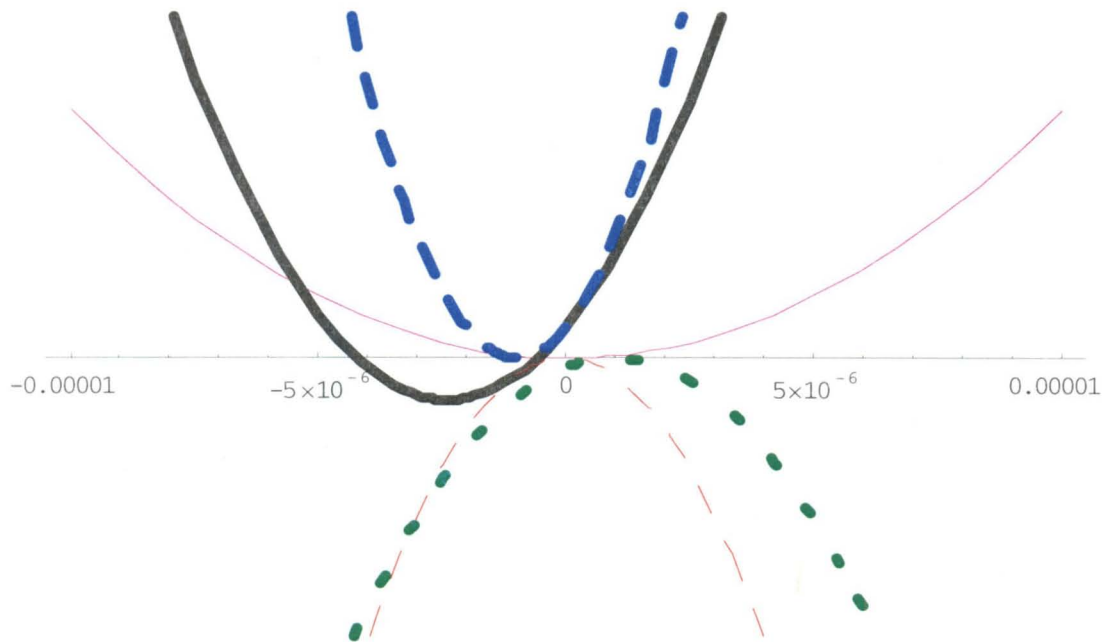


Figure 2.2.4: Elastic, Capacitive, and Magnetic Potentials for Oscillator Motion. These curves depict the potentials for the detector oscillator vs. oscillator displacement, where the $z = 0$ point corresponds to the detector magnet being coplanar with the ring magnet. The light dashed line and heavy dashed line show the magnetic and elastic potentials, respectively. The heavy solid curve shows the sum of the magnetic and elastic potentials with the unfavorable zero point offset. Applying the capacitive potential shown as the heavy dotted curve compensates this offset and controllably softens the mechanical mode to yield the net potential shown as the light solid curve.

constant. However, in micron-scale designs the elastic force constant needs to balance the magnetic force constant to within a few percent in magnitude in order to produce a v_h as low as 1 kHz. For the optimized 60 μm sample-size detector, $k_{net} = 0.2 \text{ N/m}$ yields $v_h = 1 \text{ kHz}$, and $k_{magnetic} \sim 1 \text{ N/m}$ depending on the magnet magnetizations and the particular detector-ring gap. This requirement appears difficult to satisfy without oscillator feedback, so we have designed the capacitive force transducer described above to allow fine tuning of the oscillator resonance frequency after fabrication is complete. Our design procedure is as follows. We calculate $k_{magnetic}$ for a desired magnet assembly, which depends on its dimensions, materials, and magnetization. We then specify the beam dimensions so that $k_{elastic}$ is larger than that necessary for a sub-10 kHz resonance frequency. The capacitive transducer may then be used to soften k_{net} to obtain the desired resonance frequency.

We must also attempt to build the elastic suspension such that its equilibrium position coincides with the top of the magnetic hill. Any incorporated mismatch between the zero points of these potential curves will cause the detector magnet to sit in an equilibrium position unfavorable to homogeneity. In other words, the oscillator suspension should be approximately at equilibrium when the detector magnet is in its “centered” position where it is coplanar with the ring magnet and homogeneity is optimal. As mentioned above, we may also cancel any residual offsets in equilibrium position using the capacitive transducer. Figure 2.2.4 shows example potentials for oscillator motion due to capacitive, magnetic, and elastic interactions. This example includes an elastic potential with a zero point offset, which when combined with only the magnetic potential causes a net potential with the detector magnet equilibrium position offset from

the optimal centered position. We may control the capacitive potential to compensate for this offset and to further soften the mechanical mode to produce a desired net oscillator potential.

This reduction in oscillator frequency by the use of negative magnetic and/or capacitive force constants allows use of much lower rf excitation powers during NMR driving as discussed in section 3.2.D, and may have fundamental importance for thermoelastic damping as discussed in section 1.2.F.

2.2.E Vibration Isolation

In order to ensure that ambient vibrations do not excite the oscillator, we keep in mind several concepts when designing BOOMERANG spectrometer structures and ancillary apparatus. First, we seek to design our supports and static field magnets such that all structural elements have high stiffness, *i.e.*, that they have resonance frequencies far above the range of the detector oscillator resonance. This technique allows for controllable vibration decoupling from the floor or earth, as detailed in the Ph.D. thesis of David Baselt on AFM design [22]. While we have not quantitatively applied this method to our own experimental devices, it has weighed into our thinking, and will play a part in future efforts. I further point out the particular necessity that the displacement sensor tip and any related positioning stage be rigidly fixed to the oscillator support.

Our first (successful) designs for support structure also incorporate an inertial mass large compared with the mechanical oscillator, and separated from the floor with a light, viscous suspension. This technique is ubiquitous in scientific instrumentation such as optical tables. I detail our specific support structures in section 3.1.A.

The final mode of vibration isolation involves removal of atmospheric acoustic transmission. Sound waves from assorted building air handlers, instrumentation fans, power supplies, etc., may travel directly through the air and excite the oscillator. Enclosing the entire spectrometer, including the displacement sensor, in a vacuum provides the best isolation from sound transmission, but it is likely only necessary to enclose the oscillator itself, assuming the supports are sufficiently rigid to isolate vibrations from the mechanical oscillator as described above. The other important reason for operation in a vacuum is to remove viscous air damping of the oscillator, which dominates oscillator damping at pressures above about 100 mTorr.

2.2.F Alternate Mechanical Oscillator Forms

Here I briefly mention other possible oscillator suspension designs. As mechanical oscillators attain lower dissipation, the suspension anchors and the particular deformations of the suspension elements become increasingly important in damping. We have considered designs that attempt to minimize these effects from many perspectives. One such idea is to use a “xylophone” resonator, which has anchor points at the nodes of the fundamental mode of a free rectangular beam. This minimizes the mechanical energy present at the anchor points, thus reducing acoustic transmission of energy there, and reducing deformation of the anchors themselves. A further sophistication lies in the use of nodal anchors that are one-quarter the wavelength of the mechanical mode, thus providing an impedance-mismatched condition for transmission of sound at the resonance frequency [23]. Such anchors are much larger than the entire device for micron-scale oscillators with audiofrequency resonances, so this design strategy gives no apparent benefits at this scale.

A simpler idea involving acoustic impedance mismatching involves thinning conventional clamped beams near the anchor points. Streckeisen et al. have measured improvements in ringdown time τ_h of up to a factor of three by modifying the shape and taper of MRFM cantilever mounts [24].

Torsional oscillators represent another area of concentrated study. These suspensions minimize issues of thermoelastic damping and have achieved some of the longest ringdown times of any oscillator designs [25]. These suspensions may be used to approximate linear detector magnet motion as I describe in this thesis, or to couple a magnetic moment to a torquing detector magnet. Garrett Leskowitz also reviews this topic and its relation to nano-scale BOOMERANG designs [4].

Study of more exotic oscillator suspensions, such as air bearings or spinning magnets supported by magnetic fields [tron toy], may yield large enhancements in oscillator τ_h , but require substantial investigation and development. A final motivation for oscillator geometry design involves providing enhancements to displacement sensors, such as the use of very thin beams, or “folded” or “ribbed” beam paths to increase piezoresistive sensor response to a given amplitude [26].

2.3 Oscillator Displacement Measurement

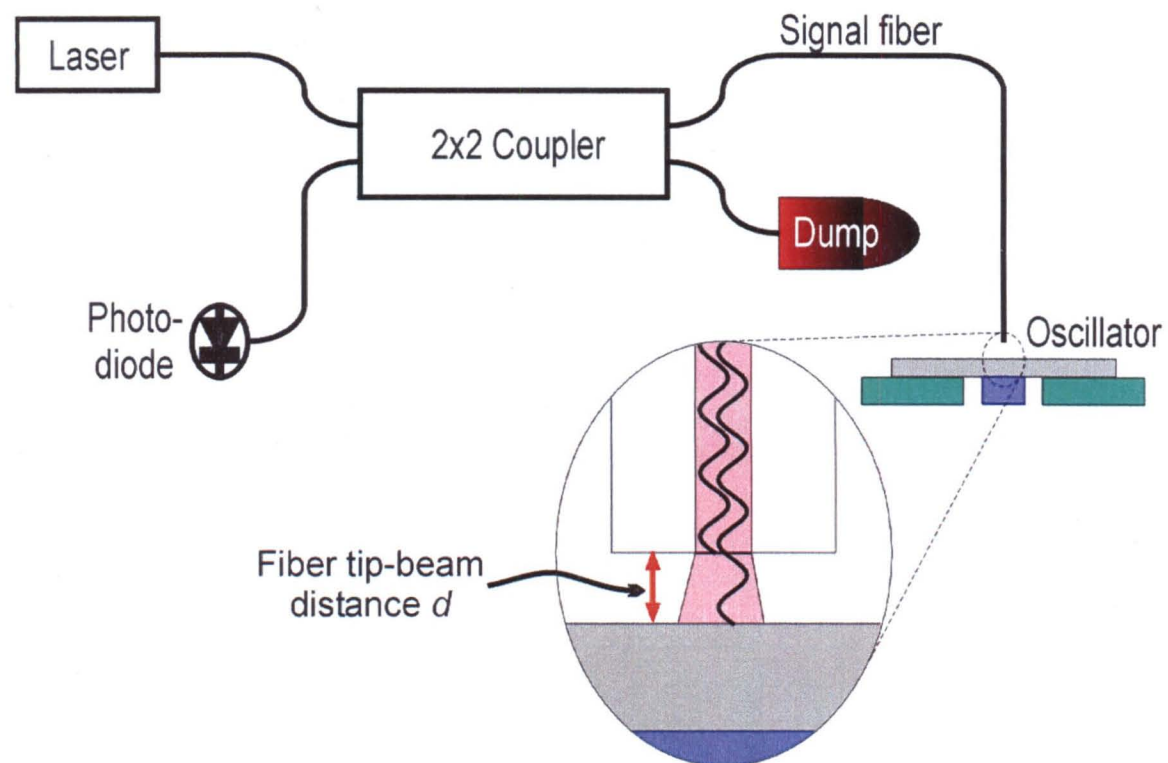
An essential element of mechanically detected NMR is making audiofrequency position measurements well enough that the noise in the experiment is dominated by the thermal motion of the mechanical oscillator. Here I describe the sensitive and convenient technique of fiber-optic interferometry (FOI), and an important innovation, transverse fiber-optic interferometry (TFOI). This method combines excellent displacement sensitivity ($\sim 1 \text{ m}\text{A}/\text{rt Hz}$) with large dynamic range and ease of manufacture. I will also

briefly summarize and compare the properties of other competitive displacement sensing methods.

2.3.A Fiber-Optic Interferometry

Fiber-optic interferometry represents a versatile and convenient method of displacement sensing on micro-scale and macro-scale objects. Rugar developed the FOI for displacement measurement in a high-sensitivity atomic force microscope [5] as a

Figure 2.3.1: Fiber Optic Interferometer. Short-coherence-length laser light travels through the fiber coupler through the signal fiber. As shown in the blow-up view, Fabry-Perot interference occurs between light reflected from the fiber face and from the mechanical oscillator surface, and depends on the fiber tip-beam distance d . The photodiode detects the back-reflected, distance-dependent interferometer fringe intensity. The beam dump, with an index-matched light sink, couples excess light out of the interferometer to prevent parasitic back reflections into the photodiode. This device affords convenient amplitude measurements down to $0.1 \text{ pm}/\sqrt{\text{Hz}}$.



replacement for the more cumbersome optical lever technology [27]. Coherent laser light travels through a 2 X 2 fiber-optic coupler and into the two fibers on the other end of the coupler, one being the sensing fiber, and one a vestigial fiber that I term the “dump.” Light reflection back into the sensing fiber occurs off of the glass-air interface due to the index of refraction difference. For 800 nm light and standard glass fibers, this wavelength-dependent reflection is 4% of the initial light intensity. The tip of the sensing fiber may be positioned relative to an object to be measured (the “measurand”) to form a Fabry-Perot interferometer cavity between the end of the fiber tip and the measurand surface. That is, light reflects off of the measurand and back into the fiber and interferes with the light back-reflected off of the glass-air interface. This interference signal travels back through the sensing fiber and through the coupler to impinge onto a photodetector, which converts the cavity-length-dependent intensity into a photocurrent. A transimpedance amplifier converts this photocurrent into a voltage for easy observation. The easily positioned and compact fiber tip in an FOI obviates the need for the delicate optics alignment and feedback quadrant photodetection present in an optical lever.

Figure 2.3.1 depicts the FOI with emphasis on the sensing tip and Fabry-Perot cavity.

The interference fringe traces out a cosine wave, usually riding on a nominally linear ramp, as the fiber tip-measurand distance d varies. Figure 2.3.2 depicts this fringe profile. Only the light field reflected back into the fiber that is mutually coherent with the light field back-reflected inside the fiber can contribute to the interference signal. The phase dependence of this interference term contributes to the level of the observed photocurrent, and depends on the measurand displacement relative to the fiber tip. As the fiber tip moves toward or away from the measurand, the fringe position changes with the

size of this term. For close distances d , more light reflects back into the fiber than is needed for the optimum interference signal, so as d increases, the dc level gets smaller and the fringe visibility gets larger. For large distances d , less light reflects back into the fiber than is needed for the optimum interference signal, so as d increases, the dc level gets larger and the fringe visibility gets smaller. The percentage of light reflected off of the glass-air interface back into the fiber may be modified by using a fiber with different

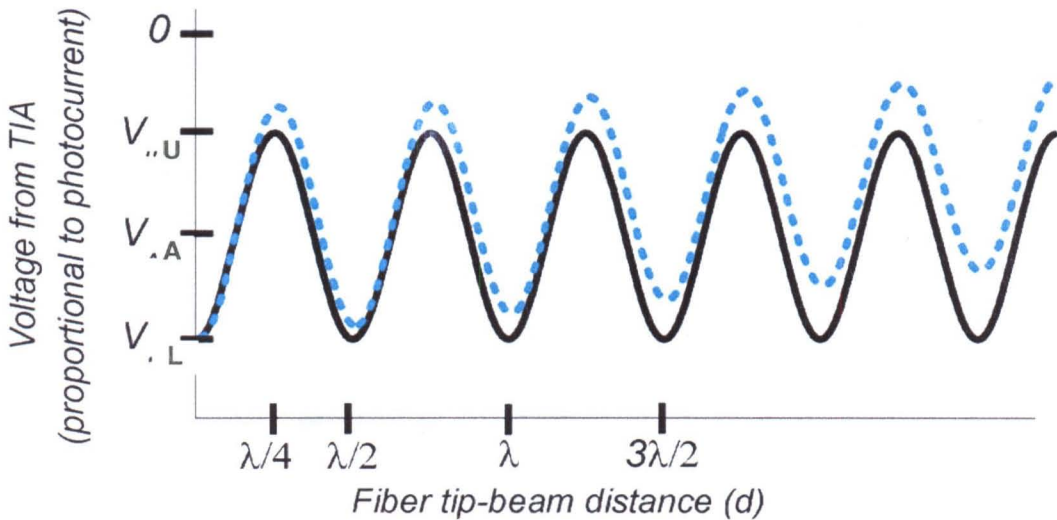


Figure 2.3.2: Interferometer Fringe vs. Fiber tip-Beam Distance.

The black curve shows the ideal interferometer voltage curve. The dotted curve shows a more typical but exaggerated profile, where both the upper and lower voltage extrema V_U and V_L and the average voltage V_A shift as the fiber-beam distance d is varied. The numerical aperture of the fiber (NA) describes light leaving a given fiber with a diverging cone angle. This causes the variable loss of light re-entering the fiber dependent on the distance d . Note that the voltage from the transimpedance amplifier (TIA) is proportional to, but inverted in sign from, the intensity of light hitting the photodiode.

refractive index, coating the fiber with a material of different refractive index (e.g., silicon) [28], or changing the wavelength of the light.

The wavelength of the laser light used limits the displacement sensing range of this device. Since the difference in intensity between the upper and lower bounds of the fringe occurs over $\lambda/4$ of the distance d , the range where the sensor is linear is

approximately $\lambda/8$, or about 100 nm for 800 nm light. This range might be extended by a suitable fiber-position feedback or modulation scheme, or by using a longer optical wavelength.

Photon counting uncertainty or “shot” noise and photon pressure uncertainty noise are intrinsic mechanisms limiting the sensitivity of the FOI when used for displacement sensing. We require that this FOI sensitivity be sufficient to observe the thermal motion noise of the mechanical oscillator. At low laser power, shot noise dominates the noise as the uncertainty in photon counts becomes a larger fraction of the signal light, and the photon pressure noise does not substantially drive the oscillator motions. At high laser power, the magnitude of photon pressure noise becomes large enough to drive the oscillator, and thus dominates the BOOMERANG detector noise due to the interferometer [29, 30]. Both sources of FOI noise are readily made much smaller than oscillator thermal motion noise for mirror-like oscillators at room temperature such that we may use a wide range of laser powers in these experiments.

Heating of the mechanical oscillator represents another significant issue when using optical interferometry. Silicon oscillators absorb light at 800 nm, which is above the Si bandgap, such that the interferometer light heats the oscillator and may cause distortions or stresses, with accompanying frequency or equilibrium position changes. This heating may be reduced or eliminated by using below-bandgap light (*e.g.*, 1300 nm or 1550 nm), or by using an oscillator material chosen to be transparent to the interferometer light. While the idea of reflection may seem counterintuitive in this case, the light will reflect at least partially off of any oscillator surface due to oscillator-air refractive index difference, just as in the fiber tip back reflection. For very thin

oscillators ($< 1 \mu\text{m}$ thick) at cryogenic temperatures, Rugar *et al.* have found it is useful to make the oscillator thickness an odd multiple of $\lambda/4$ [28]. Note that the second reflection off of the oscillator back surface acquires a π phase shift due to the negative change in refractive index.

In cases of very small BOOMERANG oscillators, the FOI spot size of $\sim 5 \mu\text{m}$ may cause unacceptably small fringe visibility and large dc offset since only a small fraction of the spot reflects back into the fiber. It may then be prudent to use lenses to focus the FOI light spot, or use a different displacement sensing technique. The new technique of force-detected optical spectroscopy (FDOS) has spurred some ideas for novel fiber-optic displacement sensor designs designed to detect nanoscale oscillators [31].

In order to assess the practicality of fiber-optic interferometers, we use the fringe visibility F [32]. We may calculate F in percent using the following formula:

$$F = \frac{V_U - V_L}{V_U + V_L} \times 100 = \frac{V_W}{2V_A} \times 100, \quad 2.3.1$$

where V_W and V_A are the width and average of the fringe, and V_U and V_L are the upper and lower bounds of the fringe in Volts. While FOI sensitivity only depends on the trade-off between shot noise and photon pressure noise and not explicitly on the fringe visibility [29, 30], we find it convenient for practical monitoring and feedback to operate BOOMERANG experiments with $F > 1\%$, and typically $F > 20\%$. For cases where heating presents a problem, *e.g.*, in low-temperature experiments or with thermally fragile oscillators, an FOI with high photon efficiency becomes important [28]. I detail

experimental details of FOI use and observations of heating in BOOMERANG instruments in section 3.1.D.

2.3 B Transverse Fiber-Optic Interferometry

While Rugar's FOI provides excellent sensing properties, in the case of micron-scale or smaller BOOMERANG instruments using permanent static-field-production magnets, the required geometry of the fiber forces compromises in the magnet assembly design. In order that the fiber tip axis is perpendicular to the surface of the oscillator beam surface, we must define holes in the field-production magnets. For the 60 μ m spectrometer, these holes would be twice the diameter of the detector magnet, thus causing severe reduction in the field strength and field homogeneity across the sample.

We have designed and demonstrated an alternative, the transverse fiber-optic interferometer (TFOI), which relaxes this geometric requirement and allows placement of the sensing fiber tip parallel to the ring magnet plane. The TFOI simply uses a sensing fiber tip polished at 45 degrees to the fiber axis to direct light, through total-internal reflection, perpendicular to the fiber axis. By rotating the fiber such that the plane of the 45 $^{\circ}$ angle polish intersects the plane of the oscillator beam in a line perpendicular to the fiber axis, the Fabry-Perot cavity then forms between the edge of the fiber and the oscillator beam surface. Figure 2.3.3 shows the TFOI tip geometry, and a representation of the BOOMERANG spectrometer using both the standard FOI arrangement and the TFOI arrangement. We detail other advantageous applications of the transverse fiber in AFM displacement sensing, optical data storage, and optical switching in a pending US patent [6].

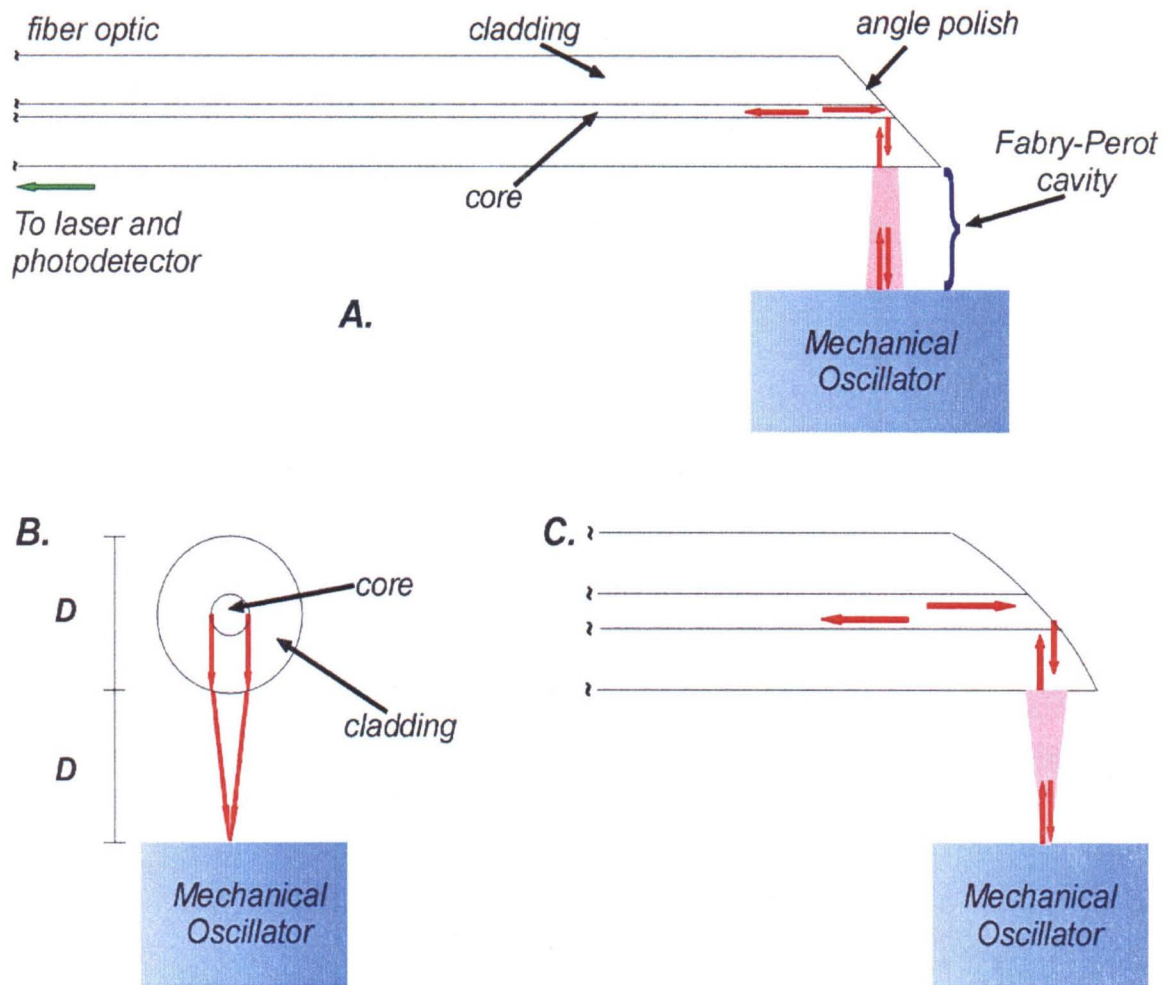


Figure 2.3.3: Transverse Fiber-Optic Interferometer: By polishing the fiber tip at 45^0 , light launches perpendicular to the fiber axis by total internal reflection. The cladding-air interface and the surface of the detector oscillator form the Fabry-Perot interferometer cavity analogous to that in a normal FOI. This cavity modulates the intensity of light reflected back to a photodetector as a function of the length of the cavity. This TFOI allows convenient displacement sensing in geometrically constrained devices, such as micro-BOOMERANG, and may simplify fiber positioning relative to AFM heads or other sensor types. Part A shows a cross-section of the TFOI. The angle-polished plane should intersect the oscillator surface plane in a line normal to the fiber axis. Part B depicts the view along the fiber axis, indicating the lensing due to the cylindrical fiber surface that focuses the light to a line parallel to the fiber axis. Part C shows the effect of curved polishing on the fiber tip, allowing light focusing to a spot.

2.3.C Other Displacement Sensing Methods

As yet, fiber-optic interferometry appears to be the most favorable displacement sensing method for BOOMERANG. However, here I include a short review of other methods that may prove useful in certain situations, given sufficient development. Tunnel sensors provide sensitivity approximately equal to the FOI, but lack linearity and dynamic range without a substantial positioning stage and feedback motion of the tunnel sensor tip [33]. The inconvenience of needing separate fibers or tips (*e.g.*, tunnel sensors) in fine alignment with BOOMERANG oscillators leads us to also consider methods that may be fabricated directly onto the BOOMERANG detector substrate in a parallel fashion. Using spatially selective metallization, doping, or oxidation commonly used in silicon microfabrication [15] (see also Chapter 4 for review of fabrication techniques), we may define piezoresistive [26, 34], or capacitive [35] position sensors directly onto wafers containing BOOMERANG detectors.

Piezoresistive sensors use the change in resistance of a material (*e.g.*, doped Silicon) under strain, where the sensing element is part of a balancing circuit, such as a Wheatstone bridge. These sensors currently lack the sensitivity needed for thermal-motion-limited detection of proposed micron-scale BOOMERANG oscillators, but their convenience and ease of parallel manufacture lend support to their further development [26, 34, 36].

Capacitive sensors are extremely easy to define onto micromachined structures, and indeed, the capacitive transducer described above (section 2.2.C) may possibly serve as a sensor as well. Capacitive sensing appears to have the necessary position sensitivity down to the scale of $\sim 10 \mu\text{m}$ [35], but this methods relies on charge bearing electrodes,

and as designs are scaled down, charge counting uncertainty may increase the sensor noise floor to an unacceptable level.

2.4 Rf Excitation and Data Collection

When designing our BOOMERANG instruments, we have employed a few main guidelines for excitation of NMR, and for acquisition of interferometer-detected oscillator motion data. When pursuing a new mode of instrumentation such as BOOMERANG, discoveries of optimal strategies usually become evident after substantial experimentation, and are not practically foreseeable. I seek to summarize our basic design principles here, and leave specific issues of experimental device discovery and optimization for Chapter 3, where I describe BOOMERANG apparatus and experiments.

2.4.A Rf Excitation System

Since the rf coil does not contribute to the detection sensitivity directly, we may design it with only spin excitation in mind. An advantage of BOOMERANG over inductive detection is that spin evolution of any number of nuclei (*e.g.*, ^1H , ^{14}N , and ^{13}C) may be encoded simultaneously into mechanical oscillator motions on each shot of an NMR experiment. We can cyclically invert each nucleus simultaneously using the rf excitation coil and it is actually preferable to have an untuned (flat response) coil probe circuit (see also section 3.1.E). As long as each nucleus experiences efficient ARP inversion (see section 3.2.A below for a complete discussion), sensitivity is maximized for all detected nuclei. This contrasts traditional detection where complicated multiple-tuned coil probes are needed to observe more than one nucleus, and some combinations

are inefficient in terms of sensitivity. Since we focus on millimeter-scale and smaller spectrometers and the excitation power scales roughly with the volume of the coil, we need not concern ourselves with amplifier power requirements becoming a limitation. Any power dissipated in the coil probe circuit or filters is likely unimportant relative to the overall usage, which would include computation, feedback, and temperature control. Keeping power deposited into the mechanical oscillator acceptably low could be an issue when exciting multiple nuclei.

Having a flexible method of generating shaped cyclic inversion sequences and multiple-pulse sequences represents another key design priority. In our opinion, using a digital-synthesis arbitrary waveform generator and, if necessary, appropriate mixers to shift carrier frequencies, is the method of choice for BOOMERANG excitation. For our prototype experiments, we have also employed an rf amplifier, but we do not foresee this as a necessity at the micron scale due to the vastly smaller rf excitation power needed. Since these waveforms must efficiently invert magnetization for as much as several seconds, it is imperative that these rf circuits have very low noise (*e.g.*, phase noise) to prevent spurious spin flips that cause dephasing relaxation.

2.4.A Data Collection System

In many ways, collection of BOOMERANG signals is much easier than inductive NMR since signals exist completely in the audiofrequency range, and thus no rf heterodyne receivers, filters, or mixers are needed to allow signal digitization. Indeed, one might use a lock-in amplifier to process oscillator response signals with the reference frequency set to the oscillator excitation frequency. However, in order to efficiently analyze mechanical spurious driving sources close to the oscillator resonance, we highly

recommend digitization of the oscillator signal after preamplification. Since the mechanical oscillations are in the audio range, we may utilize A/D boards run by desktop computers. Cheap but adequate boards exist with maximum bandwidths of up to ~ 100 kHz. For optimally digitized signals, use of bandwidth-limiting filters prevents noise from folding in from outside the Nyquist bandwidth of the digitizer. Optimal software weighting of signal transients minimizes noise within the sampled bandwidth.

The other necessity in digitizing circuitry is that the start of digitization should exactly synchronize with the onset of the rf excitation (cyclic inversion) sequence on every shot of the experiment. This allows phase measurement of the mechanical oscillation to determine whether encoded spin evolution creates positive or negative M_z before the start of driving. This shot-to-shot consistency allows encoding of the bipolar transverse-plane precession into successive shots to build up a pointwise FID or other time-domain NMR signal (see also section 1.2.D).

References

1. Leskowitz, G.M., L.A. Madsen, and D.P. Weitekamp, *Force-detected magnetic resonance without field gradients*. Solid State Nuclear Magnetic Resonance, 1998. **11**(1-2): p. 73-86.
2. George, T., et al. *MEMS-based force-detected nuclear magnetic resonance spectrometer for in situ planetary exploration*. in *2001 IEEE Aerospace conference*. 2001. Big Sky, Montana.
3. Madsen, L.A., Leskowitz, G. M., and Weitekamp, D. P., *Observation of Force-Detected Nuclear Magnetic Resonance in a Homogeneous Field*. Manuscript In Preparation, 2002.
4. Leskowitz, G.M., *Force-Detected Magnetic Resonance Independent of Field Gradients*, Chemistry Ph.D. 2002, California Institute of Technology: Pasadena, CA.
5. Rugar, D., H.J. Mamin, and P. Guethner, *Improved Fiber-Optic Interferometer For Atomic Force Microscopy*. Applied Physics Letters, 1989. **55**(25): p. 2588-2590.
6. Madsen, L.A. and D.P. Weitekamp, *Transverse Optical Fiber Devices for Optical Sensing, Switching, and Storage*, 2000, California Institute of Technology: US Patent Application.
7. Wolfram Research, *Mathematica 3.0 and 4.0*, <http://www.wolfram.com/>. 2002.
8. Ansoft Corp, *Maxwell FEM Package*, <http://www.ansoft.com/>. 1997: Pittsburgh, PA.
9. Pilkey, W.D., *Formulas for Stress, Strain, and Structural Matrices*. 1994, New Yord: John Wiley and Sons.
10. Leissa, A.W., *Vibration of Plates*. Vol. SP 160. 1969: NASA.
11. Roark, R.J. and W.C. Young, *Roark's formulas for stress and strain*. 6 ed. 1989, New York: McGraw-Hill.
12. Roukes, M.L. *Nanoelectromechanical Systems*. in *Solid-State Sensor and Actuator Workshop*. 2000. Hilton Head Island, South Carolina.

13. Streitz, F.H., K. Sieradzki, and R.C. Cammarata, *Elastic properties of thin fcc films*. Phys. Rev. B, 1990. **41**(17): p. 12285-12287.
14. Grossi, R.O., P.A.A. Laura, and Y. Narita, *A Note On Vibrating Polar Orthotropic Circular Plates Carrying Concentrated Masses*. Journal of Sound and Vibration, 1986. **106**(2): p. 181-186.
15. Madou, M.J., *Fundamentals of Microfabrication*. 1st ed. 1997, New York: CRC Press.
16. Tang, W., *Personal Communication*. 1998.
17. Yasumura, K.Y., *et al.*, *Quality factors in micron- and submicron-thick cantilevers*. Journal of Microelectromechanical Systems, 2000. **9**(1): p. 117-125.
18. *Thermophysical properties of matter*. The TPRC data series; a comprehensive compilation of data, ed. Y.S. Touloukian. Vol. 13. 1970, New York: IFI/Plenum.
19. *Properties of Silicon*. 1988, London: INSPEC.
20. Mastrangelo, C.H., *Thermophysical properties of low-residual stress, silicon-rich, LPCVD silicon nitride films*. Sens. Actuators, 1990. **A21-A23**: p. 856-860.
21. Griffiths, D.J., *Introduction to Electrodynamics*. 2nd ed. 1989, Englewood Cliffs, NJ: Prentice-Hall.
22. Baselt, D., *The tip-sample interaction in atomic-force microscopy and its implications for biological applications*, Chemistry Ph.D. 1993, California Institute of Technology: Pasadena, CA. p. 178.
23. Wang, K., A.C. Wong, and C.T.C. Nguyen, *VHF free-free beam high-Q micromechanical resonators*. Journal of Microelectromechanical Systems, 2000. **9**(3): p. 347-360.
24. Streckeisen, P., *et al.*, *Instrumental aspects of magnetic resonance force microscopy*. Applied Physics a-Materials Science & Processing, 1998. **66**: p. S341-S344.
25. Markert, J.T., K. Mochizuki, and E.E. Judge, *Direct measurement of forces on superconducting vortices using high-Q single-crystal-silicon double-torsional oscillators*. Physica B, 2000. **284**: p. 723-724.
26. Harley, J.A. and T.W. Kenny, *High-sensitivity piezoresistive cantilevers under 1000 angstrom thick*. Applied Physics Letters, 1999. **75**(2): p. 289-291.

27. Alexander, S., *et al.*, *An Atomic-Resolution Atomic-Force Microscope Implemented Using an Optical-Lever*. *Journal of Applied Physics*, 1989. **65**(1): p. 164-167.
28. Mamin, H.J. and D. Rugar, *Sub-attoneutron force detection at millikelvin temperatures*. *Appl. Phys. Lett.*, 2001. **79**(20): p. 3358-3360.
29. Rugar, D. and P. Grutter, *Mechanical Parametric Amplification and Thermomechanical Noise Squeezing*. *Physical Review Letters*, 1991. **67**(6): p. 699-702.
30. Sidles, J.A., *et al.*, *Magnetic-Resonance Force Microscopy*. *Reviews of Modern Physics*, 1995. **67**(1): p. 249-265.
31. Lambert, B.M. and D.P. Weitekamp, *Force-detected optical spectroscopy*. *Bull. Amer. Phys. Soc.*, 2000. **45**: p. 105.
32. Fowles, G.R., *Introduction to Modern Optics*. 2nd ed. 1975, New York: Dover.
33. Binnig, G., C.F. Quate, and C. Gerber, *Atomic Force Microscope*. *Physical Review Letters*, 1986. **56**(9): p. 930-933.
34. Harley, J.A. and T.W. Kenny, *I/F noise considerations for the design and process optimization of piezoresistive cantilevers*. *Journal of Microelectromechanical Systems*, 2000. **9**(2): p. 226-235.
35. Schiffer, B.R., A. Burstein, and W.J. Kaiser, *An active charge cancellation system for switched-capacitor sensor interface circuits*. *Ieee Journal of Solid-State Circuits*, 1998. **33**(12): p. 2134-2138.
36. Reynolds, J.K., *et al.*, *Packaging a piezoresistive pressure sensor to measure low absolute pressures over a wide sub-zero temperature range*. *Sensors and Actuators a-Physical*, 2000. **83**(1-3): p. 142-149.

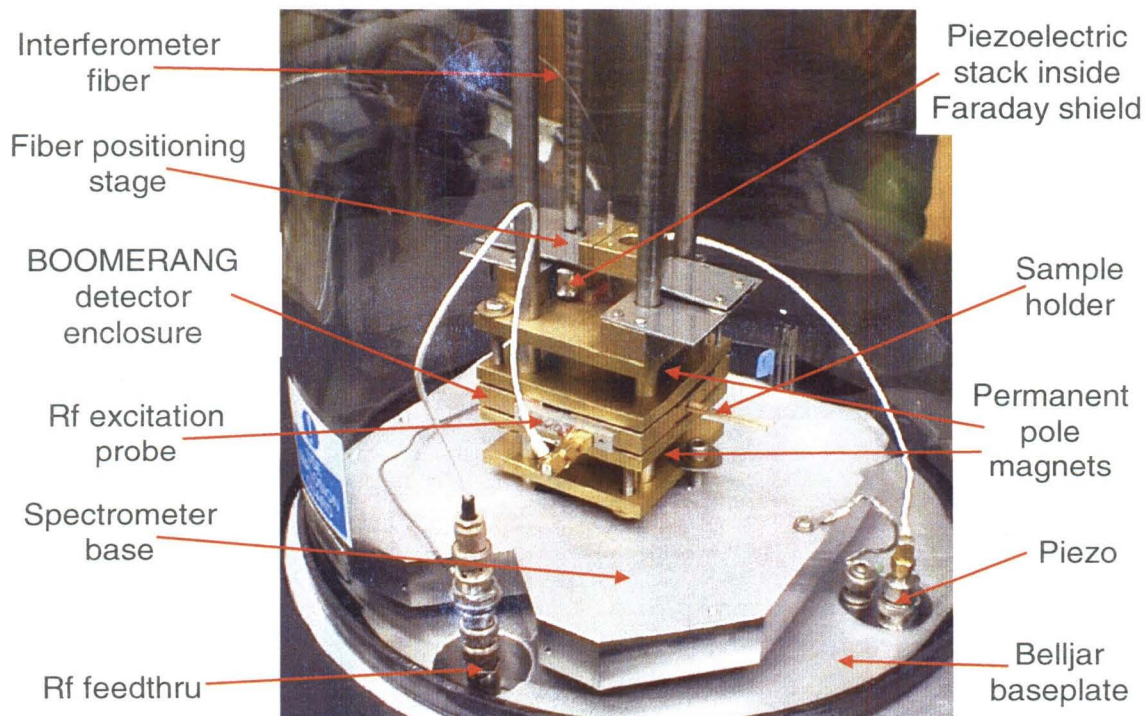
Chapter 3: The Prototype BOOMERANG Spectrometer and Experimental Observations

3.1 Spectrometer Assembly and Functionality

BOOMERANG represents a novel method of NMR detection, with its own distinct challenges and mysteries. We have chosen to pursue development of a macro-scale prototype spectrometer to show the applicability and generality of BOOMERANG,

Figure 3.1.1: BOOMERANG Prototype Spectrometer Assembly.

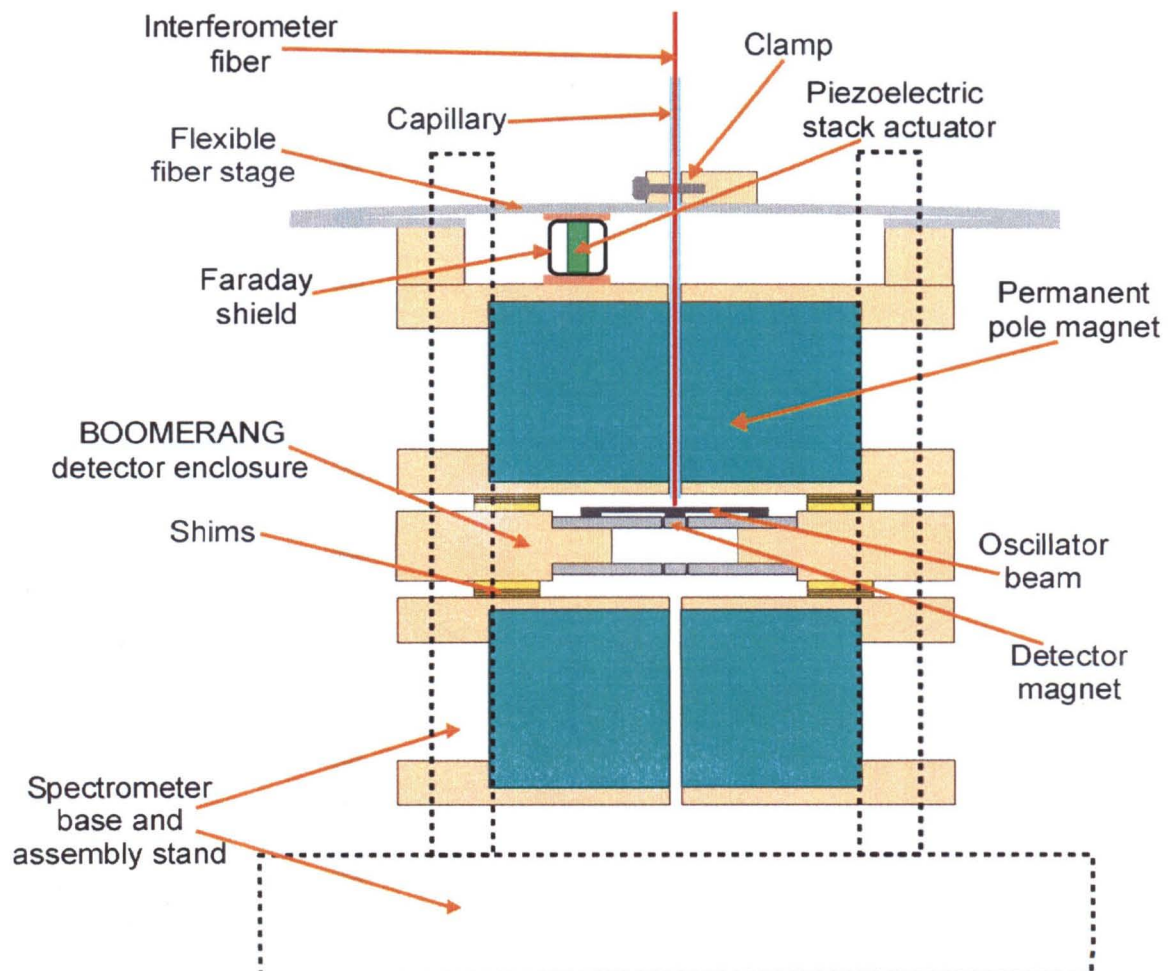
This spectrometer has provided all experimental NMR data presented in this thesis. Choice of the 3 mm detector magnet size allows fabrication by conventional machining, while providing adequate NMR sensitivity. This device shows the generality of the BOOMERANG method, quantitatively verifies our predictive theories, and aids in development of planned micron-scale spectrometers. Permanent magnets supply the 0.7 T static field and polarize the BOOMERANG magnet assembly. A belljar encloses the main spectrometer components in a < 10 mTorr vacuum to allow low-noise, low-dissipation force detection.



and to attempt to surmount experimental complexities that will be relevant to future micron-scale spectrometers.

Here I present our experimental apparatus and related discoveries, and our NMR results on 3 mm diameter samples, and leave reports of micron-scale results for Chapter

Figure 3.1.2: Cross-Section of BOOMERANG Prototype. The pole magnets, the detector and ring magnets, and the shims all have cylindrical symmetry. For simplicity, we form only one magnet-on-beam oscillator, with all other magnets remaining fixed relative to the sample. The capillary serves to fix the fiber near its tip both to remove thermal drift due to fiber length fluctuations, and to allow ease of fiber clamping. We shim the magnetic field (largely dB_z/dz and d^2B_z/dz^2) by changing the thickness of the brass shims. The piezoelectric stack allows up to 10 μm z-axis fiber positioning, and is protected from direct rf driving by the Faraday shield.



4. Figure 3.1.1 shows a photograph of the apparatus, and figure 3.1.2 shows a to-scale cross-sectional view.

3.1.A B_0 Field Permanent Magnets and Spectrometer Supports

In order to obtain sufficient static-field strength with simple design and low cost, we purchased custom neodymium iron boron magnets with the highest remanent field commercially available [1] (“NdFeB40” alloy, $B_r = 1.4$ T). A pair of brass plates fixed together with screws sandwich each of these NdFeB magnets. The cylindrical magnets are 2.54 cm thick by 5.08 cm diameter with 1.60 mm holes drilled down their axes, one magnet’s hole for fiber optic access, and the other hole to maintain symmetry. These magnets produce a B_0 field of 0.69 Tesla between them when held 1.7 cm apart with their magnetization axes aligned. We have observed field strengths of 0.59 – 0.73 T in our NMR experiments, depending on the distance between these magnets.

In order to ease manipulation of the magnets relative to each other and to hold all magnets along a common axis, we constructed a magnet stand with an aluminum base 2.5 X 40 X 40 cm with four non-magnetic stainless steel rods (304 alloy) 9.53 mm in diameter and 30 cm long mounted (press fit) normal to the plane of the base in a square 4.763 mm on a side. This aluminum base also provides a rigid, non-magnetic inertial mass to prevent ambient vibrations from coupling into the oscillator’s motion.

We have employed four 2 X 2 X 1 cm blocks of Sorbothane \circledcirc vibration isolation material [2] under the corners of this stand to yield large reductions (greater than a factor of 5) in system vibrational noise floor. We attempted to further reduce vibrations using 5 X 5 X 1 cm Sorbothane blocks under the corners of the table supporting the vacuum chamber and spectrometer, but these yielded no significant vibration damping. As

described below in section 3.2.C, we have achieved near-thermal-motion-limited detection with the remainder of the noise due to the interferometer, indicating that our vibration isolation attempts have been successful.

The brass mounting plates for the magnets have 9.55 mm holes drilled in them to match the four stainless rods on the base. Without lubrication, the sandwiched field magnets easily slide over the rods and lower into position using hand-operated aluminum levers to counteract the large attractive magnetic forces. A similar brass plate is used to mount the BOOMERANG detector assembly and locate it between the field magnets.

3.1.B Detector Oscillator and Ring Magnet Assembly

The detector-oscillator assembly represents the most critical part affecting the performance of our prototype spectrometer, and the most demanding to manufacture. We incorporate a single-crystal silicon oscillator suspension and a HyMu80 [3] (4% Mo, 80%

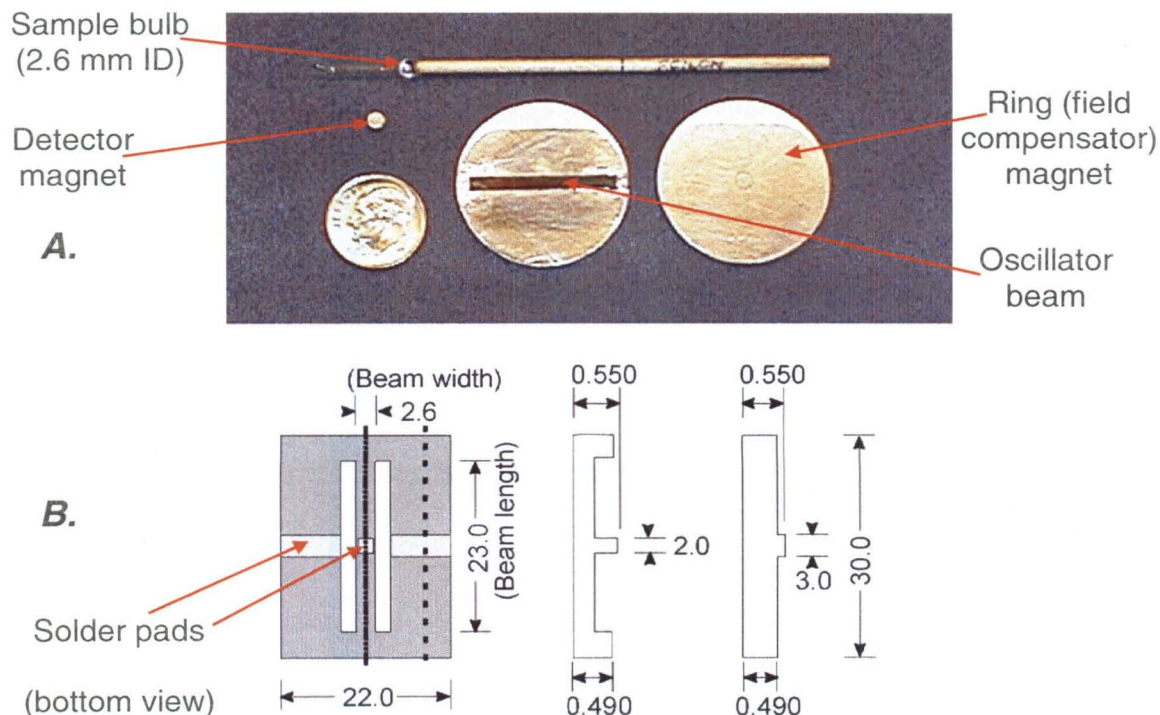
	Length	Width	Height	ID	OD
Oscillator beam	23.0	2.7	0.22		
Detector magnet			1.5		3.0
Ring magnet			3.0	3.05	30.5
Field magnets			25.4	1.6	50.8
Rf excitation coil	0.9			4.1	4.4

Table 3.1.1: Prototype BOOMERANG Spectrometer Dimensions.
This table gives measurements for the main elements of the prototype. The distance from the sample center to the closest point on the detector magnet is 2.4 mm. All dimensions are in mm.

Ni, 16% Fe, $M_s = 1.0$ T) magnet assembly with a gap of 1/40 the detector magnet radius (40 μm) between the detector and ring magnets. Table 3.1.1 shows the dimensions of the prototype BOOMERANG magnet assembly and oscillator suspension.

The oscillator suspension consists of silicon beams etched to give raised solder pads, and coated with 1000 \AA of evaporated gold to aid adhesion. Due to the difference in thermal expansion coefficients between the HyMu80 ($\alpha = 12.3 * 10^{-6} /{}^\circ\text{C}$) and silicon [4] ($\alpha = 2.6 * 10^{-6} /{}^\circ\text{C}$), we connect the magnets to the suspension using a low-temperature solder (44% In, 42% Sn, 14% Cd eutectic, $\text{MP} = 93^\circ\text{C}$) [5] using a hotplate.

Figure 3.1.3: Detector Oscillator and Sample. Part A shows both top and bottom views of the composite oscillator assembly, along with a separate detector magnet and a sample held in a spherical glass bulb. Part B is a schematic of the modified silicon beam used to counteract creep and anchor losses. The two cross-sections on the right correspond to the lines through the plan view shown at left, in respective order from left to right.



Early testing using carbon steel magnets ($M_s = 2.0$ T) showed problems with fast corrosion during soldering, prompting the switch to the well-characterized, stainless, and inexpensive HyMu80 material. However, preliminary testing with coated steel magnets with non-corrosive materials, and soldering of steel magnets under a dry nitrogen atmosphere, indicated the possibility of using steel or other corrosion-prone materials if necessary.

We assemble BOOMERANG oscillators using the following procedure, which involves placing a thin shim between the detector and ring magnets, soldering them together, and then removing the shim to free the oscillator. First, we place the lathed detector and ring magnets together onto a glass plate and super glue them together. Using successively finer grades of sandpaper (400 down to 2000 grit) on top of the glass plate, we polish both sides of the detector/ring assembly to attain a smooth and planar surface for both magnets. After separating the magnets by soaking in acetone, we place them on a clean glass microscope slide and insert a piece of 13 mm-thick mylar shim stock into the gap between them. This shim should be 2 mm X 9 mm so as to fit completely inside the detector/ring gap around the circumference of the detector magnet. After placing the slide and magnets onto a 130 - 150°C hotplate, we apply small drops of liquid, organic-salt flux [5] (Indalloy flux #4) to each solder point on the magnets, followed by 1 mm lengths of 1 mm-diameter solder wire. We retouch the solder points with flux to strip any remaining oxide, and then place the oscillator beam pads onto the solder points and align the beam relative to the magnets. After removal from the hotplate and while the assembly cools, we apply pressure to the top of the beam only above the solder pads. After cooling, we retrieve the shim by pushing a small corner of 25 μ m steel

shim into the detector ring gap to force part of the mylar shim out to allow us to grab onto it and pull it out. If we observe no resonance from a given oscillator, then we may push pieces of shim stock through the detector/ring gap to remove impurities, which will often allow the oscillator to freely resonate.

During oscillator testing and NMR experiments, I noticed an apparent creep in the suspension solder joints, manifested as changes in oscillator frequency and ringdown time over long periods (weeks to months). This indicates an inelasticity in the suspension mounts and prompted us to redesign the oscillator such that the beam was part of a thicker “brick” of silicon that we solder to the ring magnet far away from the ends of the beam. Figure 3.1.3 shows this modified beam design, along with the original beam and magnets. To incorporate the capacitive feedback transducer described in section 2.2.C, we also photolithographically patterned this beam and evaporated gold onto it to form the middle plate of the transducer. After switching to this novel beam configuration, we have not observed irreversible oscillator frequency changes due to creep. Figure 3.1.3 part A shows a photograph of an assembled detector-oscillator, along with a separate detector magnet and a sample, while part B depicts the modified beam design.

3.1.C B_0 Field Shimming

We have used combinations of annular brass shims in several thicknesses from 0.025 mm to 3.25 mm thick to precisely separate the three magnet mounts from each other. Typical shim stacks are between 1.5 mm and 3.5 mm thick, with 2.5 mm the optimal thickness for field homogeneity, assuming perfectly centered detector magnets. We have investigated using standard electromagnetic coil shims, which would allow finer control, but have yet to incorporate them.

Two adjustable factors influence the magnetic field homogeneity across the sample in this spectrometer - the detector magnet equilibrium position and the distances between each static field magnet and the center of the sample. An interdependence of these factors exists in that the detector magnet position changes due to the change in static gradient when the static field magnets are shifted. Additionally, the detector magnet equilibrium position relative to its centered (coplanar with ring magnet) position depends on the exact construction of the oscillator suspension. Assuming the oscillator suspension locates the detector magnet in its exact center position, shim stacks should place the static field magnets at their optimum position for homogeneity.

The most reliable method of shim adjustment involves careful assembly, followed by feedback from NMR signals, just as in conventional spectrometers. In the first step, we assess the practicality of the mechanical oscillator by determining visually if the detector magnet is centered in (*i.e.*, coplanar with) the ring magnet after assembly of the spectrometer magnets. By adding or subtracting shim thickness symmetrically above and below the detector array, the detector magnet is pulled further up or down, respectively. The best oscillators have the detector magnet centered when the shim thickness is near its optimum for field homogeneity, but in any case, adding or subtracting shims allows centering of the detector magnet. The effects on field homogeneity from an uncentered detector magnet far outweigh the effects from non-optimal static-field-magnet placement. In some cases, an oscillator may have too much built-in detector magnet offset, and must be rebuilt or adjusted.

Once the detector magnet is centered to the limit of visual inspection, we acquire a simple FTNMR spectrum, as described in sections 1.2.D and 3.2.G, to determine the

field-homogeneity-limited linewidth. I then “shim on the spectrum” by adding or subtracting shims to attain the best NMR linewidth. Using this method, I have achieved linewidths as small as 6 kHz, or 200 ppm for protons in a 0.7 T field. Our theoretical FEM calculations indicate that far better homogeneity is possible using the same device geometry, up to a factor of 10^3 , given more accurate manufacture. Also, simple calculations suggest that using coil shims would allow for ~ 1 ppm homogeneity with much more convenient tuning.

3.1.D Fiber-Optic Interferometer and Fiber Position Feedback

I have described our general interferometer apparatus in section 2.3.A, and I depict the layout of our specific interferometer in figure 3.1.9 below. We drive a short-coherence-length 780 nm Sharp LT023 diode laser [6] to < 10 mW optical power using a homebuilt current source, as depicted in Appendix A.1. A 50/50 fiber coupler from Seastar Optics, made from 125 μm -cladding, 5 μm -core fiber, carries this light to a signal arm and a “dump” arm. Light reflects from the Fabry-Perot cavity formed at the end of the signal arm back through the coupler and into a photodiode, which is reverse biased with a 9 V battery. A Princeton Research 181 transimpedance amplifier (TIA) provides an amplified voltage from the $\sim 1 \mu\text{A}$ oscillator-modulated photocurrent. The fiber coupler arms are FC/PC connectorized to allow convenient configuration changes, or fiber tip, photodiode, or laser replacements.

To obtain maximum fringe visibility and minimum DC offset of the fringe, we clean the fiber connector faces periodically using lens paper and acetone or methanol, and we incorporate an index-matched beam dump. For best performance, we begin by checking the fringe dc offset with the laser on by pulling the fiber tip/capillary away from

any reflecting surface by at least 2 mm. This dc offset should be < 5 V with the TIA sensitivity on 10^{-7} A/V. The beam dump contains some black foam soaked with diffusion pump oil to disperse the light. The foam acts to absorb this light so that it does not reflect back into the interferometer, and the oil acts as a refractive index matching fluid to better couple light into the foam. These measures decrease reflections from the fiber connector faces and from the end of the unused fiber on the 2 X 2 coupler, which can dramatically increase the dc light level hitting the photodetector.

We incorporate two simple structural methods into our FOI mounting apparatus to minimize spurious vibrational noise, and to minimize fringe drift due to thermal expansion. First, we fix the signal fiber close to its tip (within 1 mm), to minimize the effect of any thermal changes to the fiber length on the length of the fiber tip-beam cavity that forms the Fabry-Perot interferometer. We accomplish this by inserting the fiber through a *ca.* 1.5 mm-OD, 0.6 mm ID glass capillary, and gluing the fiber in place near the tip using Crystal Bond thermoset glue. Second, we rigidly fix all pieces of the spectrometer, especially the fiber positioning stage and the oscillator mounts to one another with minimal distance between the fiber mounts and the oscillator mounts. This second measure decreases coupling of undesirable ambient vibrations into the interferometer cavity length.

We may also adjust the laser level to tailor the average fringe position, or the fringe width to the particular parameters of an experiment. Often after pumping down and/or long periods of rf heating, the fiber or oscillator drifts substantially such as to saturate the TIA, or decrease the fringe visibility. Dialing the laser current up or down may bring the interferometer fringe into an acceptable range for doing experiments. In

order to balance shot noise with photon-pressure noise it is in principle best to keep the laser power in an optimum range. In the prototype spectrometer, we have used laser currents of 60 - 90 mA without substantial increase in the noise floor of the interferometer. The large mass of the millimeter-scale mechanical oscillator decreases the importance of photon pressure noise and heating (high laser powers). Micron-scale designs will require more careful optimization of laser power, as described in section 2.3.A.

As shown above in figure 3.1.1, we incorporate a 304-stainless-steel fiber positioning stage into the brass mount that houses the top field magnet. This stage is stiff but flexible along the fiber and oscillator motion (z axis), but extremely rigid in the transverse directions. Using finger control alone, we slide the capillary holding the fiber through the upper static-field magnet until the tip comes close to the oscillator beam and we observe satisfactory interferometer fringes. We then fix the capillary in place using the brass-block and set-screw clamp. By applying some drag friction using the partially-engaged clamp, we may position the fiber to a useable position using only finger adjustments. The piezoelectric stack actuator (Thorlabs model AE0203D08) [7] allows up to 9 μm of fine fiber position control at a maximum of 150 V.

Application of rf irradiation to the spins and thus the surrounding spectrometer assembly causes fringe drifts of up to $\sim 1 \mu\text{m}$ in several minutes. We observe several thermal time constants, presumably arising from thermal equilibration of the oscillator beam, the central BOOMERANG detector support, and the static field magnet assembly and supports. To provide stability of the fringe at its most sensitive average position during NMR experiments of more than a few minutes, I have incorporated active

proportional feedback on the fiber position via a homebuilt op-amp circuit. This circuit allows application of -18 V to $+40$ V to the fiber stage piezo actuator, which gives a feedback range of about $3 \mu\text{m}$. I describe and depict this circuit in Appendix A.2. We have also begun work on a temperature feedback system for the magnet assembly to increase stability of the NMR experiments.

Due to unlocking of the fringe feedback circuit during high power rf pulses, I found it necessary to enclose the piezo actuator in a flexible brass Faraday shield, which I found was most effective when the shield was isolated from the magnet assembly and connected to the rf ground. This allows stable operation using rf pulses of up to 140 kHz Rabi frequency.

Finally, I mention initial measurements of the performance of the transverse fiber-optic interferometer (see section 2.3.B). We obtained 45^0 -angle-polished fibers along with a 90/10 fiber coupler [8]. By constructing a simple testing jig, we were able to observe fringe visibility of $> 50\%$. The rotation angle about the fiber axis exhibited a tolerance of approximately $+/- 3^0$, while still allowing observable interferometry. These measurements have confirmed that TFOI is a robust and generally applicable method of displacement sensing.

3.1.E Rf Excitation System and Coil

The Signatec Arbitrary Waveform Generator (AWG-502) is a programmable 12-bit digital-to-analog (D/A) converter board that we use for generating arbitrary NMR pulse sequences. It occupies an ISA expansion slot in the PC used to run the experiment. A C++-language, DOS executed program on the PC loads the AWG board with waveforms and timing sequences for the experiments. I direct the reader to the thesis of

Garett M. Leskowitz for detailed descriptions of these experiment operation programs [9]. Analog channel 1 of the AWG outputs analog rf waveforms of up to 5MHz when using a 10MHz clock. Channel 2 generates a sine wave at the mechanical oscillator driving frequency v_d , at or near v_h , and is sent directly to a second digitization channel for timing calibration, which is necessary for phase-sensitive measurements.

We use a homebuilt single-sideband mixer to create pulses at the NMR frequencies of interest by mixing the AWG output with another fixed rf source (see Appendix A.3 for circuit diagram). The mixer takes waveforms from AWG channel 1 as the “IF” input and an adjustable-frequency sine wave from a PTS 500 frequency synthesizer as the “LO” input, and outputs the difference frequencies between the IF and LO inputs at its “RF” port. We may also easily configure this mixer to synthesize sum frequencies instead.

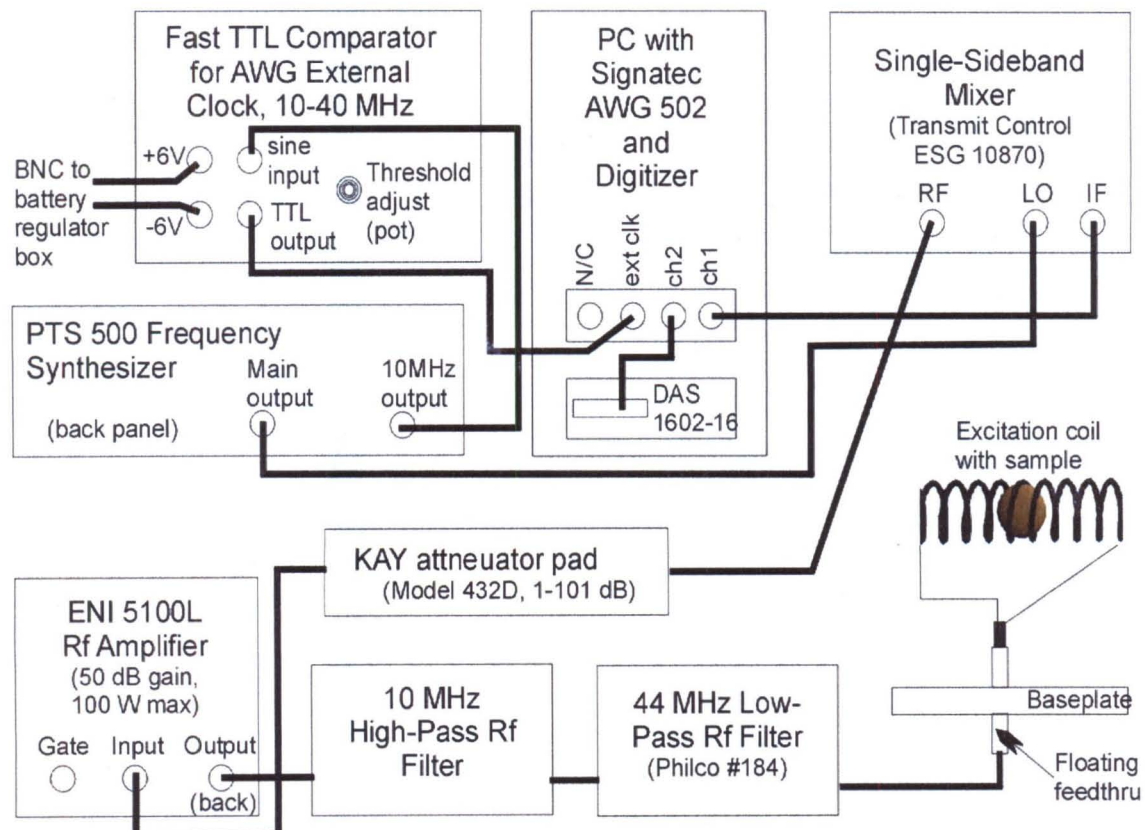
During optical NMR (ONMR) experiments in our group, which also use the Signatec AWG-502 synthesizer, James G. Kempf observed an increase in the rotating frame (spin-locked) relaxation time T_{1p} of a factor of 4 after switching from the AWG’s on-board clock to a cleaner external clock [10]. Following the success in the ONMR experiment, we constructed a clock circuit to drive the external clock input on the AWG and allow for low-phase-noise waveform generation (see Appendix A for diagram). We use a fixed, 10MHz sine output from the same PTS 500 used for mixing to provide the stable clock source signal for the AWG. The PTS 500 bipolar sine wave triggers a fast TTL comparator circuit (bandwidth up to 40 MHz) to generate TTL square waves (0 V to +5 V nominal) at the same frequency. If we desire a different frequency of TTL signal, we may use the variable output from a second PTS to generate the sine wave input. As in

the ONMR experiments, we observed a factor of 4 increase in spin-driving (cyclic inversion) relaxation time T_{1a} , as compared to experiments using the AWG internal clock.

We use an ENI 5100L rf amplifier to provide 50 dB of amplification (100 W max) to NMR pulse sequences, which drive the rf excitation coil surrounding the sample. We have tried several different amplifiers with varying results. While using an older ENI A-500 amplifier, we observed shorter cyclic-inversion relaxation times T_{1a} by up to a

Figure 3.1.4: Rf Excitation System Schematic and Coil Probe.

The PTS supplies the AWG with a low-phase-noise clock signal via the TTL circuit. The rf waveform from the AWG is mixed up to the desired NMR frequencies with the adjustable (ca. 30 MHz) PTS output by the single-sideband mixer. The level of the mixer's "RF" output is adjusted by the KAY attenuator pad, then amplified by the ENI rf amplifier. Finally, the rf is conditioned by the high-power filters before passing through the vacuum baseplate and reaching the coil. Note that the coil is isolated from the baseplate/spectrometer grounds, thus aiding stability of the interferometer fringe feedback circuit.



factor of four. This deficit most likely stems from excessive phase noise in these amplifiers. See section 3.2.C below for a discussion of ARP cyclic inversion and T_{1a} .

Rf filters limit the bandwidth of NMR pulses to remove rf signals outside the frequency range of our experiments, which may cause unnecessary heating of the coil or the mechanical oscillator. Several configurations provided adequate results, but we found the best arrangement was simply to use high-power rf filters, a 10 MHz high-pass (homebuilt) and a 44 MHz low-pass (Philco #184), between the rf amplifier and the coil to generate a flat frequency response around the excitation frequencies of interest.

Tuning and matching of the coil was not necessary since the available rf power never limited our excitation level, and since we do not use the coil as a detector. Flat frequency response in our circuit allows the ARP frequency sweeps at $2v_h$ to remain flat in amplitude over each sweep, thus minimizing direct rf driving of the mechanical oscillator. Indeed, due to our implementation of π phase shifts on alternating ARP cycles, Fourier components of the rf exist at v_h , which may spuriously drive the oscillator if substantial rf-circuit amplitude-response variation is present. Figure 3.1.4 shows a schematic of the rf system and indicates the path the rf travels from the waveform generator to the rf coil.

While less critical than in inductive NMR applications, the coil and probe head still constitute an important component of the rf excitation system in the BOOMERANG spectrometer. A solenoidal coil must be made from wire that is thin in the radial direction to minimize the space it occupies between the sample and the detector magnet. To this end, we use 30 gauge copper magnet wire, flattened to 0.12 mm X 0.48 mm cross-section, to wind our 9-turn coils over a glass or beryllia tube. Alternatively, a coil

without turns directly wound around the sample, *e.g.*, a Helmholtz pair, gives somewhat worse excitation efficiency and B_1 homogeneity, but allows the sample to be placed closer to the detector magnet, thus improving sensitivity.

Since we must apply continuous rf to the spins for up to several seconds, rf heating presents a challenge for coil/lead survival and for detector oscillator frequency stability. Any heat deposited into the detector oscillator tends to change stresses in the suspension, and thus the oscillator frequency. To minimize this effect, we implemented

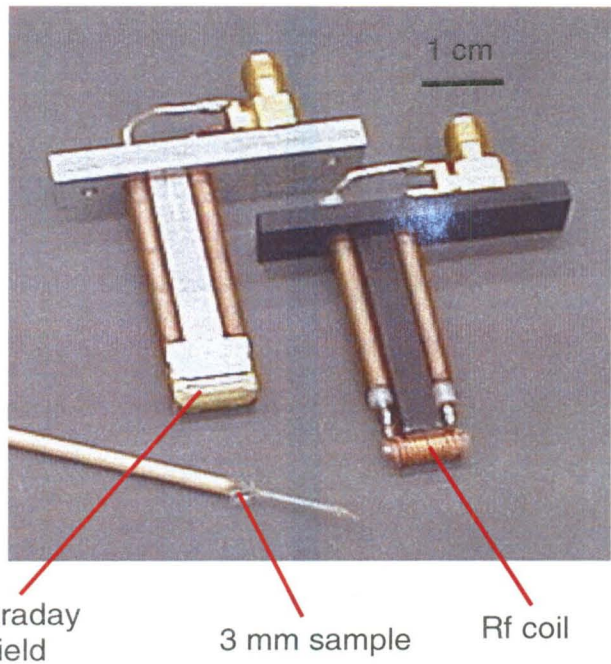


Figure 3.1.5: Rf Coil Probe. We replaced the black plastic probe on the right with the improved aluminum probe on the left, which uses a beryllia (Be_2O_3) coil form and brass Faraday shield. Both probes incorporate 9-turn solenoidal coils wound from flattened 30 gauge copper wire. The 4 mm-OD sample bulb slides inside the rf coil.

two strategies – mounting of the coil onto a support with high thermal conductivity, and enclosure of the coil in a Faraday shield to block rf electric fields from exciting currents in the magnet assembly. We obtained cylindrical tubes made of beryllia (Be_2O_3), wound coils around these, and then mounted this assembly to an aluminum probe head. Beryllia, even in ceramic form, has thermal conductivity (250 W/m-K) [11] a factor of 6 higher than sapphire (40 W/m-K) [12] and a factor of 200 higher than fused silica (1.4 W/m-K)

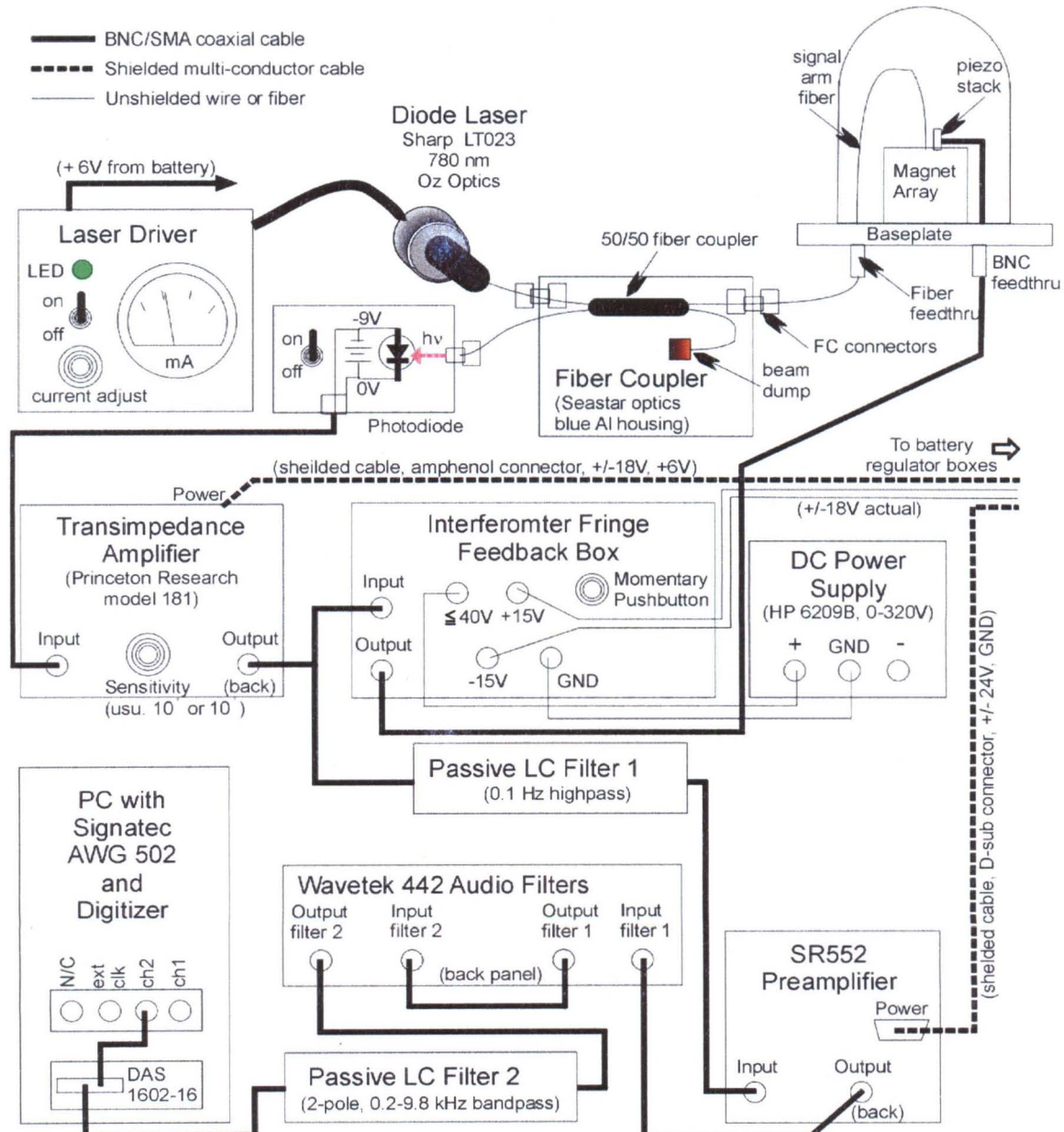
[12]. This first attempt at thermal sinking did not observably affect oscillator drift due to rf heating. We then enclosed the coil, except for the ends, in a 25 μm -thick brass shield grounded to the magnet assembly. This shield reduced the drift of the oscillator frequency during NMR experiments by more than a factor of three, and allowed experiments of more than $\frac{1}{2}$ hour in length without human monitoring. Figure 3.1.5 shows a picture of an early unshielded probe design made with glass and plastic support, accompanied by the shielded probe head with aluminum and beryllia support.

3.1.F Data Collection System

Here I describe the processing and digitization of the signal emerging from the fiber-optic interferometer. As mentioned in section 2.4.A, we must obtain accurate synchronization of the digitization with the beginning of the rf cyclic inversion sequence.

A Princeton Research model 181 transimpedance amplifier (TIA) converts the photodiode current to a voltage, and has an adjustable gain of 10^4 to 10^9 V/A. We typically use the 10^6 or 10^7 V/A ranges to amplify the $\sim 1 \mu\text{A}$ photocurrents, a large fraction of which come from the fringe dc offset and average fringe position, and not from the ac oscillator signals. We then strip the dc level off of this voltage using a passive high-pass LC filter with 0.1 Hz cutoff frequency v_{cutoff} , and amplify this voltage using a Stanford Research SR552 preamplifier. Two Wavetek 442 audio filters, a low-pass set to $v_{cutoff} \sim 100$ Hz in series with a high-pass set to $v_{cutoff} \sim 2 v_h$, serve to bandwidth-limit the amplified ac signal to exclude noise outside the Nyquist bandwidth of the digitization. A passive LC 2-pole filter with a 0.2-9.8 kHz bandpass further shapes the signal before digitization using the Computer Boards DAS 1602-16 expansion board. Figure 3.1.6 depicts this data acquisition network.

Figure 3.1.6: Oscillator Detection Path Schematic. The optical signal from the FOI impinges on the reverse-biased photodiode. The transimpedance amplifier (TIA) converts the resulting photocurrent to a voltage. The fringe feedback circuit reads this voltage and feeds back on the piezo stack to maintain the dc fiber tip position relative to the oscillator beam. The TIA output is also filtered to remove the large dc level, amplified by the SR552 preamp, then further filtered by the Wavetek adjustable filters and LC filter 2. Finally, channel 1 of the DAS 1602-16 digitizing board records the signal.



This digitizer has a 100 kHz maximum bandwidth, and 16-bit dynamic range. We

adjust the on-board input gain to the bipolar 1.25 V range for our experiments. Unfortunately, this board does not possess a true hardware trigger, which would allow synchronization of the rf driving with digitization, using a simple TTL pulse from the AWG board to start digitization. This board’s “hardware trigger” instead incorporates a software loop that prevents triggering of the digitization more accurately than $\frac{1}{4}$ of one data sampling point. This annoyance prompted us to digitize two channels, the first being the processed signals from the interferometer, and the second being a sine wave at the oscillator driving frequency generated from channel 2 of the AWG in synchrony with the rf driving sequence. We then use this digitized sine wave to shift the origin of data collection for each shot of the experiments so that all data sets have the same phase relationship relative to the rf driving sequence. For more detail on this synchronization scheme, the reader should consult the Ph.D. thesis of Garrett M. Leskowitz [9].

To reduce background noise from purely electrical 60 Hz multiples created by switching power supplies, we use automotive batteries to power the interferometer laser, the SR552 preamp, and the TIA. We wire two 6 V and four 12 V batteries in series to yield voltages of \pm 6.3 V, \pm 18.9 V, and \pm 31.5 V (nominal), and these voltages outputs have 3 A fuses to protect circuitry. The \pm 6.3 V outputs also power the AWG external clock circuit described in section 3.1.E above. The TIA uses \pm 24 V for power, and I incorporated adjustable voltage regulator circuits to reduce and regulate the \pm 31.5 V battery outputs to \pm 24 V. Most importantly, the + 6 V battery powers the interferometer laser via a simple, filtered, constant-current source (see Appendix A.1 for circuit diagram). Switching from the Melles-Griot DLD 105 or DLD 103 laser drivers we had been using to this simple source reduced background noise peaks at multiples of

60 Hz by up to a factor of 10^3 . These background peaks, especially those at 320, 360, 420, 480, and 540 Hz were a constant irritation during NMR experiments prior to this improvement, since the oscillator frequency might fall on one of these peaks as a result of fabrication variations, or rf-heating-induced drift.

3.1.G Vacuum System

For BOOMERANG experiments described here, a Welch vane-type roughing pump brings the pressure low enough (1 to 10 mTorr) to negate oscillator dissipation due to sound transmission and viscous damping. We enclose the apparatus in a belljar, a 12" diameter glass cylindrical shell with a hemispherical top and a viton gasket to seal it to a planar aluminum baseplate. A diffusion pump allowed a further reduction of the pressure to the 10^{-5} to 10^{-6} Torr range, but no observable change in mechanical dissipation or vibrational noise level was encountered below 10^{-3} Torr. However, reducing the pressure to $< 10^{-5}$ Torr does provide reduction in arcing observed at the ~ 1 mTorr pressures and at high rf power. As mentioned in section 1.2.F, a sub-1 mTorr vacuum may be necessary to completely remove viscous damping for micron-scale oscillators [13]. Most of the reduction in oscillator damping for our oscillators occurs between about 500 mTorr and 30 mTorr. See Appendix A.5 for a more complete description and a depiction of the vacuum system.

3.2 Experimental Methods and Observations on 3 mm Samples

Many aspects of these first BOOMERANG experiments lie outside the scope of traditional NMR spectroscopy, or even previous force-detected NMR methods, *e.g.*, magnetic damping. Here I present our experimental methods and reasoning in the order

that we proceed after assembling the spectrometer. Along the way, I include development and testing that served to confirm our theories, to aid understanding of new phenomena, and to improve sensitivity. Our general protocol for conducting a multiple-pulse NMR experiment (*e.g.*, J spectroscopy) is as follows: 1) Measure the mechanical oscillator resonance, 2) Find the NMR resonance line using continuous-wave BOOMERANG spectroscopy, 3) Measure the rf field strength using nutation, 4) Measure the T_1 of the sample nuclei using inversion-recovery, 5) Acquire a FTNMR spectrum to finely determine the Larmor frequency, and 6) Conduct the desired NMR experiment.

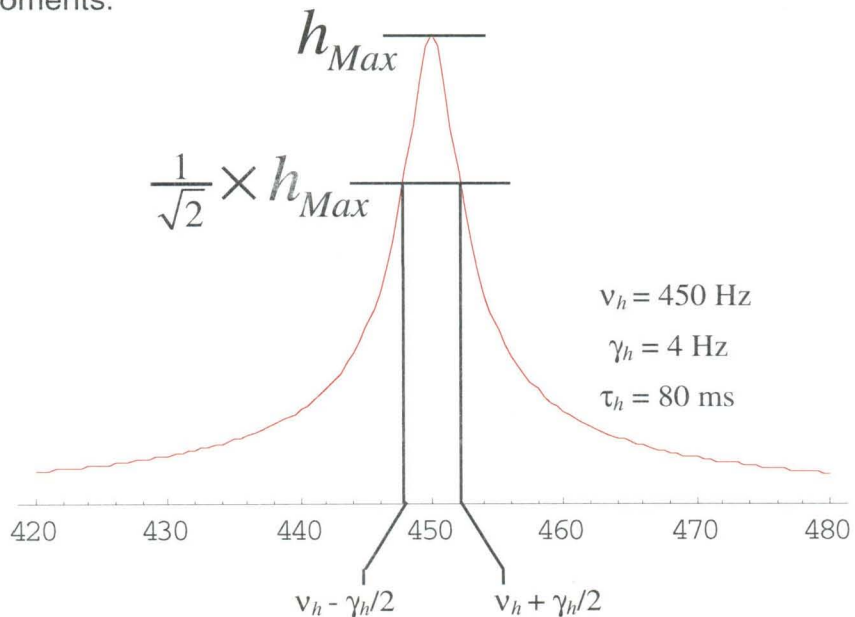
3.2.A Measuring Oscillator Resonances

Since γ_h is typically defined as the FWHM of the *energy* spectrum resonance, and we observe an oscillation *amplitude* spectrum using our interferometer, we measure γ_h as the full-width at root-half max of the amplitude spectrum in order to simply compute $Q_h = v_h / \gamma_h$ (dimensionless) and $\tau_h = 1 / \pi * \gamma_h$ (in seconds). Since energy goes as the square of amplitude, the amplitude decays at half the rate of the energy decay, thus making the amplitude resonance curve half as wide. Along with the motional mass m of the oscillator, v_h and τ_h completely define the oscillator properties affecting sensitivity, barring nonlinearities.

We begin our measurements by setting the interferometer fringe to its most-sensitive (steepest slope) average position, or the “center” of the fringe. We measure the fringe characteristics, as described in section 2.3.A, and adjust the fiber positioning stage via the voltage on the piezoelectric actuator to attain the average level. We apply a controllable excitation using the NMR coil or a z-axis test coil near the oscillator, driven by a function generator (HP 651B or Heath SG-1271) with a ~ 20 ohm current-limiting resistor in series. We measure excitation frequency with a frequency counter, *e.g.*, HP

Figure 3.2.1: Harmonic Oscillator Amplitude Response Curve.

By tracing out the oscillator response and measuring the frequencies at $1/\sqrt{2}$ of the maximum amplitude h_{Max} , we may extract the ringdown time τ_h of the oscillator. Assuming thermal-motion-limited detection, τ_h and the mass and the dipole moment of the detector oscillator completely determine its sensitivity to magnetic moments.



5216A. Scanning excitation frequency with a sine wave from the function generator reveals a resonance with $Q_h > 20$ in air, assuming the oscillator is free to move. Many other resonances will appear at much lower amplitudes due to modes of the spectrometer support structure and components. It should be easy to drive the actual oscillator

resonance such that its amplitude is comparable to or exceeds the fringe width. Applying ~ 1 mA through our NMR coil as the driving element yields an easily observable response at ν_h .

We trace out the resonance in the frequency domain, allowing measurement of the ν_h and τ_h of the oscillator as shown in figure 3.2.1. We begin by fine-tuning the excitation frequency such that the oscillator response is at a maximum, *i.e.*, at ν_h , the top of the resonance peak. After measuring ν_h to 1 Hz precision or better, and measuring the oscillation amplitude in volts, we multiply the peak oscillation amplitude by $1/\sqrt{2}$ and adjust the excitation frequency in turn to the two frequencies that give oscillator response at this amplitude. The difference between these two frequencies is γ_h . We have built mm-scale oscillators in the 200 Hz – 3 kHz frequency range, with the most useful examples for NMR exhibiting ν_h between 300 Hz and 700 Hz.

Alternatively, we have used low-frequency square waves (about a factor of 100 lower than the oscillator frequency) from a function generator (*e.g.*, Heath SG-1271) to achieve broadband excitation of the oscillator. These square transitions in field applied to the oscillator cause free ringing of the oscillator, analogous to striking a bell with a hammer, or applying a short rf pulse to a spin system. We may then extract ν_h and τ_h from the transient exponential ringdown of the oscillator after each square transition.

It is not uncommon to observe some nonlinearity in the oscillator response, especially at high excitation power. One sign of nonlinearity is that the resonance curve has different peak amplitude and width when you scan up or scan down in excitation frequency. Also, you will see asymmetry in the slope of the resonance curve on either

side of the peak. The reader should consult Baierlein [14] or Goldstein [15] for examples and discussions of anharmonic oscillators.

3.2.B Mechanical Oscillator Dissipation Studies

Using the above methods to measure oscillator dissipation, I conducted several experimental studies to determine the sources and approximate magnitudes of the damping in our BOOMERANG oscillators. The primary conclusion of these studies is that eddy-current damping currently limits our sensitivity, but we have developed strategies to counter it.

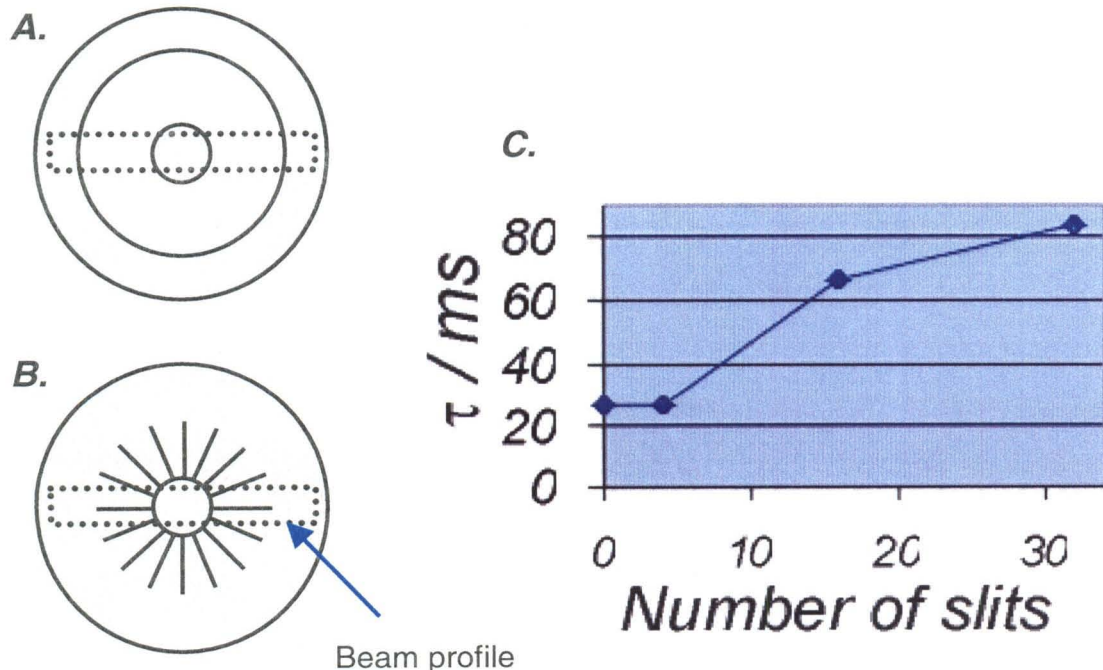
Our first goal was to determine whether losses through the beam anchors dominate damping in the absence of atmospheric damping or magnetic damping. Constructing oscillators with rigid brass clamps holding the beam ends to the ring magnet showed no improvements in ringdown time relative to soldered oscillators. However, oscillators built using ring magnets with large inner diameters, as depicted in Figure 3.2.2A, exhibited dramatically higher ringdown times in air ($\tau_h = 80$ ms) and in vacuum ($\tau_h = 300$ ms), compared to those with a narrow detector/ring gap ($\tau_h \sim 30$ ms in vacuum). While these wide-gap oscillators would not be suitable for BOOMERANG detection, the result established that magnetic damping accounts for the dominant losses in our mechanical oscillators.

Subsequently, we investigated a new type of oscillator with radial slits in the ring and/or detector magnet. As yet, we have not tested slotted-detector oscillators, but we have observed a quantitative dependence of τ_h on the number of slits in the ring magnet. We had 100 μm -wide, radial slits cut in four separate HyMu80 ring magnets using a diamond wire saw [16]. The ring magnets had 4, 8, 16, or 32 slits in them as shown in

figure 3.2.2.B, and for the 16- and 32-slit oscillators, we observed increases in ringdown times of more than a factor of two, as shown in figure 3.2.2.C. This indicates that eddy-currents dominate our damping, and rules out the possibility of substantial hysteresis damping, which is proportional to magnet volume, since the volume of ring magnets removed in the annular region near the detector magnet is only $\sim 10\%$. In these slotted magnets, homogeneity is slightly compromised due to the removal of magnetic material near the sample. We may nearly compensate for this loss by cutting slits in the magnets, coating the slits with a thin insulator, then refilling the slits with magnetic material,

Figure 3.2.2: Oscillator Dissipation Tests with Modified Ring Magnets.

The ring magnet depicted in part A (top plan view) exhibits ringdown times of 300 ms in vacuum, indicating that magnetic effects dominate damping in our BOOMERANG oscillators. Part B shows an example of a ring magnet with 16 radial slits, designed to reduce eddy-current damping in the mechanical oscillator. The plot in part C confirms that these slits reduce dissipation (ringdown time τ_h) by more than a factor of 2 with 16 or more slits. These ring magnets have vacuum gaps near the detector magnet with smaller arc lengths than the height of the cylindrical magnets.



We also conducted testing on oscillators using ring magnets made of four electrically isolated layers in the axial direction. This method showed no reduction in damping relative to monolithic oscillator magnets, but combinations of layers and slits may provide a desirable method of eddy-current reduction.

Based on our calculated predictions [9] of the eddy-current damping in cylindrically symmetric oscillators, we expect that both the detector and ring magnets contribute approximately equally to the eddy-current loss. Thus, we expect at least as large a gain in ringdown time by implementing slits or other insulating gaps in both the detector and ring magnets. I direct the reader to the Ph.D. thesis of Garett M. Leskowitz [9] for an account of our progress on quantitative eddy-current predictions in BOOMERANG oscillators. Beveling or shaping the edges of the magnets, using magnets with inherently low electrical conductivity, or sectioning the magnets into small, electrically-isolated pieces, provide other possibilities for eddy-current reduction. Since eddy-current loss is proportional to the effective resistance of the magnets, we seek to increase the effective resistance of the magnets in the regions of current flow.

3.2.C Thermal-Noise-Limited Detection

In all our NMR experiments, we seek to attain the thermal (Brownian) motion noise limit for optimal detection sensitivity. Upon measuring the mechanical frequency spectrum in the absence of any driving, we discovered that substantial background noise peaks exist in nominally dc circuits at many multiples of 60 Hz, assumedly due to square-wave transitions inherent in switching power supplies and other modern electronic circuits. After minimizing 60 Hz-multiple noise peaks by eliminating the ac-supply power sources causing them, and replacing them with batteries as described in section

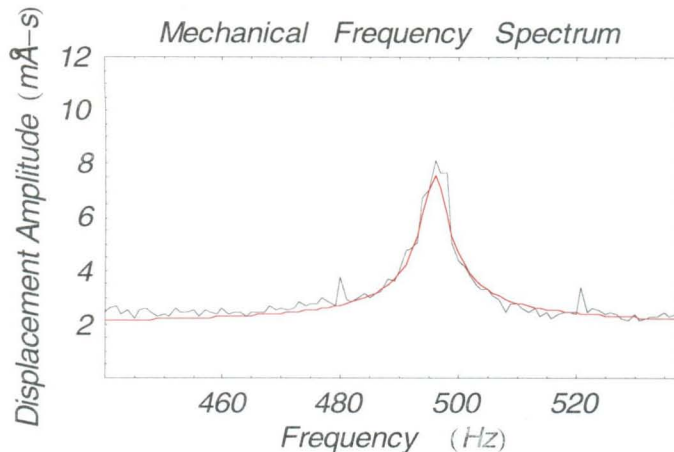


Figure 3.2.3: Thermal Motion Noise Peak.
 Acquisition of 100 mechanical transients in the absence of any driving, followed by taking the absolute values of the Fourier transform of each transient and adding them, yields this mechanical frequency spectrum. The observed peak at v_h is very nearly at the predicted thermal motion amplitude of $5 \text{ mÅ} / \sqrt{\text{Hz}}$, but is riding on a white background noise of $2 \text{ mÅ} / \sqrt{\text{Hz}}$.

3.1.F, we were able to observe thermal motion noise directly over a large mechanical frequency range. A small residual white noise component ($\sim 2 \text{ mÅ} / \sqrt{\text{Hz}}$) remains in our spectra, due most likely to intensity noise in the FOI. For smaller oscillators, this excess noise will be even less significant fractionally, so the Brownian limit will be more closely approached. Figure 3.2.3 shows the mechanical frequency spectrum of an oscillator with $v_h = 496 \text{ Hz}$.

3.2.D Efficient Cyclic Inversion: Adiabatic Rapid Passage and Variants

We have used adiabatic rapid passage (ARP) as an efficient way of cyclically inverting the z-magnetization of the sample and resonantly driving the mechanical oscillator. ARP involves sweeping an rf field through resonance in a time short compared to the spin-lattice relaxation time [17, 18]. This is achieved by smoothly varying either the rf (B_1) excitation frequency, or the B_0 field. The rate of reorientation of the magnetization must be slow compared to the Rabi frequency describing the strength of the B_1 field. In this adiabatic regime, nearly lossless inversion of the nuclear spin

population, or equivalently, the magnetization of the spin system results [18]. In force-detected magnetic resonance techniques, maximum signal occurs when the field is swept back and forth such that magnetization inversion occurs at twice the resonance frequency of the mechanical oscillator ω_h and it is repeated long enough to build up a steady-state amplitude of vibration in the oscillator [19-21]. In order to invert the magnetization over the whole sample and yet prevent cancellation of forces associated with sample volume elements at different fields, the stricter lower bound on ARP is that the sweep must be accomplished in a time short compared to $\frac{1}{4}$ of an oscillator period [19]. The adiabatic condition sets the upper bound on the sweep rate. The necessary ARP conditions in FDMR for a spectrum of width Δ are

$$4\Delta \frac{\omega_h}{2\pi} \ll \left| \frac{d\omega_0}{dt} \right| \ll \omega_i^2 \quad 3.2.1$$

where ω_h and ω_i are the oscillator's resonance frequency and the Rabi frequency,

respectively, and $\left| \frac{d\omega_0}{dt} \right|$ characterizes the B_0 field sweep rate.

In previous FDMR designs, in which the sample experiences a field gradient G during ARP, the sensitivity was compromised by the need to keep Δ small enough to allow repeated ARP. In this case, Δ is the product of the gradient strength and the sample extent or approximately GR_s in a well-designed apparatus. An alternative to sacrificing sensitivity in such a design would be to use very high (> 100 kHz) Rabi frequencies in order to adiabatically sweep through a greater fraction of the inhomogeneously broadened resonance line. This creates technical problems, such as sample heating. In the present method Δ due to inhomogeneity is lower by $> 10^3$ and depends ideally only on the intrinsic spectral width. This makes ARP effective at modest

rf power. In addition, the mechanical force per spin can be made close to optimum, given a target sample volume.

The signal on each shot is proportional to the actual spin-inversion decay time T'_{1a} of the envelope of longitudinal magnetization during ARP driving. Force-detected magnetic resonance, including BOOMERANG, requires spin population inversion efficiency better than $(1 - T/2T_{1a})$ per pass in order to prolong the signal magnetization on a given shot for a time approaching the full spin-inversion relaxation time T_{1a} allowed by irreversible processes intrinsic to the spin system, where T is the oscillator period. If the spin inversion is perfect, then a fraction $[1 - \exp(-T/2T_{1a})]$ of the magnetization is lost during $T/2$. If through non-adiabaticity or rf noise, a fraction $\epsilon = [1 - \exp(-T/2T'_{1a})]$ of the magnetization is lost in one pass through inefficient inversion, then the observed spin-driving relaxation time T'_{1a} decreases by half. For $T_{1a} = 1$ sec and $T = 2$ ms, $\epsilon < 0.001$ is necessary (99.9% efficient inversion) to suffer at best a $(1 - 1/e) = 63\%$ loss in signal to noise.

We employ tangent frequency-modulated ARP, which exhibits much better tolerance for B_0 offset frequency and B_1 inhomogeneity than compensated sequences of hard pulses, and allows far better inversion efficiency for a given rf power level than either compensated hard pulses, or sinusoidal or linear frequency sweeps [22-24]. The addition of amplitude modulation to these sequences may also provide enhancements in inversion efficiency [23, 25], at the possible cost of increased background rf driving of the oscillator.

We have also introduced a π rf phase shift on alternate ARP sweeps to further prolong signal magnetization during cyclic inversion [21]. This novel phase cycling

increases T_{1d} by up to a factor of four relative to non-phase-cycled experiments. The idea motivating this phase cycling is that on each ARP sweep without phase cycling, a small fraction of the magnetization,

$$\Delta M = \frac{2\omega_l}{\sqrt{\left(\frac{SW}{2}\right)^2 + \omega_l^2}} \sin\left(\tan^{-1}\left(\frac{2\omega_l}{SW}\right)\right), \quad 3.2.2$$

is lost when the rf is turned off and returned to its initial frequency for the next sweep,

where SW is the rf sweep width. In the limit that $SW \gg \omega_l$, we have simply

$\Delta M \cong 8\omega_l^2/SW^2$. Using our typical parameters of $\omega_l \sim 10$ kHz and $SW = 2$ MHz, this tiny effect only produces an 18% loss in magnetization over 1000 ARP sweeps, and cannot account for the difference we see between ARP with and without the phase cycling. Since we see major gains only at low rf inversion power, we attribute this difference to non-adiabaticity at the extremities of sweeps being refocused by the phase cycle. Figure 3.2.4 shows our rf modulation scheme including phase-cycling.

While the upper bound on T_{1a} is in general difficult to evaluate, it should fall between the spin-locked relaxation time T_{1p} and the spin-lattice relaxation time T_1 . For a typical liquid, where these times are equal, we expect that $T_{1a} = T_1$. To date, we have achieved T_{1d} values consistently greater than $T_1/2$ in our solid and liquid samples. As described above we have taken pains to apply “clean” rf to the spins by using an rf amplifier (ENI 5100L) and a frequency source for waveform generation (PTS 500) with low phase noise.

Signal power also depends on the rapidity of complete spin inversion. If one can invert the entire spin population in a time much shorter than one quarter of an oscillator period, then the applied force on the oscillator approximates a square wave. This has

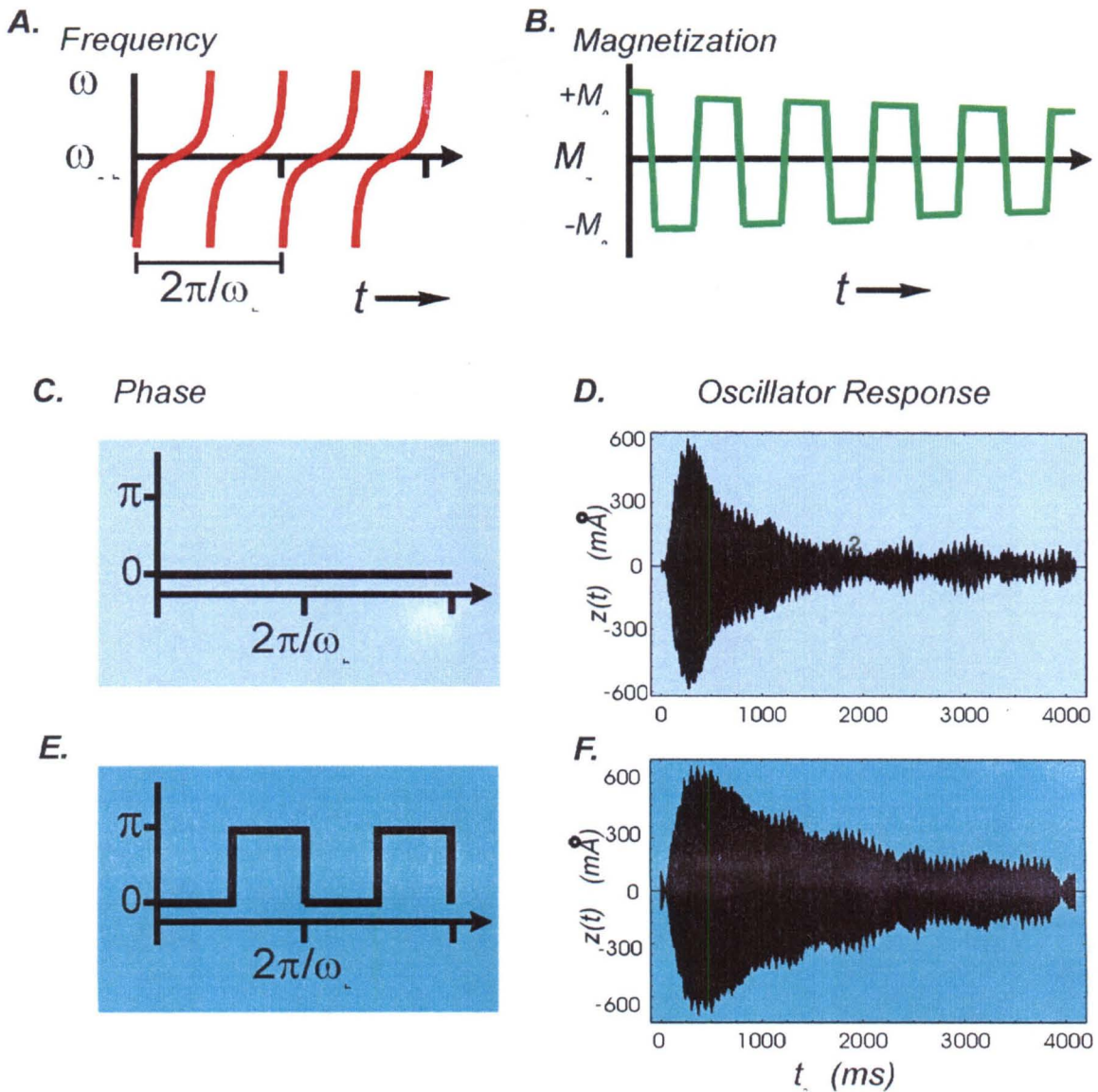
1.27 times the Fourier amplitude at v_h than the sinusoidal modulation assumed in our SNR analysis of section 1.2.E. Minimizing rf heating may, however, require that rf power be less than that required for fast (square-wave) spin inversion.

In a sufficiently homogeneous field, the spectral width may be narrow enough so that the entire magnetization can be controlled by “hard” pulses, adequately described as unitary rotations. This opens up the possibility of replacing ARP by a train of π pulses (or composite π pulses) with repetition rate $2v_h$. This is desirable in samples with a short rotating-frame spin-lattice relaxation rate T_{1p} , since these would suffer rapid magnetization decay during ARP.

Instead of using ARP and pointwise detection, we might also use BOOMERANG to do real-time detection of NMR transients. This would increase information throughput and time resolution with some cost in sensitivity. In such a method, one would apply multiple-pulse NMR sequences that change the effective quantization axis to one which has a component orthogonal to the z-axis, *e.g.*, the WAHUHA sequence [26], which shifts the quantization axis to the magic angle. Thus, we may create a component of magnetization oscillating along the z-axis, which could be used to resonantly drive the oscillator.

A third observation method would involve using pulse sequences that evolve spins and then flip magnetization onto the z-axis during windows of that pulse sequence. By timing these windows such that an M_z , which depends on the effective Hamiltonian of the evolving spin system, has a Fourier component at the oscillator frequency v_h , we may achieve resonant driving of the oscillator and encoding of a spectrum via frequency or amplitude modulation of this M_z . These last two detection pulse sequences would be

Figure 3.2.4: Phase-Cycled Tangent ARP for Broadband and Efficient Spin Inversion. Part A shows the frequency modulation used to cyclically invert spin magnetization, shown in part B, and drive the mechanical oscillations (see also fig. 1.2.2). Simple frequency modulation using constant phase on successive ARP sweeps, shown in parts C and D, gives sufficient performance for our experiments. However, use of the phase-cycled ARP version shown in parts E and F allows reduction of rf power needed for spin inversion, thus providing for more stable experiments with less heat deposited into the detector assembly. At low rf powers, we have observed improvements in T_{1a} as high as a factor of 4 using phase cycling.



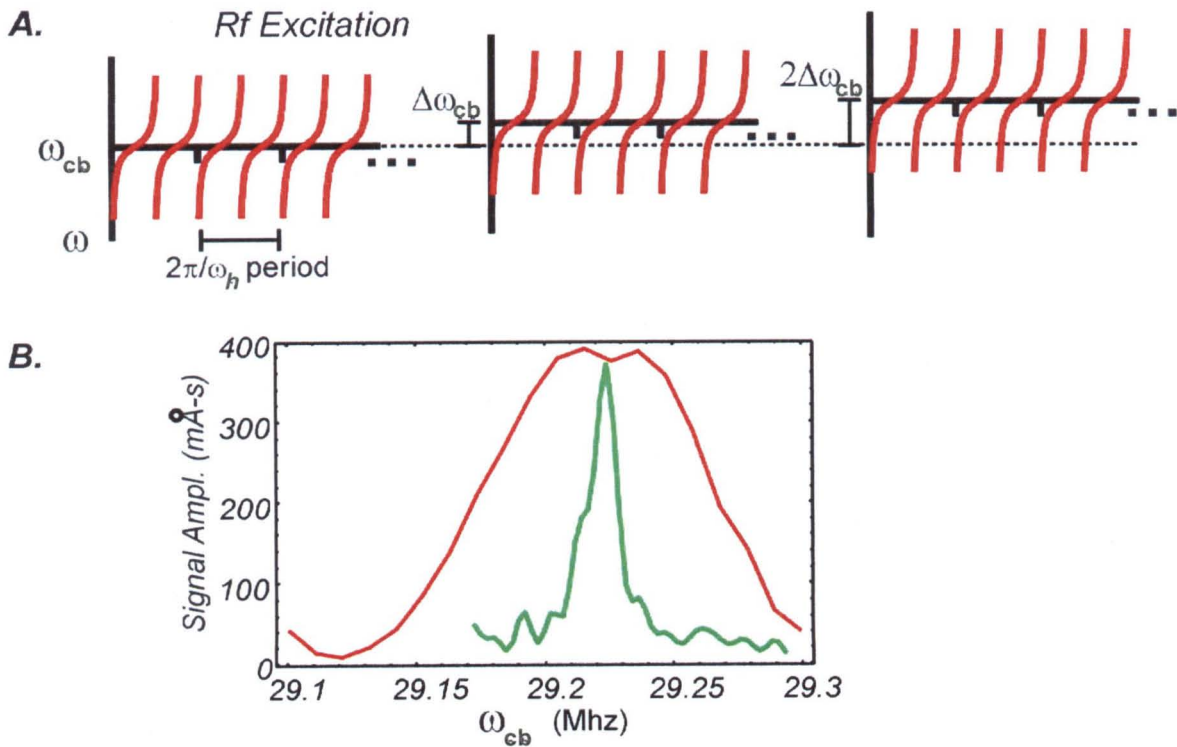
even more impractical than ARP to implement using high-gradient detection schemes since in those cases the spread of Larmor frequencies across the sample will generally

extend well beyond ω_l and conventional hard pulses could not be used directly to drive magnetization inversion.

3.2.E Continuous-Wave (CW) NMR Experiments

As our first test of BOOMERANG detection, we chose to fix the sweep-width

Figure 3.2.5: Continuous-Wave (CW) NMR Spectroscopy. Part A shows the rf frequency sweeps applied to sample. In order to trace out a resonance line, we step the centerband frequency ω_{cb} by a fixed increment $\Delta\omega_{cb}$ on successive shots of the experiment. Since the ARP sequence inverts magnetization effectively even when ω_{cb} is slightly away from the resonance line, the CW spectrum shown in B is power broadened. The inset curve in the spectrum shown in B indicates the true linewidth of the sample in the magnetic field, as obtained by pulsed FTNMR.



parameters for ARP and sweep the centerband frequency ω_{cb} over a large frequency range to find the Larmor frequency of the spins in the sample. This provides an efficient method of finding the Larmor frequency in a given magnetic field when we do not have

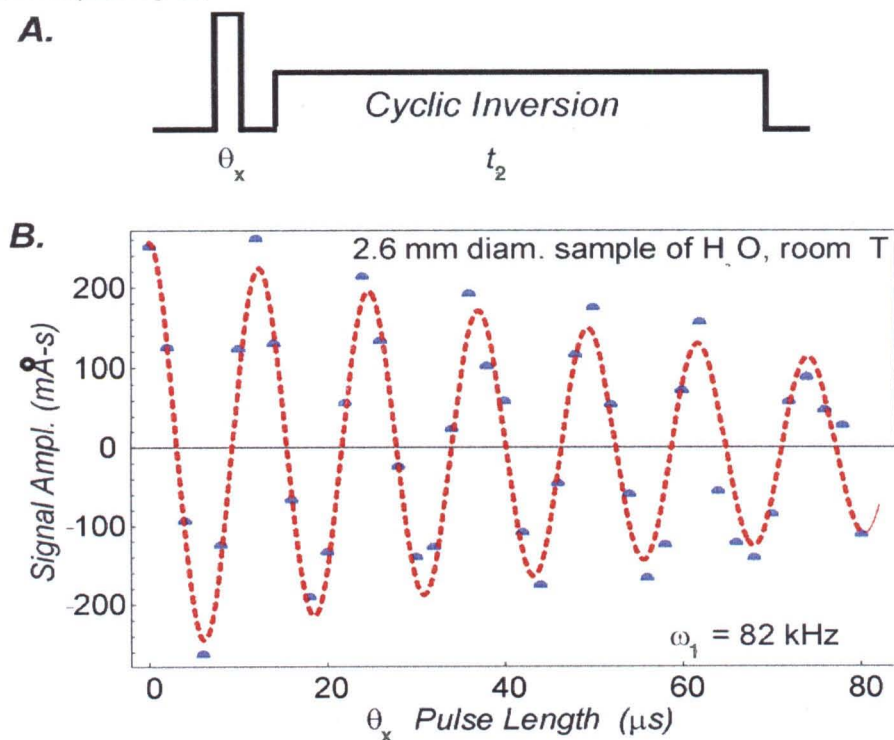
an accurate way to measure the field strength at the sample. Only spins falling within the frequency band that the ARP successfully cyclically inverts will give a signal in this method, thus we can trace out the resonance line. When we observe a flat top on the resonance curve for several points, we know that we are successfully inverting the entire sample magnetization for the time T_{1a} . We use the term CW spectroscopy because of its analogy to the first method of inductive NMR detection where a continuously swept rf field in the transverse plane allows tracing out of the spin resonances in the frequency domain [17, 27].

This type of spectroscopy exhibits power broadening, where the resonance line appears broader due to the bandwidth of efficient excitation being broader than the resonance line. As you increase the excitation power, the excitation bandwidth grows, which similarly affects the apparent spectral linewidth. This is convenient for initially locating the resonance, since a coarse search grid of frequencies suffices. Figure 3.2.5 depicts a typical CW spectroscopy signal, in which each point in the frequency spectrum represents a Fourier-transformed and weighted mechanical signal. The inset FTNMR spectrum shows the actual spectral linewidth, due mainly to the residual magnetic field inhomogeneity.

3.2.F Nutation to Determine Rf Field Strength

Once we have located the resonance line, we then measure the rf field strength B_1 that we apply using our rf excitation system and coil. This field strength is characterized by a nutation (Rabi) frequency ω_1 , *i.e.*, the frequency that the spins nutate about the excitation coil axis at the resonance condition. Figure 3.2.6 depicts the nutation rf timing sequence and the resulting time-domain signal for the protons in water at 27.2 MHz. Using the apparatus described above, we have obtained Rabi frequencies up to 140 kHz

Figure 3.2.6: Nutation to Measure Rf Field Strength. Part A shows the rf pulse sequence applied to the spins. We increment the length of the fixed-power θ_x pulse and measure the surviving M_z after the pulse using the ARP cyclic inversion sequence to drive the mechanical oscillator. After Fourier transformation and weighting, each mechanical transient (measurement of M_z) becomes one point in the nutation time-domain signal shown in part B. The points are real data and the dotted curve is a fit from which we extract the 82 kHz Rabi frequency ω_1 .

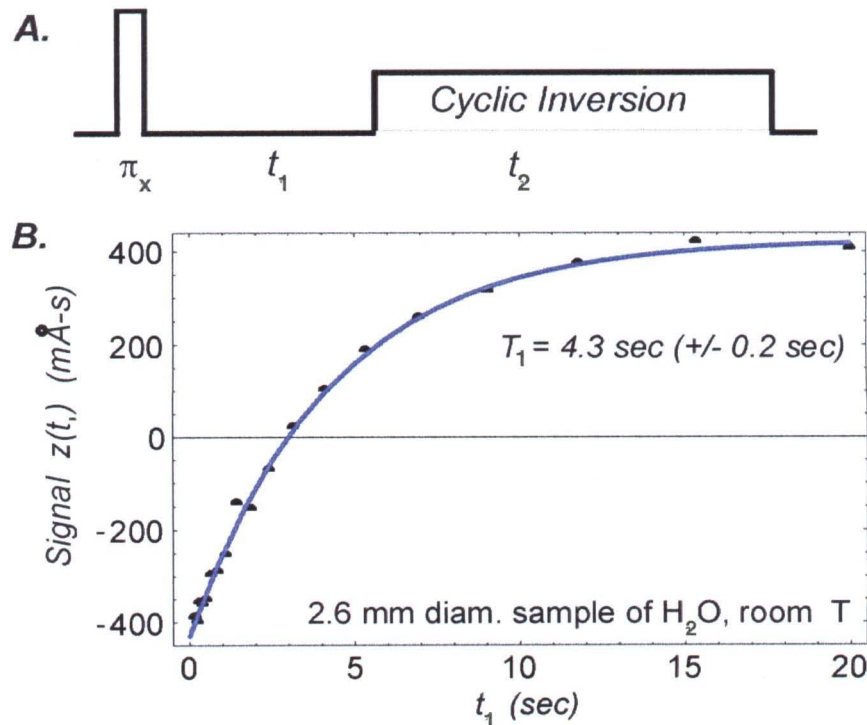


without damage to the sample, the detector, or the rf probe. The demonstrated ability to nutate over several cycles with little loss in magnetization indicates that both B_0 and B_1 homogeneity are adequate for most multiple-pulse NMR experiments. The entire sample is under coherent control, a key advantage of BOOMERANG over gradient-based force-detection methods.

3.2.G Inversion-Recovery Determination of T_1

In order to measure spin-lattice relaxation times to tailor the detection time and relaxation delay in our NMR experiments, we perform an inversion-recovery experiment

Figure 3.2.7: Inversion-Recovery Determination of T_1 . Part A shows the rf pulse sequence applied to the spins. We increment the delay time t_1 after the π_x pulse and measure the surviving M_z for each shot using the ARP cyclic inversion sequence to drive the mechanical oscillator. After Fourier transformation and weighting, each mechanical transient (measurement of M_z) becomes one point in the exponentially decaying time-domain signal shown in part B. The points are data and the solid curve is a fit to an exponential, from which we extract the spin-lattice relaxation time $T_1 = 4.3$ sec (± 0.2 sec).



in a slightly modified form. We simply apply a single inversion pulse to flip the spins to the $-z$ axis, wait a delay time t_1 , which is varied on successive shots, and then measure the M_z remaining after the delay by cyclically inverting the spins to drive the mechanical oscillator. Figure 3.2.7 shows the NMR timing sequence, and resulting data acquired at 27.2 MHz on protons in a 2.6 mm sphere of water at room temperature. The fit of the data points to a single exponential gives $T_1 = 4.3$ sec (± 0.2 sec). We have also measured T_1 for ^1H and ^{19}F in several other solid and liquid compounds, including the protons in $\text{NH}_4\text{NO}_3(s)$, where $T_1 = 6.7$ sec (± 0.3 sec), and the flourines in $(\text{CF}_3)_2\text{CHOH}$, where $T_1 = 1.7$ sec (± 0.1 sec).

3.2.H Fourier-Transform NMR Spectroscopy

Once we have roughly located the resonance line for a given sample and magnet arrangement (*i.e.*, the shim thicknesses and a particular oscillator), we need not use the CW method again, and may instead use our FTNMR experiment as described in section 1.2.D and shown in figure 1.2.5. Our first applications of this sequence used adiabatic half passages for the encoding sequence, where we sweep the frequency to nearly the middle of the resonance line to approximate a $\pi/2$ pulse, because they have a wider excitation bandwidth than conventional hard pulses. We soon switched to using hard $\pi/2$ pulses for the encoding section of the sequence, and incorporated time-proportional phase incrementation (TPPI) to the second $\pi/2$ pulse to allow shifting of the time-domain frequencies to an arbitrary offset from the carrier frequency [28]. This allows us to shift the detected spectrum away from zero frequency in the rotating frame where excess noise due to slow drifts in instrument response is often problematic, while keeping the excitation pulses set to the center of a line or spectrum. To date, we have observed

proton linewidths as small as 6 kHz, corresponding to 200 ppm in the 0.64 T field (27.2 MHz for protons). We have achieved this linewidth without any provisions for fine control of shimming during a run, such as the detector magnet position, or any electromagnetic shims.

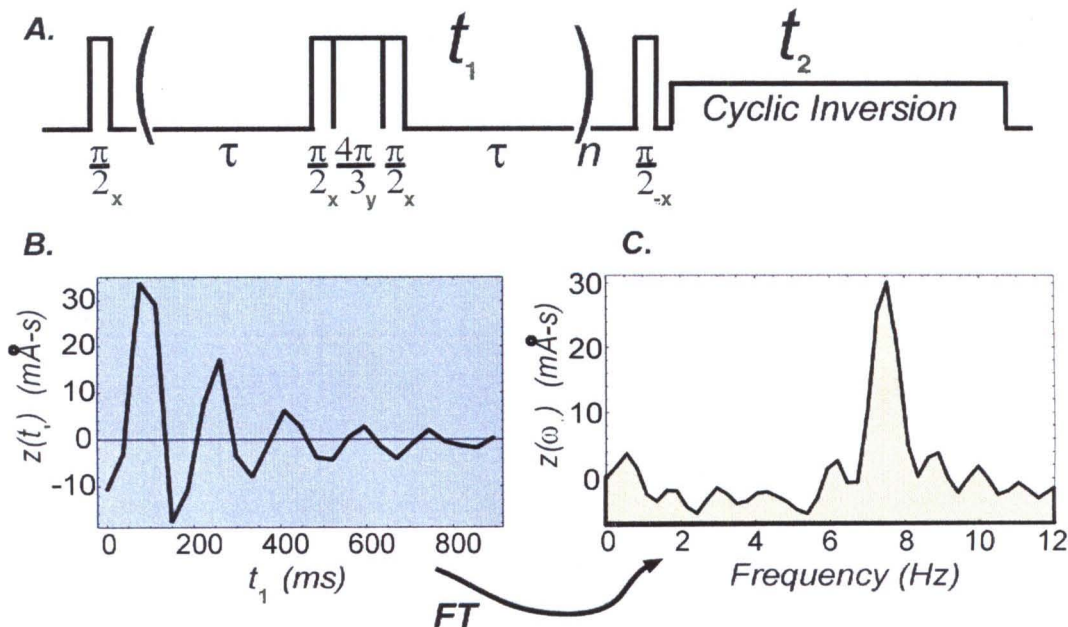
One notable feature of BOOMERANG FTNMR signals is the shape of the spectral lines due to the residual field inhomogeneity. Often we observe a small shoulder on one side of the NMR line, which is an artifact of the magnetic field generated by the BOOMERANG magnets. This artifact may be removed by suitable shimming using coils or permanent magnets, or by application of the reference deconvolution technique [29]. Garrett M. Leskowitz presents a Monte-Carlo simulation of this lineshape that agrees qualitatively with our measurements in his thesis [9]. This indicates that both the finite annular gap and the design of the field magnets contribute significantly to the observed lineshapes.

3.2.1 Spin Echoes, Echo Trains, and Use of Composite Pulses

In order to further show the generality of the BOOMERANG method, we applied spin-echo pulses to the spins to refocus magnetic field inhomogeneity and attain narrow spectral lines. Since we chose water as our test sample, diffusion dominates the linewidth for a single echo experiment [30, 31]. Therefore, by applying a train of π pulses we were able to achieve spectral linewidths as narrow as 0.8 Hz. In order to better refocus magnetization throughout the sample over many echo cycles, we applied the three-component compensated echo pulses [32] shown in figure 3.2.8. At a given rf power, and compared with simple π pulses, we observed greater than a factor of 2 gain in the time-domain signal decay time when using these compensated pulses. While more

complex schemes are known for inverting over a range of offsets, these pulses yielded good results and were simple to program, given our somewhat limited waveform generator memory [9]. More modern compensated π pulses should give longer echo decays approaching T_1 [33], as should the use of suitable adiabatic sweeps [24, 25], assuming data is collected only after even numbers of sweeps [34]. Use of the MLEV-4 echo supercycle constitutes a further improvement that we are pursuing to refocus cumulative echo-pulse errors [35].

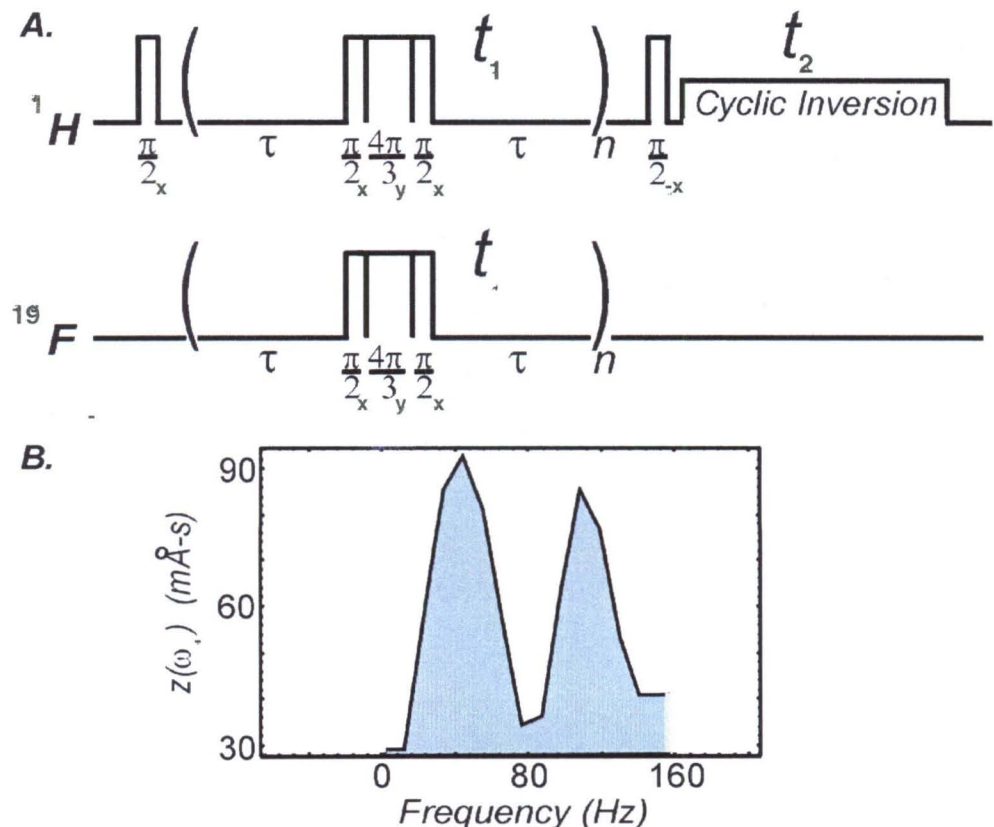
Figure 3.2.8: Compensated Spin-Echo Spectroscopy. Part A shows the rf pulse sequence applied to the spins - in this case, protons in a 2.6 mm sphere of DI water. We use the time-domain FTNMR pulse sequence of figure 1.2.5 with echo pulses inserted into the evolution time t_1 with delays of 2τ between them. We then increment the number of echo pulses n on successive shots of the experiment. After storing echo-encoded transverse magnetization onto the z-axis, we measure the resulting M_z for each shot using the cyclic inversion sequence to drive the mechanical oscillator. After Fourier transformation and weighting, each mechanical transient (measurement of M_z) becomes one point in the time-domain signal shown in B. Fourier transformation of B yields the echo spectrum C with a linewidth of < 1 Hz. The frequency axis ω corresponds to the offset from the carrier frequency of 27.2 MHz.



3.2.J Heteronuclear Echo Trains: J Spectroscopy

Once we obtained narrow lines in water, we extended our experiments to include measurement of a chemically relevant quantity – a scalar spin-spin (J) coupling. This successful measurement, using a modified version of the heteronuclear- J spectroscopy technique [36], represents the first force-detected observation of a multiple-resonance as well as a multi-nuclear NMR spectrum. Our modification to the standard heteronuclear- J spectroscopy pulse sequence is simply that we apply an incremented train of

Figure 3.2.9: Heteronuclear J Spectroscopy. Part A shows the rf pulse sequence applied to the ^1H and ^{19}F spins in the CH_2FCN (I) sample. Echo pulses applied to the fluorine spins serve to prevent decoupling of the heteronuclear J interaction. For this experiment, we measured only the proton magnetization using BOOMERANG detection. We carried out data collection and manipulations similar to the spin-echo spectrum of figure 3.2.8. The frequency axis represents the offset from the carrier frequency of 29.2 MHz (^1H).



compensated π pulses to each spin species with fixed τ delays between them as shown in figure 3.2.9, as opposed to a single π pulse with incremented τ delays. In liquid samples such as the fluoroacetonitrile (CH_2FCN) studied here, this minimizes relaxation due to diffusion in residual field gradients.

Note that we apply a train of echo pulses to the ^{19}F nuclei at 27.5 MHz in synchrony with the ^1H echo train at 29.2 MHz to recouple the ^{19}F to the ^1H and observe the spin-spin splitting. We apply large numbers of echo pulses n during this sequence, and $n = 180$ in this experiment with $\tau = 240 \mu\text{s}$. After approximately 100 echo pulses, we observed decoupling of the ^{19}F from the ^1H and the resulting line broadening, which we attribute to cumulative pulse errors. The linewidth in figure 3.2.9B is limited by apodization in t_1 . We hope to remove this limitation on linewidth by implementing the above mentioned MLEV-4 supercycle [35], and improved compensated π pulses [33].

References

1. *Magnetic Component Engineering*, <http://www.magneticcomponent.com/>. 1997, Inglewood, CA.
2. *Sorbothane Inc*, <http://www.sorbothane.com/>. 1997, Kent, Ohio.
3. *Carpenter Steel Co*, <http://www.cartech.com/>. 1998, Wyomissing, PA.
4. *Thermophysical properties of matter*. The TPRC data series; a comprehensive compilation of data, ed. Y.S. Touloukian. Vol. 13. 1970, New York: IFI/Plenum.
5. *Indium Corporation of America*, <http://www.indium.com/>. 1998.
6. *Oz Optics*, <http://www.ozoptics.com/>. 1998, Carp, Ontario, Canada.
7. *Thorlabs Inc*, <http://www.thorlabs.com/>. 1999, Newton, NJ.
8. *Wave Optics Inc*, www.waveoptics.com. 1999, Mountain View, CA.
9. Leskowitz, G.M., *Force-Detected Magnetic Resonance Independent of Field Gradients*, Chemistry Ph.D. 2002, California Institute of Technology: Pasadena, CA.
10. Kempf, J.G., *Probing Quantum Confinement at the Atomic Scale with Optically Detected Nuclear Magnetic Resonance*, Chemistry Ph.D. 2001, California Institute of Technology: Pasadena, CA. p. 181.
11. *Accuratus Inc*, <http://www.accuratus.com/>. 2000, Washington, NJ.
12. *CRC Handbook of Chemistry and Physics*. 74th ed, ed. D.R. Lide. 1994, Ann Arbor: CRC Press.
13. Yasumura, K.Y., *et al.*, *Quality factors in micron- and submicron-thick cantilevers*. Journal of Microelectromechanical Systems, 2000. **9**(1): p. 117-125.
14. Baierlein, R., *Newtonian Dynamics*. 1983, New York: McGraw-Hill.
15. Goldstein, H., *Classical Mechanics*. 2nd ed. 1980, Reading, MA: Addison-Wesley.
16. *Well Diamond Wire Saws*, <http://www.welldiamondwiresaws.com/>. 2000, Norcross GA.
17. Bloch, F., W.W. Hansen, and M. Packard, *The Nuclear Induction Experiment*. Physical Review, 1946. **70**: p. 474.
18. Abragam, A., *Principles of Nuclear Magnetism*. 1961, Oxford: Clarendon Press.

19. Leskowitz, G.M., L.A. Madsen, and D.P. Weitekamp, *Force-detected magnetic resonance without field gradients*. Solid State Nuclear Magnetic Resonance, 1998. **11**(1-2): p. 73-86.
20. Yannoni, C.S., *et al.*, *Force Detection and Imaging in Magnetic Resonance*, in *Encyclopedia of Nuclear Magnetic Resonance*, D.M. Grant and R.K. Harris, Editors. 1996, John Wiley: New York.
21. Madsen, L.A., Leskowitz, G. M., and Weitekamp, D. P., *Observation of Force-Detected Nuclear Magnetic Resonance in a Homogeneous Field*. Manuscript In Preparation, 2002.
22. Hardy, C.J. and W.A. Edelstein, *Tailoring Broad-Band Inversion With Efficient Adiabatic Fast Passage*. Journal of Magnetic Resonance, 1986. **69**(1): p. 196-199.
23. Kupce, E. and R. Freeman, *Adiabatic Pulses For Wide-Band Inversion and Broad-Band Decoupling*. Journal of Magnetic Resonance Series A, 1995. **115**(2): p. 273-276.
24. Kupce, E. and R. Freeman, *Optimized adiabatic pulses for wideband spin inversion*. Journal of Magnetic Resonance Series A, 1996. **118**(2): p. 299-303.
25. Hwang, T.L., P.C.M. van Zijl, and M. Garwood, *Fast broadband inversion by adiabatic pulses*. Journal of Magnetic Resonance, 1998. **133**(1): p. 200-203.
26. Waugh, J.S., L.M. Huber, and U. Haberlen, *Approach to High-Resolution nmr in Solids*. Physical Review Letters, 1968. **20**(5): p. 180-182.
27. Purcell, E.M., H.C. Torrey, and R.V. Pound, *Resonance Absorption by Nuclear Magnetic Moments in a Solid*. Physical Review, 1946. **69**: p. 37.
28. Weitekamp, D.P., *Time-Domain Multiple-Quantum Nmr*. Advances in Magnetic Resonance, 1983. **11**: p. 111-274.
29. Metz, K.R., M.M. Lam, and A.G. Webb, *Reference deconvolution: A simple and effective method for resolution enhancement in nuclear magnetic-resonance spectroscopy*. Concepts in Magnetic Resonance, 2000. **12**(1): p. 21-42.
30. Carr, H.Y. and E.M. Purcell, *Effects of Diffusion on Free Precession in Nuclear Magnetic Resonance Experiments*. Physical Review, 1954. **94**(3): p. 630-638.
31. Slichter, C.P., *Principles of Magnetic Resonance*. 3rd Enlarged and Updated ed. Springer Series in Solid-State Sciences 1. 1990, New York: Springer-Verlag.

32. Levitt, M.H., *Composite Pulses*. Progress in Nuclear Magnetic Resonance Spectroscopy, 1986. **18**: p. 61-122.
33. Smith, M.A., H. Hu, and A.J. Shaka, *Improved broadband inversion performance for NMR in liquids*. Journal of Magnetic Resonance, 2001. **151**(2): p. 269-283.
34. Kupce, E., *Personal Communication re: Use of ARP as echo pulses*. 2000.
35. Levitt, M.H., R. Freeman, and T. Frenkiel, *Supercycles For Broadband Heteronuclear Decoupling*. Journal of Magnetic Resonance, 1982. **50**(1): p. 157-160.
36. Goldman, M., *Quantum Description of High-Resolution NMR in Liquids*. International Series of Monographs on Chemistry. 1988, Oxford: Clarendon Press.

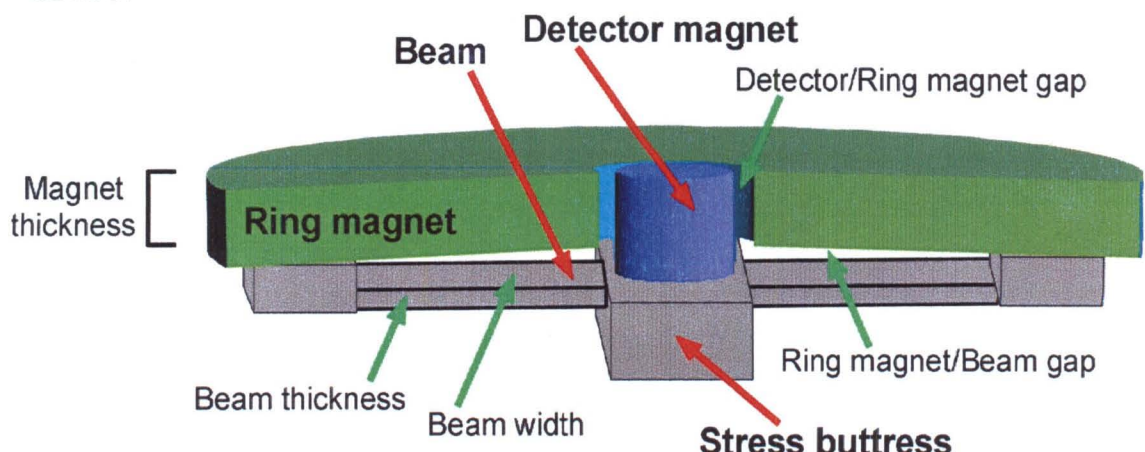
Chapter 4: Fabrication of a BOOMERANG FDNMR Spectrometer for Micron-Scale Samples

4.1 Fabrication Goals and Reasonable Expectations

We seek a practical and robust microfabricated BOOMERANG detector with acceptable homogeneity for efficient whole-sample spin inversion and coherent multiple-pulse spin manipulation, and with optimal sensitivity to spin magnetism in bulk samples. The key design challenges for the 60- μm -sample detector consist of the following: 1) definition of a narrow, unobstructed detector/ring magnet gap to obtain sufficient field homogeneity and low dissipation mechanical oscillations, 2) coplanar detector and ring magnets for minimization of inhomogeneity and DC magnetic forces, 3) deposition or

Figure 4.1.1: Microfabricated BOOMERANG Detector Element.

We define detector and ring magnets on a silicon substrate, where the detector magnet is bound to a silicon beam to form a composite mechanical oscillator. A buttress may be necessary to compensate for stress inherent in the detector magnet. The thickness of the magnets influences the sensitivity, and to a lesser extent the field homogeneity. The detector/ring magnet gap has the greatest influence on field homogeneity, as does the magnet planarity. All beam dimensions and the detector magnet mass influence the resonance frequency of this composite oscillator. Two of the structures depicted reside symmetrically above and below the sample to form the complete BOOMERANG device.



incorporation of thick (up to 20 μm) films of low-stress magnetic material, 4) definition of oscillator beams with desired frequencies, low mass, and low intrinsic mechanical dissipation, 5) reduction of eddy current damping in the magnet structures, and 6) fabrication of a robust assembly suitable for use at various NMR static field strengths in both portable *in-situ* studies and in laboratory studies. Figure 4.1.1 shows a cutaway view of the desired structure with design points highlighted.

In order to satisfy these stated goals, we have arrived at a specific set of dimensions and parameters for our device. Perhaps our simplest guideline is that we wish to operate this device at ambient temperature, thus allowing portable *in-situ* NMR measurements, biological studies at physiological conditions, and general solution studies, while obviating the need for a complicated cooling apparatus. Nonetheless, it may be fruitful to cool the apparatus for certain experiments, and the device has no particular limits in this capacity.

As mentioned in section 2.1.A the saturation magnetization M_s of iron ($2.1 \text{ T}/\mu_0$) sets a practical limit to the sensitivity of this detector, and we endeavor to achieve this magnetization in our detector magnet and surrounding ring magnet. Due to the linear scaling of sensitivity with magnetic field B_0 when B_0 is above the saturation field of the detector magnet, we obtain only limited sensitivity gains by increasing the field substantially above that point. Thus for a portable spectrometer we choose permanent magnets to generate our polarizing field and have a reasonable goal of $B_0 \sim 2 \text{ T}$. Of course, gains in resolution and sensitivity are still realized in the much higher fields available in commercial superconducting magnets (up to $\sim 20 \text{ T}$), such that for earth-

based laboratory experiments we may implement BOOMERANG detection in these magnets.

As stated above, we have optimized our device dimensions for a 60 μm spherical sample to reside between two BOOMERANG detectors. Since the magnetic force

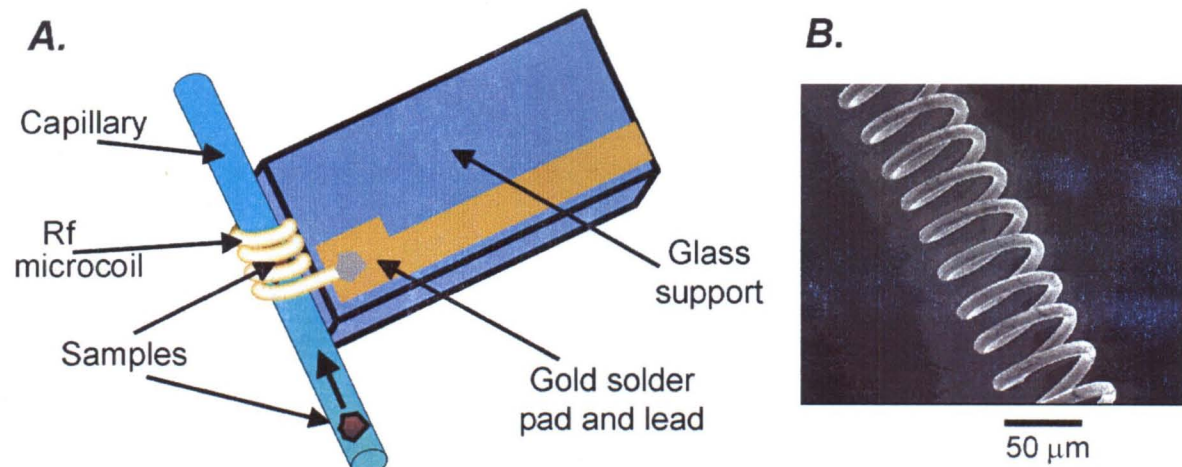


Figure 4.1.2: Proposed Microcoil Excitation Probe for MEMS BOOMERANG Spectrometer. In part A, an rf microcoil is wrapped on a capillary (40-50 μm ID) which contains and shuttles solid or liquid samples. The capillary-coil assembly is bonded or glued to a glass, silicon, or Be_2O_3 support plate (e.g., 50 μm glass coverslip) with patterned gold leads and solder pads. This probe assembly is then sandwiched between FDNMR detector planes. Rf circuit elements might be incorporated onto the glass or silicon support. Part B shows a 60 μm -ID coil made from 8 μm wire by Wes Hoffman at Edwards AFB [1], who has supplied similar coils for our first probes.

between the detector magnet and a sample with its center at a fixed distance from the detector magnet falls as $1/r^3$, where r is the sample radius, and since the sensitivity of the detector magnet to sample dipole elements falls as $1/R^4$, where R is the detector-dipole element distance, we have designed the device to have the smallest clearance possible between the detector magnet and the sample. The rf coil and sample holder may increase this minimum distance, although considerable engineering is still needed in these areas of

compact, high-power coil fabrication and efficient sample handling. Figure 4.1.2 shows a configuration we are developing for an excitation probe incorporating an rf microcoil and sample holder. We intend to use microcoils built at Edwards Air Force Base (AFB) by Wes Hoffman [1], similar to those shown in figure 4.1.2, as the first excitation coils. These coils are 60 μm ID, have 8 turns with 5 μm spacing per turn, and are made with 12 μm copper wire. Future microfabrication processes might incorporate microcoil leads and sample channels defined directly onto the BOOMERANG detector substrate wafer.

Based on the continuum mechanics and magnetic spring constant calculations in sections 2.1.D and 2.2.A, and on published data for similar size oscillators [2-4], we expect to microfabricate a mechanical oscillator structure with resonance frequency ν_h in the 1 – 10 kHz range, ringdown time τ_h of ~ 1 sec, and motional mass within a factor of two of the detector magnet mass. The resonance frequency must be sufficiently low to allow spin inversion for ~ 1 sec with rf power low enough to prevent excessive heating of the sample or the oscillator. A long ringdown time and a low mass of the oscillator increases the sensitivity of the device to magnetic moments.

Magnetic field homogeneity gives another essential requirement for this device. As discussed in section 1.2.C, we require field homogeneity for three reasons: acquisition of narrow NMR lines to provide high-resolution spectroscopy, minimization of diffusion-driven relaxation in liquids, and coherent manipulation of the magnetization of the whole sample. I list these requirements in increasing order of importance. Based on the finite-element method (FEM) magnetostatic calculations in section 2.1.C, and on experimental observations with the macro-scale prototype spectrometer, we have initially set aside the first homogeneity requirement and strive to attain field homogeneity of a

few-hundred ppm or better over the whole sample volume. This compromise does not substantially limit NMR capabilities in solids, and has some limited detrimental effects on liquid-state NMR (see sections 1.2.C and 3.2.J).

Initially, we have chosen to fabricate detectors \sim 8 mm apart in a square array of *dies*, giving \sim 100 devices, one per die, on a single 100 mm-diameter circular wafer. This wide spacing of devices relative to their sizes allows easy addressing and tracking of visual properties of the devices during fabrication, and simplifies post-process handling, including assembly of an *in-situ* spectrometer. Our goal of simultaneous NMR data collection on massive arrays of samples poses further challenges for parallel displacement sensor incorporation. Device packing density also depends more fundamentally on oscillator beam geometry and on ring magnet shape and diameter.

4.2 Microfabrication Methods Overview

4.2.A. Basic Concepts in Microfabrication

Conventional microfabrication, or micromachining [5], relies on three basic classes of technology: lithography to define patterns on a substrate, selective etching of patterned structures or substrates, and deposition of materials onto patterned structures or substrates. The materials available range from semiconductors, to insulators, to metals, which may be in elemental, doped, alloyed, or compound form. These materials may exist in glassy, polycrystalline, crystalline, or even porous states. Substrates generally consist of single-crystal silicon wafers 100-1000 μm thick and 5-25 cm in diameter, but may also consist of quartz, GaAs, or other materials. At the micron to nanometer scales, these conventional microfabrication techniques may be augmented by processes such as laser ablation, focused ion-beam milling, and microsphere lithography.

1. *Lithography Methods*

Lithography methods include the following common variants. *Shadow masking* involves shining light, ions, or atoms through patterned openings in a mask onto a substrate. Typically, this method is used in achieving a pattern when evaporating metal onto a silicon substrate, and is used when tolerances below a few microns are not required. *Photolithography* and *electron-beam lithography* selectively irradiate light- or electron-sensitive polymers to pattern a chemically and mechanically protective layer bound to the substrate surface. Conventional photolithography can achieve resolution as fine as $\sim 0.15 \mu\text{m}$ while enabling parallel production of patterns by including many duplicates of a pattern on a single template, or *mask*. Electron-beam lithography allows for resolutions as small as $\sim 20 \text{ nm}$, but relies on raster scanning a finely focused electron beam and thus has much lower throughput.

A typical photolithography sequence used to define patterns on a substrate proceeds as follows. A light-sensitive polymer, or *photoresist*, is spin coated onto one side of a nominally planar wafer. UV light passes through a *mask*, often a quartz plate coated in the desired pattern with chromium, and *exposes* the photoresist on the wafer. Photoresists are termed *negative* if they are strengthened (*e.g.*, cross-linked) by UV light irradiation and exposed resist remains where irradiation occurred, or *positive* if they are decomposed by UV irradiation. In a positive-resist process, photoresist that was exposed to light is then chemically *developed*, *i.e.*, dissolved away to leave open areas of substrate in the pattern defined by the mask's transparent areas. The wafer is protected by the remaining photoresist in the pattern of the mask's opaque areas. This remaining photoresist is nominally chemically inert and is strongly bound to the substrate, thus

providing protection from many chemical etchants and from direct binding of deposited materials. Fabrication tolerances are limited by the accuracy of mask definition, the choice of photoresist type and the quality of the photoresist film, the specific exposure and development parameters, and ultimately by the diffraction limit set by the wavelength of UV light used for exposure. Electron-beam lithography proceeds in the same manner but uses electron-sensitive photoresists, and exposes them by raster scanning the focused electron beam rather than shining it through a mask.

Patterned layers of photoresists or other materials, such as SiO_2 , Si_3N_4 , or metals, may also be defined by photoresist-based lithography in order to utilize these materials' differential selectivities under chemical or physical processes. Often such patterned materials are used as *masking layers*, which protect underlying features from removal, or *sacrificial layers*. After definition of a sacrificial layer, further microfabrication processes are applied, such as material deposition, followed by etching of the sacrificial layer to open a via or to release a mechanical structure to move on specific supports.

2. Selective Etching of Materials

Selective etching techniques span three subclasses: “wet” chemical etching, “dry” chemical reactive-ion etching (RIE), and ballistic ion etching. The first two classes further exhibit anisotropic or isotropic etching properties depending on the specific chemistry, substrates, or etching conditions used. Anisotropic processes etch selectively with respect to material dimensions or crystal lattice, while isotropic processes etch equally well in all directions. The third class, also termed ion milling or sputtering, simply involves acceleration of inert ions, such as Ar^+ , at high energies onto a substrate to ablate material away, and is necessarily anisotropic.

Wet etching is simply the dissolution of materials by immersing part or all of a wafer in a liquid solvent. Lithographically defined layers of photoresist or other materials may be used to protect against various wet etchants and are effective over various time periods, temperatures, and concentrations. Perhaps the most common example of isotropic wet etching is the selective dissolution of SiO_2 by $\text{HF:H}_2\text{O}$ or $\text{HF:NH}_4\text{F}$ solutions, where the latter is termed *buffered oxide etchant*, or BOE. These solutions dissolve SiO_2 equally in all directions relative to the device, while leaving Si and many other materials unharmed for etching times of up to several hours. A common example of anisotropic wet etching is the dissolution of single-crystal Si by aqueous KOH solution. KOH etches silicon more quickly in the (100) direction than in the (110) or (111) directions, and thus the etching follows (111) planes. As a result, Si (100)-oriented wafers exhibit etching profiles that follow the magic angle (54.7°) relative to the plane-normal direction [5]. The KOH etch-rate selectivity between Si and SiO_2 is $\sim 1000:1$ so that SiO_2 may be used as a protection layer for patterning silicon using KOH.

Dry etching, also called plasma etching or reactive-ion etching (RIE), involves chemical reaction of ions in a plasma with a substrate material, followed by desorption of the reacted species and removal by diffusion into a vacuum pump. The most common method of isotropic dry etching is O_2 plasma etching, in which the substrate wafer is bathed in a slowly flowing O_2 plasma that oxidizes and carries away organic species, such as photoresist residue. Reactive-ion etching, or RIE, is anisotropic, and usually involves unidirectional acceleration of ions toward a substrate such that the plane of the substrate perpendicular to the ion motion is preferentially etched relative to the direction along the ion motion. The selectivity between “floor” and “wall” etching is typically in

the 10:1 range, which similarly limits the achievable aspect ratio. The chemical selectivities of certain etch gases between different materials are also in the 10:1 range.

A more sophisticated version of RIE, termed deep RIE (DRIE) or a “Bosch process,” provides much higher selectivity both chemically and spatially, and is a key component of the BOOMERANG microfabrication process. In this technique, the etching process involves two steps. For silicon etching, which is most common, the first step deposits a conformal protection layer onto the substrate composed of quasi-polymerized C_4F_8 ions. SF_6 ions are then accelerated perpendicular to the substrate. The ballistic energy of the SF_6 ions striking the substrate preferentially and quickly removes the fluoropolymer protection layer on floor surfaces (parallel to the plane of the substrate), but cannot efficiently remove the protection layer on the walls (nominally perpendicular surfaces). The SF_6 etchant ions then chemically react with the substrate on the floor for several seconds until they begin to substantially erode the protection layer on the walls. At this point the etching is stopped, and these two steps, *protect and etch*, are repeated to etch the material. Often the first step is the etch step, followed by the repeated protect and etch cycles. For silicon etching, this cycle is typically 10-20 sec. long and has etch rates of $\sim 3 \mu\text{m}/\text{min}$. Selectivities between different materials, used as masking layers or substrates, can easily be as high as 1:400, as is the case for the $\text{SiO}_2:\text{Si}$ etch rate ratio. The selectivity for floor vs. wall etching can reach $\sim 100:1$, such that very high aspect ratio structures are possible. We define the BOOMERANG micro-oscillator beam structure out of a bulk silicon substrate using DRIE.

3. Deposition and Modification of Materials

The most common methods of materials deposition are physical vapor deposition (*e.g.*, sputter deposition or evaporation), chemical vapor deposition (CVD), and electrodeposition. These are listed in rough order of increasing deposition thickness capacity, and in decreasing order of film quality.

The first method is termed physical vapor deposition because it relies on removal of atoms from a solid reservoir, also termed a “source” or “target,” and adsorption of these chemically inert atoms onto an electrically neutral substrate. Sputtering consists of the ejection of atoms from a target by rf electric fields, or by bombardment by chemically inert ballistic ions, such as Ar^+ , and subsequent adsorption of these atoms onto a nearby substrate to form atomically pure and sometimes crystalline structures. Film growth may be controlled down to single atomic, or epitaxial, layers if the correct conditions are used, as in the technique of molecular beam epitaxy (MBE).

Evaporation of atoms from a pure solid “source” is achieved by heating a region of the solid with a high-energy (~ 10 kV) electron beam. Atoms boiling off of the source fly radially outward and adsorb onto structures of the nearby substrate that are in the line of sight of the source solid. Usually metals or semiconductors are coated to 10-3000 Å thickness in this way, and evaporation represents a staple technique in conventional microfabrication.

Chemical vapor deposition (CVD) refers to a class of methods by which molecular plasmas or neutral gases react to form solids on a substrate. Gas phase molecules are broken into neutral radicals or ionized to form reactive species in a vacuum chamber and are accelerated onto a substrate, sometimes with the aid of an inert carrier

gas. Due to the reduction of free energy when the molecular ions react with each other, a solid film grows on the substrate [5].

Electrodeposition, or electroplating, of metals forms another important method of controllable film deposition. Two electrodes are placed into an aqueous solution of metal ions, called a *bath*, and a voltage difference is applied between them. A current develops in the solution, and positively charged metal ions are reduced at one electrode, called the cathode, and plate onto its surface. A patterned wafer substrate with a conductive metal *seed layer* evaporated onto it may be used as this reducing electrode such that only conductive surfaces that require film deposition are exposed to the solution. Negative counter ions, typically Cl^- or OH^- , are oxidized at the other electrode, called the anode, and combine to escape as gases. Variation of voltage difference, temperature, ion concentrations, bath conductivity, exposed cathode area, and additives can be used to modify film growth rate and material properties. Electrodeposition allows film thicknesses of ~ 100 nm to hundreds of microns on patterned substrates. Alloys with desirable electric or magnetic properties may be electrodeposited by varying relative concentrations of combinations of metal salts in solution. Our BOOMERANG fabrication process uses electrodeposition of NiFe, CoNiFe, or CoNi alloys to produce the detector and ring magnets.

A related class of material creation is that of direct chemical or physical modification of a resident material by heating and/or exposure to reactive gases. A prime example of this is the oxidation of silicon to produce a well-defined SiO_2 layer. This process, also called “wet oxidation” because water vapor is present during oxidation, occurs by diffusion of oxygen atoms into the silicon lattice and chemical reaction to form

SiO_2 . The oxidation is carried out in an atmosphere of oxygen and water gases in an oven at high temperatures ($\sim 1000^\circ\text{C}$). Doping of silicon by boron or other atoms may also be accomplished in this way. These diffusion methods are practically limited to ~ 2 μm layer thickness due to the decreasing rate of atomic diffusion further into the substrate material. These materials are frequently used as masking layers, or as *etch stops*, which serve to firmly terminate etching of another material (*e.g.*, silicon) at a given layer or depth.

4.2.B. General Comments on the Culture of Microfabrication and Science

Before beginning my discussion of the BOOMERANG microfabrication process, I present my viewpoints on the use of microfabrication to realize scientific instruments or experiments, specifically the nature of collaborations between scientists, *i.e.*, theorists and designers, and hands-on micromachinists.

It is inevitable that these two groups approach problems of manufacture from different points of view. Scientists tend to view manufacturing problems conceptually, and with minds set toward constant optimization and understanding of as much of the problem's intricacies as possible. Able micromachinists generally approach these problems with focus on attaining working structures quickly using the tools available to them. They reserve room for process innovation and improvement of their basic knowledge, but place less emphasis on understanding the physics or chemistry of the specific steps involved.

For fabrication techniques less than about 10 years old, MEMS resembles science, where technological innovations are not made instantly available to the average

practitioner. One needs to develop expertise to use each new bit of technology. Statements such as “MEMS can achieve 10:1 aspect ratios” means that unless an experienced fabricator is employed with excellent equipment, it will take non-trivial development to achieve such a quality. The assumption of micromachinists is generally that a device process will have a few difficult or critical steps, but will mostly use stock procedures. Furthermore, certain combinations of processes and/or materials may be incompatible, and unless a micromachinist is expert in many processing motifs, it may be difficult to identify these incompatibilities when designing a process. Literature searching and reading will aid this foresight, although given the range of processes available, published information may not exist, may be incomplete, or may not adequately describe the pitfalls of a processing combination. Ultimately, hands-on experience of a fabricator with many combinations of processes leads to the best information.

Microfabrication equipment for prototype work requires frequent and highly specialized maintenance and calibration to attain reproducibility and durability. Often, equipment failure causes long delays in processing, or the equipment produces different results after repair such that more time must be spent to reoptimize a given processing step. It is the responsibility of micromachinists to know the capabilities of their equipment and materials, and to adequately inform the scientist of these properties and limitations. Similarly, the scientist should become informed about equipment capability, material properties and limitations, and process difficulty before initiating design or process changes. Both groups should also become familiar with recurring contamination issues and material property fluctuations and tolerances.

Ideally, a first-run process should be designed to have either few or no difficult steps that would require process optimization, and as few total steps as possible in order to realize the desired device or a close approximation to it. For a complex first-run process, specialized microfabricators and scientist-designers must have frequent and meaningful communication in order to ensure that combinations of processes will not interfere with each other and to constantly reassess whether design goals are reasonable, and whether they are necessary or flexible. Micromachinists must also characterize and monitor their wafers vigilantly at each processing step both to avoid wasting time on wafers that have been ruined by a failed step or contamination, and to provide processing feedback (*e.g.*, yield, or trends in quality across a wafer) to collaborating fabricators and to scientist-designers.

As micromachinists make confident statements about processing capabilities, scientists naturally add complexity and optimization to a process without necessarily knowing the costs involved. When many “cutting edge” steps are incorporated into a fabrication process, this places larger demands on the fabricator to produce high yield for each difficult step. This leads to issues of device yield where often several devices on a wafer may have acceptable qualities for a given step, but after executing a many step process, variations over a wafer will result in no working devices.

Scientists might lean toward thinking of micromachining as having the same reliability that conventional machining does, in which macroscopic, complex working devices may be built with almost 100% yield on the first run through, assuming tolerances do not exceed a reasonable limit. I find it instructive to rather think of micromachining like synthetic chemistry, where each step of a complex synthesis might

have 50-100% yield, but after 20 steps, one is left with very little or no useable product. This analogy extends further in that a single difficult synthetic step, one prone to “oil out” instead of produce crystals, may postpone or ruin a synthesis indefinitely.

As a scientist and recently a micromachinist, I firmly recommend that scientists involved in MEMS instrumentation design spend some time actually training and working in a microfabrication clean room. Hands-on experience is irreplaceable, and I believe that valuable intuition may be gained in only a few weeks of solid work. Micromachinists should also spend ample time familiarizing themselves with the design and theory of the scientific instruments they attempt to build. This invested time, for both groups, will be more than repaid in the efficiency of future lab efforts and communication.

4.3 BOOMERANG Microfabrication Process Overview

After a search of methods for fabrication on the micron-scale (*e.g.*, diamond grinding, laser machining, self assembly), we chose to pursue bulk silicon micromachining at JPL as a reliable and parallelized method for building our micro-BOOMERANG detectors. In order to achieve ~ 20 μm -thick, high-saturation magnetic films necessary for our device, we electrodeposit detector and ring magnets composed of alloys of nickel, iron, and/or cobalt. We have contemplated several methods of fabricating the oscillator suspension, including use of ready-made 2 - 4 μm -thick monolithic films of silicon, definition of surface-deposited Si_3N_4 films, definition of boron-doped silicon films, definition of silicon-on-insulator (SOI) films, and use of deep RIE to define films from bulk silicon. While all of these methods have pros and cons, definition of oscillator beams using deep RIE presented the simplest, most readily

available, and most versatile method. In order to effectively separate the detector and ring magnets by a thin gap ($\sim 1 \mu\text{m}$ or smaller), and to separate the silicon oscillator beam from the ring magnet by a similar gap, we chose to use sacrificial layers between these pieces to build up the device structure, and then release it to freely oscillate.

4.3.A. Fabrication Process with Two-Step Magnet Deposition

In keeping with our design goals, our first microfabrication process was intended to satisfy requirements of the optimal cylindrical detector magnet size and aspect ratio, and field homogeneity. Attaining a $\sim 1 \mu\text{m}$ detector/ring gap for $18 \mu\text{m}$ -thick magnets using a single-step plating process requires defining a wall of photoresist $20 \mu\text{m}$ tall by $1 \mu\text{m}$ wide. This falls outside the $\sim 10:1$ maximum aspect ratio usually possible with conventional micromachining techniques. Exotic processes such as LIGA [5], which uses synchrotron X-rays for photolithography, may be able to achieve such a structure, but they are currently much less convenient and more costly. Thus, we decided to electroplate the detector magnet first, then deposit a thin sacrificial layer of oxide (as thin as $\sim 0.25 \mu\text{m}$) over this magnet, then electroplate the ring magnet, then polish the magnets to attain planarity, if necessary. Figure 4.3.1 shows a summary of this magnet definition process. Details of the beam definition using DRIE are identical in the current process, and thus I describe them in the next section. While this process in theory produces the optimum magnet structures, it has many difficult steps, thus reducing the chances of producing a working device. Also, by electrodepositing the detector magnet first, electric field inhomogeneity during plating can cause raised edges on the magnets, thus requiring polishing to planarize them.

Figure 4.3.1: Fabrication Process Summary with Two-Step Plating.

Note: individual die cross-section, dimensions not to scale

1) Pattern double-side align marks (not shown).



2) Deposit Cr/Au (200Å/1000Å) plating seed layer.



3) Pattern photoresist for detector magnet mold.



4) Electroplate detector magnet 18 - 20 μm thick and strip photoresist mold.



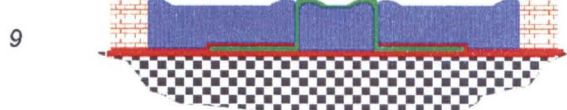
5) Deposit $\sim 1 \mu\text{m}$ PECVD SiO_2 for sacrificial layer and pattern etch stops.



6) Deposit Cr/Au (200Å/1000Å) plating seed layer.



7) Pattern seed layer to reduce magnet plating over detector magnet.



8) Pattern photoresist for ring magnet mold.



9) Electroplate ring magnet 18 - 20 μm thick.



10) Planarize magnets using chemo-mechanical polishing (CMP) - optional.

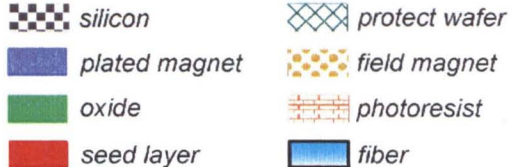


11) Protect front side by wax-mounting to dummy wafer.

12) Pattern backside and create stress buttress and oscillator beam using deep RIE (DRIE).

13) Remove dummy wafer, sacrificial oxide (BOE), and photoresist mold.

14) Bond field magnet and fiber to backside.



We actively pursued development of the steps of this process for two years before making an important compromise to switch to a single-step plating process. The magnet

deposition method described in the next section avoids the complication and polishing issues of the first process, while sacrificing 20 - 50% in the sensitivity of the device, and a modest decrease in field homogeneity. The lessons learned in investigating this first process directly apply to essentially any process involving electroplating of magnets. It may be advantageous to return to this first process for better magnet manufacture, after a working prototype is achieved.

4.3.B. Simplified Fabrication Process with Single-Step Magnet Deposition

With the knowledge that our first process was excessively complex, we redesigned our process to include much fewer steps of photolithography (from 10 masks to 6 masks total), and much fewer total steps (52 steps to 32 steps). The cost of this simplification lies in the sacrifice of magnet thickness, which decreases sensitivity, and the widening of the detector/ring gap to a minimum width of $\sim 1 \mu\text{m}$. While this process is still relatively challenging, we expect to achieve working devices in the next few months.

This process again uses sacrificial layers to separate the detector and ring magnets, and the oscillator beam. We electrodeposit both magnets simultaneously into a lithographically defined mold of photoresist which defines the outer edge of the ring magnet and separates the two magnets. For the detector magnet, this represents a method of “frame plating,” where magnets are deposited with only thin walls of photoresist between them to minimize electric field inhomogeneity, which causes poor surface morphology in the plated film. Thus, the resulting detector magnet is perfectly coplanar with the ring magnet, obviating the need for polishing.

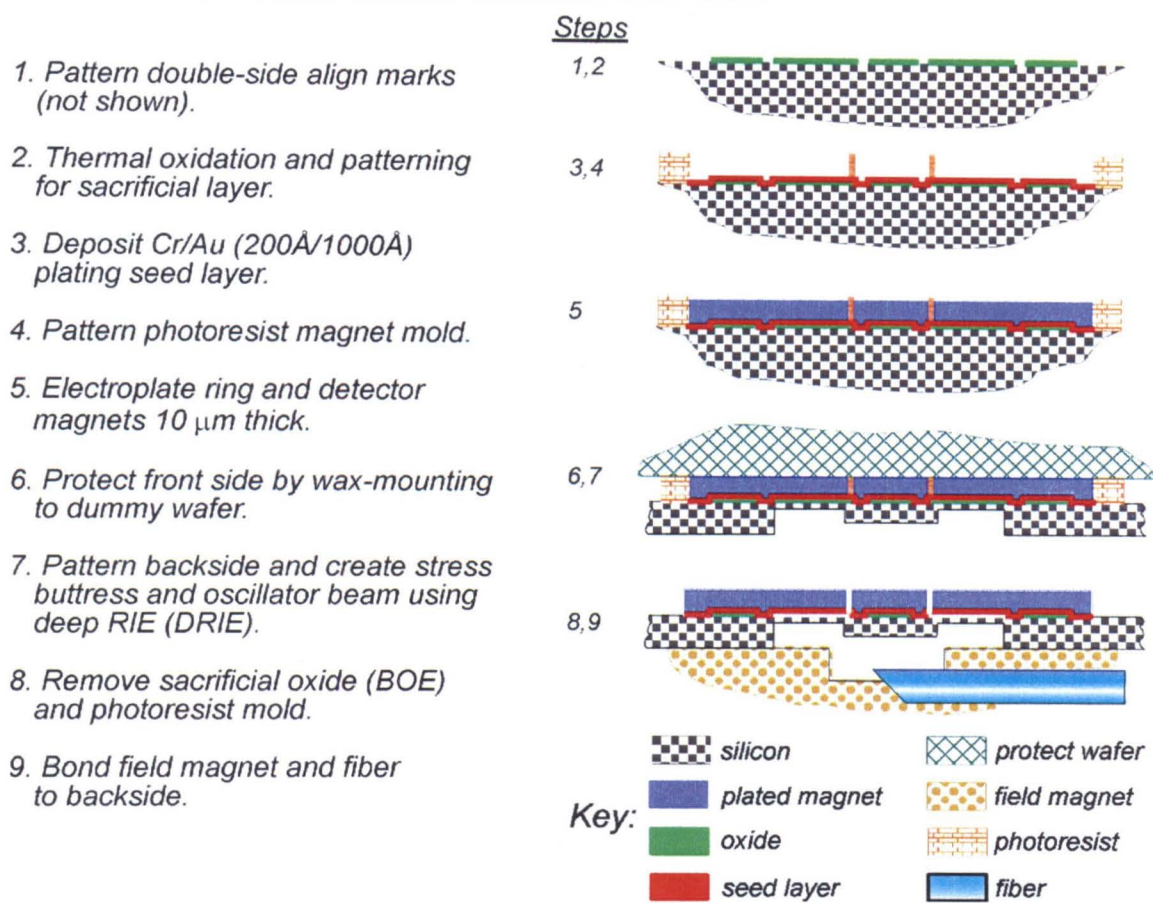
We define the oscillator beam: by patterning the side of the wafer opposite the magnets, the *backside*, and etching away silicon using DRIE to leave only the beam structure. Stress inherent in the plated magnet film may be extreme enough to buckle or twist the beam such that the detector magnet hits the ring magnet, or dissipation of the beam becomes unacceptable. Thus, we also define a reinforcement, or *butress*, by DRIE on the beam opposite where the detector magnet is bound in order to counteract stress induced in the beam by the magnet film.

We fabricate these structures on both sides of the substrate wafer, so in this process (as well as in the two-step plating process) we require alignment between the frontside and backside of the wafer to $\sim 5 \mu\text{m}$. We have used three methods to achieve this: using DRIE to punch alignment holes in the wafer, placing the wafer in an “alligator jaws” jig with precision hinges and alignment marks defined on masks on either side of the clamped wafer, and using a single mask and a contact aligner with optics for backside alignment to expose the alignment marks on both sides of the wafer sequentially. We currently use the last method since it produces the best alignment and is compatible with MDL’s contact aligner.

Figure 4.3.2 depicts a summary of the simplified microfabrication process. I include attachment of a transverse-fiber displacement sensor and a permanent magnet as part of this process for completeness.

Figure 4.3.2: Fabrication Process Summary with One-Step Plating.

Note: individual die cross-section, dimensions not to scale



4.4 The Refined Microfabrication Process: A Detailed Description

In this section, I attempt to include all concepts and details relevant to microfabrication of a micron-scale BOOMERANG spectrometer [6]. This process has resulted from careful design, experimentation, and feedback from many micromachinists at JPL and scientists at Caltech. Like any carefully crafted piece of art or machinery, specific reasoning underlies each step of this procedure, and I attempt to summarize our logic and experiences. Appendix B gives a process flow summary for quick reference on specific details of the microfabrication process.

4.4.A. Double-Side Alignment

In order to define magnets and oscillator structures on a monolithic wafer, our device consists of essentially two processes, each of which is carried out on opposite sides of the wafer. Since the magnets and oscillator beam must be precisely lined up with each other, we require alignment between patterns on the frontside (magnet side) of the wafer, and the backside (beam side) of the wafer to within $\sim 5 \mu\text{m}$. This $5 \mu\text{m}$ tolerance comes from the fact that our $50 \mu\text{m}$ -diameter magnet must lie within our $60 \times 60 \mu\text{m}$ buttress area. By adjusting the relative sizes of these structures, this alignment tolerance may be relaxed. This involves minor compromises of increased motional mass or smaller detector magnet diameter (see section 2.1.A), and increased allowable asymmetry in the position of the magnet relative to the center of the beam. Conversely, tightening this tolerance would allow a slightly more efficient detector in terms of sensitivity.

We use a device termed a *contact aligner*, in which the photolithography mask is placed in direct contact with the substrate wafer and UV light shines through the transparent parts of the mask to expose the photoresist on the wafer. By using the Karl Suss MA6/BA6 contact aligner at MDL, it is possible to achieve $\sim 1 \mu\text{m}$ -tolerance double-side alignment, and relatively easy to achieve $< 5 \mu\text{m}$ [7]. This device uses microscope objectives in precise alignment with each other to view both sides of the wafer simultaneously and subsequently expose photoresist on one side of a wafer with UV light (320 and 405 nm). The alignment quality and photoresist pattern resolution depends critically on the planarity of the wafer surface (including photoresist) and the absence of contaminants that would create space between the mask and the wafer surfaces.

Figure 4.4.1: Double-Side Align Marks.

Note: whole wafer cross-section, dimensions not to scale

1) Substrate wafer:

400 μm double-polished,
spin photoresist
(PR) both sides.



2) Mask 1: Align Marks

Expose 1 side
w/ 1:1 contact aligner,
develop PR.



3) Flip wafer,

align to backside,
expose/develop PR.



4) Reactive ion etch

(RIE) both sides
 $\sim 2 \mu\text{m}$ deep.

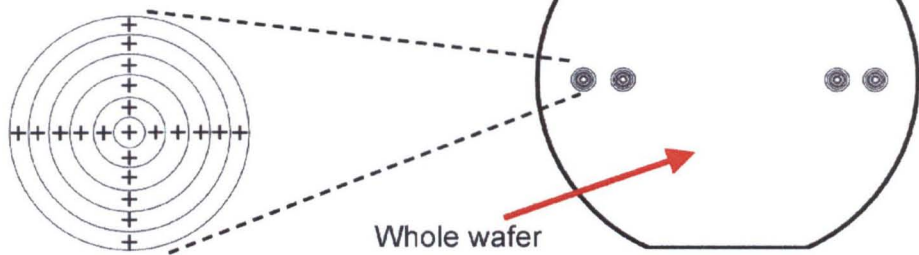


5) Strip PR.



These are *global align marks*
to orient successive masks
to the wafer.

Single
mark ==>



We execute the align-mark process as depicted in figure 4.4.1. We spin coat photoresist onto both sides of a fresh, double-polished wafer and expose one side in the contact aligner using our align mark mask, followed by backside alignment using the contact aligner and exposure of the second side using the same mask. We then place the wafer into photoresist developer and wash away the photoresist in the double-side-registered

patterns of the align marks. After this photolithography step, we do RIE on both sides of the wafer to etch away silicon in the shape of the align marks, then strip the photoresist.

These marks are termed “global” align marks since they serve to align the entire wafer with all masks in the fabrication process via optics present in the *projection aligner* (see next section) or the contact aligner. In our current process, we carry out lithography using only the projection aligner after align mark patterning. The align marks on the wafer must lie in a range of widths related to the alignment optics, essentially microscopes with crosshairs, present in the projection aligner and/or contact aligner. In addition, we have chosen these marks to be integer multiples of our die size so that the marks do not overlap device dies, and so by symmetry they are easier to find on the wafer. In our case, the four colinear align marks defined by **Mask 1** are spaced by 76.2 mm, and 50.8 mm, and so have three possible widths, 63.5 mm being the third, for viewing with alignment optics. I show a wafer with these marks at the bottom of figure 4.4.1.

4.4.B. Wafer Trench Etching and the Projection Aligner

Since we define oscillator structures using DRIE from the backside of the wafer, we need to etch through the entire thickness of the substrate wafer while maintaining the beam and buttress profiles. Early on in our process development, we carried out extensive testing to determine a substrate thickness that would allow preservation of the beam profile. Etching through an entire 400 μm wafer severely distorts the beam profile, while etching through $< 200 \mu\text{m}$ allows flat and uniform thickness beams to within $\sim 10\%$ over the beam area. In order to combine wafer strength with the best beam profiles,

we used 400 μm wafers as the starting material and etch 350 μm -deep square depressions for each die on the wafer. Thus, the device substrate is nominally 50 μm thick.

To attain best thickness uniformity (< 0.5 μm thickness difference over the wafer area after 350 μm etching) and ease of manufacture, we etch these depressions using a temperature-controlled KOH solution. The etch rate is 23 $\mu\text{m} / \text{hr}$. using a solution of 1.44 L of 45% KOH, 1.76 L of DI water, and 50 mL isopropanol at 60 $^{\circ}\text{C}$ with a stirbar spinning at 350 rpm (see also Appendix B). Since photoresist is attacked relatively quickly by this KOH solution, we employ thermally grown SiO_2 as a KOH-resistant masking layer. We require that this oxide layer be > 1 μm thick in order to ensure wafer protection over the ~ 15 hour etching process. Figure 4.4.2 shows the process used to define these depressions.

Figure 4.4.2: Backside KOH Etching Process.

Note: whole wafer cross-section, dimensions not to scale

1) Grow thermal oxide $\sim 1.5 \mu\text{m}$.



2) Spin PR both sides.



3) Mask 2:
KOH Etch
Expose/develop
PR on backside.



4) BOE to remove oxide on squares.



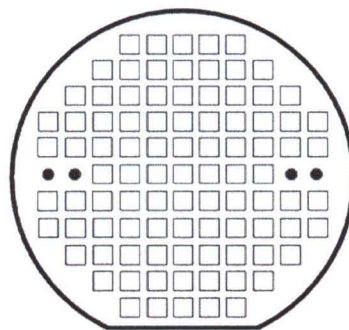
5) Strip PR, KOH etch for ~ 10 hours to create substrate thickness of $50 \mu\text{m}$.



6) BOE to remove remaining oxide.



Whole wafer =>
(backside
plan view)



For this photolithography step and all subsequent steps, we use a projection aligner, or *stepper*, to define patterns on the wafer. This device uses masks with patterns that are five or ten times the linear dimensions of the desired structures on the wafer, and focuses these patterns through a lens stack onto a single die on the wafer. This single die is then exposed with UV light, and all of the dies on the wafer are similarly stepped

through and exposed in turn. We refer to steppers that reduce mask patterns by five or ten times as “5X” and “10X” steppers, respectively. The stepping process is controlled interferometrically and is accurate to sub-micron tolerances, such that alignment and reproducibility are maintained. It is also possible to use different masks to expose different dies on one wafer. The registry of the mask with the exposure optics is achieved by viewing crosshair marks, or *fiducial marks*, on the mask through microscope objectives with similar marks, and then adjusting the position of the mask relative to the exposure optics. The exposure optics are then aligned to the wafer by aligning the wafer’s global alignment marks to crosshairs in microscope objectives fixed to the exposure optics. Once these alignment steps are accomplished, one may also program offsets (to $< 1 \mu\text{m}$ tolerance) of the mask relative to the optics such that if patterns are small relative to the die size, several mask patterns may be printed onto different locations on a single mask, and the patterns not in use are covered up to block the light leaving only the desired pattern exposed onto the photoresist.

In order to pattern the depressions on the wafer, we use MDL’s GCA DSW 5X stepper and **Mask 2**, which consists of a 30 X 30 mm square opening to produce 6 X 6 mm depressions for each die on the wafer, where the die step size is 7.62 mm in both dimensions. Due to the method of autofocusing employed in the stepper, similar to the utilization of an optical lever in atomic force microscopy, the depressions must be large enough so that the laser beams reflected off the wafer can exit the depression unblocked. This may require depression size and/or die size adjustment to allow stepper focusing.

4.4.C. Oxide Sacrificial Layer Definition

We create and pattern this sacrificial layer of SiO_2 to separate the ring magnet from the silicon beam during processing, and we etch it away at the end of the process to release the mechanical oscillator structure to freely vibrate. This sacrificial layer must be thick enough so that “stiction” forces do not pin the oscillator beam against the ring magnet upon dissolution of the sacrificial layer. Stiction is not fully understood in the MEMS literature [5], but it is known to involve a combination of electrostatic forces, van der Waals forces, and covalent chemical bonding. Stiction usually manifests when a liquid evaporates out of a sub-micron gap between planar surfaces. We have used a $\sim 1 \mu\text{m}$ -thick sacrificial layer in order to minimize the likelihood of stiction. Another method of counteracting stiction is to dissolve the sacrificial layer, then remove the solvent by drying the wafer in CO_2 at or above the critical point, an approach known as *critical-point drying*.

We have used two methods of creating this sacrificial layer: plasma-enhanced CVD (PECVD) oxide deposition and thermal oxidation. PECVD is a process by which SiO_2 is deposited on an arbitrary substrate at $\sim 250^\circ\text{C}$ with a rate of $\sim 400 \text{ \AA/min}$. PECVD oxide is somewhat porous, although it does create a chemical barrier when it is thicker than a few hundred nanometers. It also dissolves much more quickly in HF solutions, about ten times faster than thermal oxide. Thus, PECVD oxide may be more desirable as a sacrificial layer since long-time etching for beam release can cause magnets to corrode or peel off, or cause silicon beam damage (see also section 4.4.F). Thermal oxidation of the silicon wafer, as described in section 4.2.A.3, produces a near-crystalline oxide layer, and necessarily occurs over the whole wafer surface. We have so

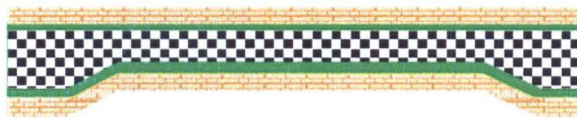
far favored thermal oxidation since it is a higher quality coating, and it simultaneously produces oxide on both sides of the wafer. The oxide on the backside provides a mask layer during the DRIE beam/buttress definition section of the process, as described in section 4.4.E.

After creation of the oxide layer (thermal or PECVD), we photolithographically define concentric rings using **Mask 3**, and etch the oxide away in those rings using RIE. Figure 4.4.3 shows these rings and the process steps involved. Carefully timed BOE etching may instead be used here, but we have found that this wet etching necessarily undercuts the photoresist to yield wider ring patterns than those defined by the patterned photoresist layer.

Figure 4.4.3: Oxide Sacrificial Layer Patterning.

Note: individual die cross-section, dimensions not to scale

1) Grow thermal oxide, 1-1.5 μm , Spin PR front side.



2) Mask 3: Oxide Define Expose/develop PR.



3) CF_4 RIE to etch oxide.



4) Strip PR.



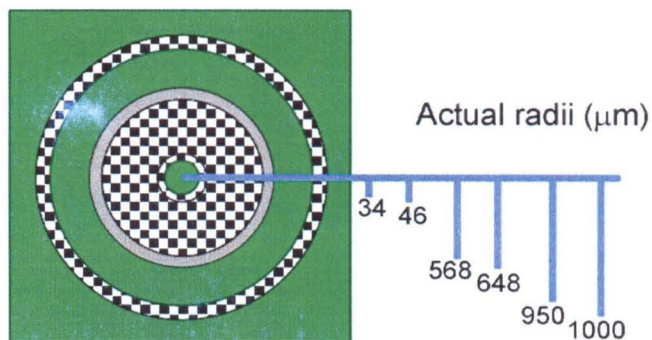
5) Deposit plating seed layer Cr/Au 200/1000A.



Frontside plan view before seed layer deposition (at step 4)

Key:

- ☒ silicon
- ☒ oxide
- ☒ seed layer
- ☒ photoresist



These concentric rings also serve to anchor the detector and ring magnets onto the silicon substrate so that most of the surface area of the magnets facing the beam (backside of wafer) are coplanar. This co-planarity is not necessary from a fabrication standpoint, but this geometry will provide the best magnetic field homogeneity in the BOOMERANG spectrometer. This oxide patterning step must achieve better than ~ 3

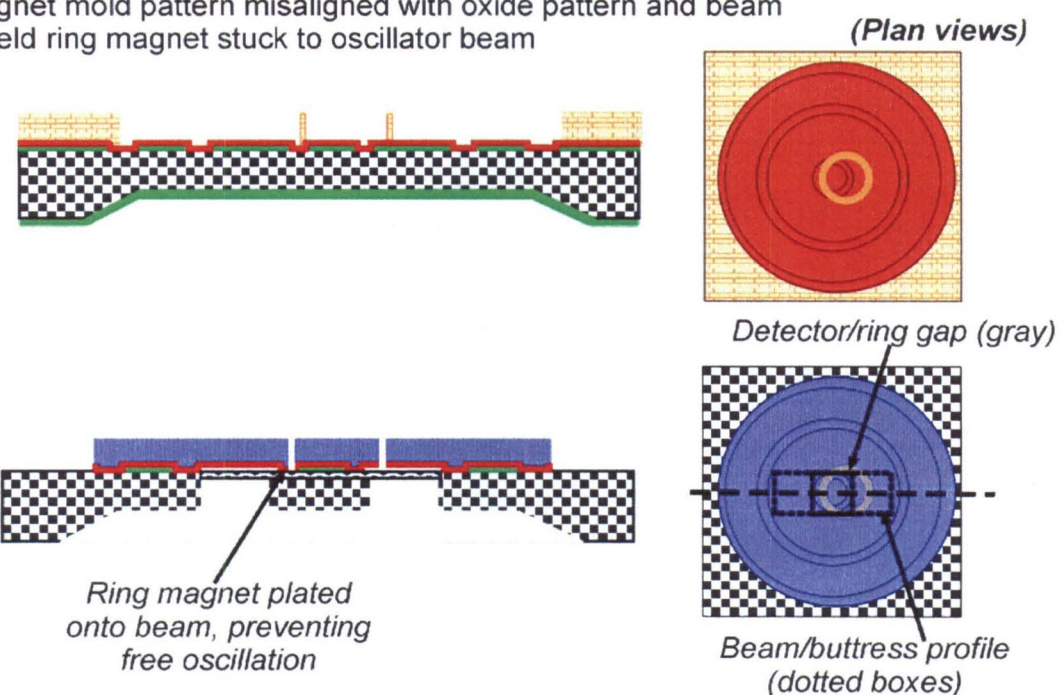
μm alignment tolerance relative to the magnet positions and the beam pattern such that:

1) the magnet mold pattern prevents electroplating any portion of the ring magnet onto the oscillator beam, and 2) the detector magnet is solidly anchored by a metal-to-silicon surface around its circumference to prevent lift off of the magnet from the beam during sacrificial layer etching. Figure 4.4.4 A and B illustrate these two misalignment modes of failure. The first may be attacked by designing the masks for oxide definition and magnet plating photoresist mold (**Masks 3 and 4**) to allow higher tolerance of misalignments, but this creates the same inefficiencies as described in section 4.4.A concerning front-to-back side alignment. The cure for the second failure mode, which we have incorporated in early processing runs, is to pattern the oxide such that the detector magnet is bound directly to the silicon over the whole backside surface of the magnet. I depict the solutions to these two failure modes in figure 4.4.4 C and D. For the first runs, we have settled on the latter cure and a smaller detector magnet anchor site to allow misalignments of up to $6 \mu\text{m}$ among all three (oxide sacrificial layer, magnet mold, and beam definition) mask patterns.

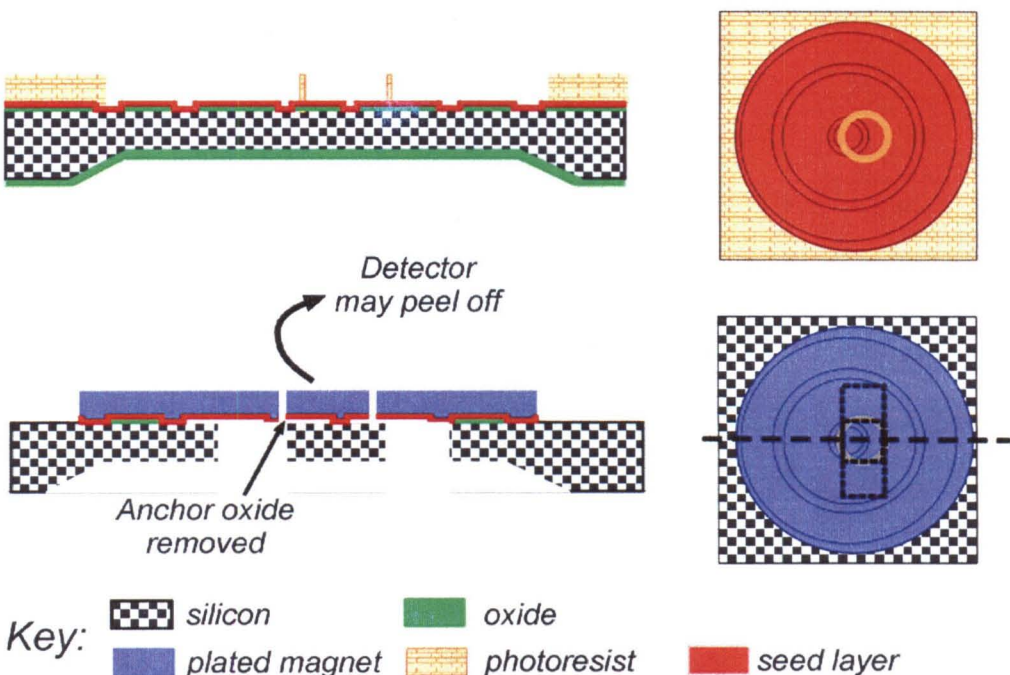
Figure 4.4.4: Pattern Alignment Failure Modes and Remedies.

Note: individual die cross-section, dimensions not to scale

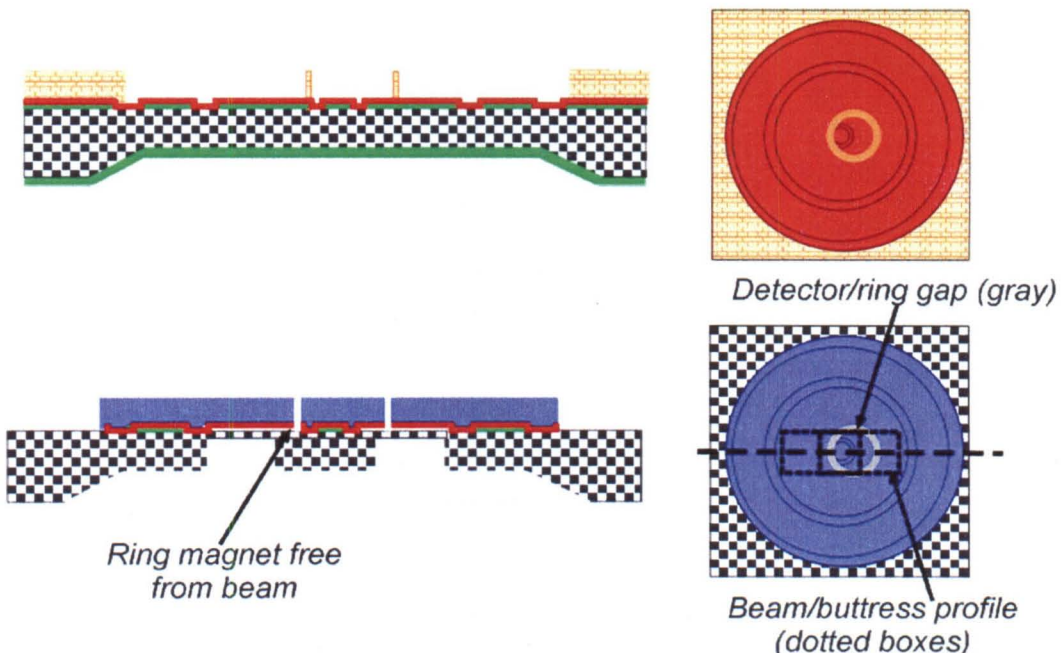
A. Magnet mold pattern misaligned with oxide pattern and beam to yield ring magnet stuck to oscillator beam



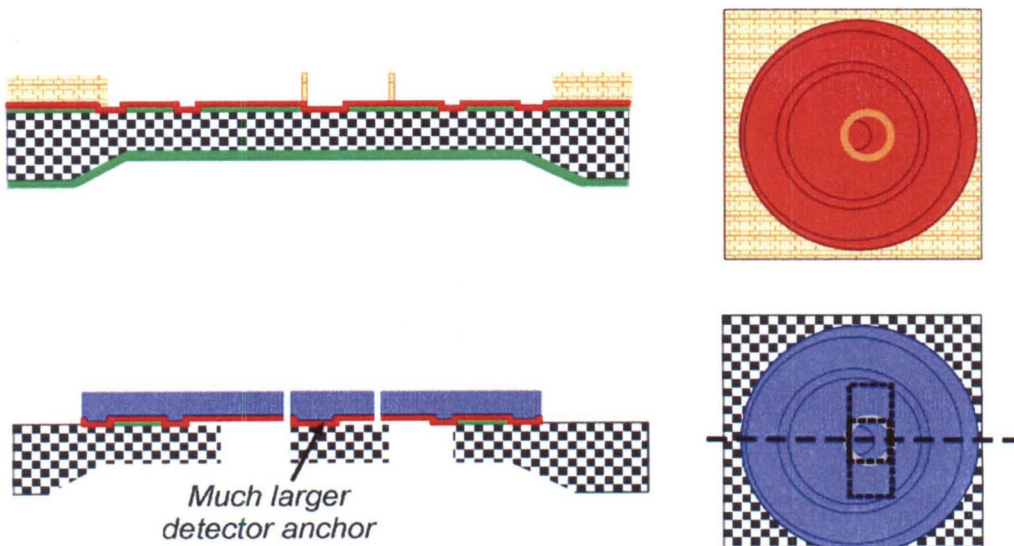
B. Magnet mold pattern misaligned with beam and oxide pattern to yield poor anchor area for detector magnet after oxide release



C. Oxide detector magnet anchor pattern is reduced in diameter to allow larger misalignments between oxide, magnet, and beam patterns. If defects are present in central magnet/silicon anchor ring, detector magnet might still peel off during sacrificial oxide etching.



D. Oxide detector magnet anchor pattern is reduced in diameter and central oxide disk removed to yield larger anchor area for detector. Anchor area is impervious to HF oxide etching.



Key:

	<i>silicon</i>		<i>oxide</i>
	<i>plated magnet</i>		<i>photoresist</i>
	<i>seed layer</i>		

We expose the wafer using **Mask 3** using the GCA DSW 5X stepper at MDL, although previously we have used a GCA 4800 10X stepper at Integrated Micromachines®, in collaboration with Weilong Tang of that company. On this single mask plate, I had designed six oxide definition patterns, three for use with 10X, and three for use with 5X steppers. Thus there are three distinct patterns, each with different dimensions for the rings to allow for fine tuning of the process and coping with the failure modes mentioned above. We simply cover up the unused patterns, and program the stepper to shift its origin to the center of the desired mask pattern.

4.4.D. Magnet Patterning and Electrodeposition

Electrodeposition of specifically patterned magnets and incorporating them into mechanical oscillator structures constitutes the core of our microfabrication process. Electrodeposition provides a proven and controllable method for creating various ferromagnetic alloys in lithographically defined molds on a substrate. The ability to deposit films of reasonably high quality in terms of porosity and crystallinity, often approaching that of foundry-synthesized metals, in thicknesses ranging from ~ 100 nm to ~ 100 μm , allows considerable flexibility in current and future designs for BOOMERANG structures. We can readily control alloy compositions through bath salt and additive concentrations and through deposition conditions, even allowing testing of various alloys on a single substrate wafer.

This electrochemical process of magnet deposition is highly sensitive to specific chemical, electric field and conduction, fluid and gas flow and substrate factors. Every electrodeposition process must balance and optimize the following film properties: composition, deposition rate, internal stress, substrate-film adhesion, nm-scale roughness

and μm -scale morphology, magnetostriction, and sometimes interfacial film-substrate stress. We control film composition mainly through bath chemical concentrations, and to a lesser extent deposition voltage, current, and pH. The reader should refer to the patent of Castellani et al. [8] for more information on optimizing electrodeposition processes.

First and foremost, we seek to maximize the saturation magnetization of the magnet films so as to maximize sensitivity for a given detector geometry. We consider other properties of the magnets, such as permeability and coercivity as unimportant for our current BOOMERANG designs since they have no direct effect on sensitivity or homogeneity. Also, since we plan to operate in static magnetic fields above the saturation field of our detector and ring magnets, these properties will not contribute to eddy-current or hysteresis damping of the mechanical motion. Since eddy-current damping will also depend on the electrical conductivity of the detector and ring magnets, we seek to electrodeposit films with either low conductivity, or with geometric patterning to break up current paths.

The main practical barrier to high saturation magnet deposition is that of excessive internal stress leading to magnet delamination. The use of iron as an alloy component produces alloys with the highest saturation magnetizations, but high ratios of iron usually correlate with high stress. Iron has the further disadvantage that it corrodes very easily. Alloys of cobalt and iron have relatively poor corrosion resistance, but can produce a saturation magnetization of up to $2.6 \text{ T}/\mu_0$ [9]. Alloys rich in nickel give the highest corrosion resistance and the lowest stress, but have the lowest saturation magnetizations, typically $\sim 1 \text{ T}/\mu_0$ [10]. 20/80 Fe:Ni, or “permalloy,” is the most widely used and developed of these materials, has a magnetostriction value of zero, and has very

low stress and excellent corrosion resistance. CoNiFe alloys seemingly present the best compromise in that they have good corrosion resistance, M_s of up to $2.1 \text{ T}/\mu_0$, and acceptable stress. For ease and certainty of manufacture in our device trial runs, we have plated either 20/80 Fe:Ni (permalloy) [8], with $M_s = 1.0 \text{ T}/\mu_0$, or 50/50 Fe:Ni, with $M_s = 1.5 \text{ T}/\mu_0$. We continue to investigate CoNiFe alloys as superior candidates for future devices [11]. Table 4.4.1 shows typical bath mixtures, deposition conditions, and film properties for NiFe and CoNiFe alloys that we have plated. Additional plating conditions were that the pH was maintained at 2.6 ± 0.1 , and the deposition rates were typically $0.03 - 0.05 \mu\text{m}/\text{min}$ for these baths. For the CoNiFe baths, the plating current was between 30 and 40 mA for $\sim 1 \text{ cm}^2$ exposed plating area.

Table 4.4.1: NiFe and CoNiFe Alloy Electrodeposition**Conditions and Film Properties.** Emily Wesseling in the

Micromagnetics group at JPL measured the B vs. H loops for the plated films using a vibrating sample magnetometer. The stated percent compositions of the plated films come from energy dispersive (X-ray) spectroscopy (EDS) analysis in the SEM at MDL. We measured film thicknesses using profilometry (alpha step) at MDL.

NiFe Process Parameters		Analysis		
Fe (g/L)	Current (mA)	Thickness (μm)	Composition (wt. %Ni/Fe)	Magnetic Saturation (T/μ ₀)
5	100	3.52	49/51	1.59
15	80	3.09	38.2/61.8	1.76 or 1.81
15	50	6.75	61.3/38.7	1.41 or 1.42

CoNiFe bath-run number	Thickness (μm)	Composition (wt.% Co/Ni/Fe)	Magnetic Saturation (T/μ ₀)
K1-1	16.3	34.1/11.3/51	2.04
K1-2	5.3	37.5/10.4/52.1	2.06
K2-1	6.7 to 7.5	47.3/12.6/37.4	2.06 to 1.84
K2-2	4	47.6/12.6/39.2	1.92
K2-3	1.8	53.1/9.9/37	1.98

Components				
	NiSO ₄ ·6H ₂ O (g)	CoSO ₄ ·6H ₂ O (g)	FeSO ₄ ·6H ₂ O (g)	H ₂ O (L)
K1 bath	210.26	65.28	77.81	3.5
K2 bath	210.26	77.81	65.28	3.7

For both CoNiFe baths: H₃BO₄ = 98.9 g, Sodium Saccharin = 4.0 g, NH₄Cl = 64.14 g.

As mentioned in section 4.4.C above, we require an alignment tolerance of ~ 3 μm between the oxide sacrificial layer and the magnet deposition steps. We achieve this by using only masks defined by high-resolution optical or electron-beam lithography with

< 1 μm feature tolerance over the entire mask. We align these masks to the substrate wafer and expose patterns using the GCA DSW stepper. Sub-micron errors in alignment of the mask to the stepper optics, or the stepper to the substrate wafer are possible, but can be time-consuming to achieve. Thus our design allows for the slightly looser tolerance in the interest of efficiency and high yield.

Several factors limit definition of the photoresist mold. Design limitations on field homogeneity require that the gap be smaller than approximately 2 μm between the detector and ring magnets, although magnet thickness plays a part as well. The maximum aspect ratio for the photoresist mold obtained by conventional lithography is approximately 10:1, so that the walls separating the detector and ring magnets are limited to $\sim 10 \mu\text{m}$ in height. Through careful optimization of lithography conditions – light exposure time, chemical development time, and pre-exposure photoresist bake time and temperature - we have been able to achieve walls as tall as 15 μm and 1 – 1.5 μm thick (see Appendix B for details). Part of this success comes from soaking the photoresist in chlorobenzene prior to exposure to desensitize the photoresist closer to the surface, allowing a more uniform reaction to light exposure through the thickness of the photoresist. We have found substantial irreparable focusing errors in older GCA steppers used at Integrated Micromachines, and use of the GCA DSW 5X stepper at MDL working at 350 nm wavelength provides the best resolution. The failure mode in this lithography is that of over- or under-exposure of the photoresist possibly combined with over- or under-development. This results in a shorter photoresist wall to separate the detector and ring magnets or insufficient photoresist removal at the wafer surface after development. Due to exposure and development variations over a wafer, the yield for

this step has been as low as 20%, but has recently reached $\sim 90\%$, for 12 μm -tall photoresist walls using MDL's equipment [12]. Monitoring of the device structures and yield at this step should be done with optical and/or scanning-electron microscopy.

I show the details of this photolithography process in step 17 of Appendix B. I mention the reasons behind a few process details. After spin coating the wafer with this thick ($\sim 12 \mu\text{m}$) layer of photoresist, we use baking in a convection oven to drive off solvents. This also removes water from the photoresist, which deactivates its exposure properties. Letting the wafer stand overnight allows the photoresist to rehydrate and reactivate. After exposure with the magnet mold mask (**Mask 4**), the deepest photoresist (nearest the wafer surface) may be underexposed, causing residue after development that impedes magnet adhesion. Exposure of the wafer again with **Mask 3**, used for definition of the magnet anchor rings in the oxide sacrificial layer, allows further exposure of the photoresist in the critical regions of magnet adhesion without exposing the magnet mold photoresist walls.

Once we define the photoresist molds on the wafer, we electrodeposit 8-12 μm of magnet alloy such that the photoresist mold is nearly “full” with magnetic material, but the magnets do not bridge over the top of the photoresist wall. We should also monitor this step with optical and/or scanning-electron microscopy before proceeding. Relative to the optimum size cylindrical detector magnet of 20 μm radius and 18 μm height, detector magnets 25 μm in radius and 10 μm , 8 μm , or 6 μm in height are only 17%, 28%, or 44% less sensitive to magnetic moments, respectively, while allowing much easier fabrication.

After optimizing a given electrodeposition process, we have observed device yields for the plating step of close to 100%. This yield may be degraded by poor

adhesion of the plated magnets due to bath or surface contamination, or residual photoresist covering the seed layer.

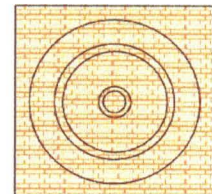
After magnet deposition, we ion mill away the plating seed layer that was deposited over the oxide sacrificial layer and that lies in the gap between the detector and ring magnets. After removal of the photoresist (detector/ring gap) and oxide (ring/beam gap) sacrificial layers, this seed layer section would bridge the detector/ring gap and prevent free vibration of the magnet-on-beam oscillator. The ion mill bombards a wafer with a beam of chemically neutral Ar^+ ions accelerated by a uniform electric field to ablate material away. This beam covers the entire area of the wafer and removes material roughly evenly across the wafer. During milling, the wafer chuck is water cooled to dissipate heating from the ion bombardment, and is rotated at about 2 RPM to spatially homogenize the beam's effects over the wafer. The operator must take care to use a beam current and voltage such that excessive heating does not damage the devices. For a given beam acceleration voltage, different materials etch at different rates. Using our milling conditions of 250 V beam voltage and $0.14 \text{ mA} / \text{cm}^2$ current density, milling rates range from 40 \AA/min for SiO_2 , 60 \AA/min for Cr or permalloy, up to 140 \AA/min for Au. Ion milling is a purely directional, momentum-transfer process, such that only material in the line of sight of the beam is ablated away. The beam must travel through the length of the detector/ring gap and the actual beam direction relative to the chuck is not precisely known, so in order to insure that the seed layer is completely removed we choose several angles of the wafer chuck (usually three to five angles) within 2° of perpendicular to the beam, and etch at each angle for the time it takes to remove the

entire seed layer (15 - 20 min). Figure 4.4.5 shows the process for the photolithography, magnet deposition, and ion milling.

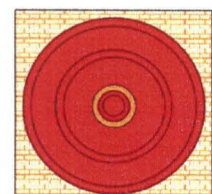
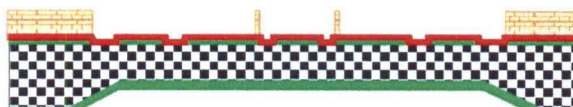
Figure 4.4.5: Magnet Lithography and Electrodeposition.

Note: individual die cross-section, dimensions not to scale

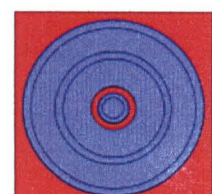
1) Spin PR frontside.



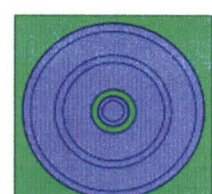
2) Mask 4: Magnet Mold
Expose and develop PR.



3) Deposit permalloy magnets, strip PR.



4) Ion mill seed layer.



Key:

	<i>silicon</i>		<i>seed layer</i>
	<i>plated magnet</i>		<i>photoresist</i>
	<i>oxide</i>		

Frontside Plan Views

A more predictable, although time-consuming, method of seed layer removal involves two steps of seed layer patterning and deposition. We would remove the original Cr/Au seed layer in the region of the detector/ring gap by patterning photoresist in the shape of the detector/ring gap and etching the seed layer, then depositing and patterning an easily wet-etched seed layer, such as titanium, in the place of the etched Cr/Au seed layer. The Ti acts only to provide electrical conductivity between the Cr/Au

under the detector magnet and the Cr/Au under the ring magnet, which provide much better adhesion and corrosion resistance than the Ti. When the devices are ready for final release, this Ti bridging layer will be rapidly removed in the HF solution used to etch away the oxide sacrificial layer, while the magnets and Cr/Au seed layer are unaffected. The cost of this process is that it involves one or two additional lithography steps, and requires alignment tolerance of $\sim 1 \mu\text{m}$ to accurately overlap this Ti layer with the patterned Cr/Au layer.

4.4.E. Beam and Buttress Definition

We have developed a novel method of defining few-micron-thick silicon oscillator beams using deep reactive-ion etching (DRIE) and multiple lithography masking steps to selectively remove material from a bulk silicon wafer substrate. This method allows considerable flexibility in the design of oscillator structures with magnets or other MEMS elements defined on the opposite side of the wafer from the DRIE etching. We have $\lesssim 0.5 \mu\text{m}$ -resolution control over all beam dimensions, as well as incorporation of additional structure, such as our stress buttress. We may also implement post-process or even post-testing adjustment of beam thickness using regular RIE or DRIE etching. A further advantage lies in the use of standard single-crystal silicon wafers as substrates, which should allow low mechanical dissipation and are more convenient to obtain than silicon-on-insulator (SOI) wafers. Use of SOI wafers, boron-doped silicon wafers, or surface-deposited silicon nitride to define oscillator structures may also provide excellent pathways to building BOOMERANG detectors, but sacrifice flexibility and agility of design, and/or mechanical dissipation quality. One possible disadvantage of our DRIE process is that sub-micron non-uniformity in beam thickness

and roughness resulting from this deep etching may cause increases in oscillator damping relative to more perfectly planar beams. We are currently studying this effect as well as steps that might be taken to reduce it.

We define these structures by first patterning two layers of masking material onto the backside of the wafer, one for the oscillator beam and one for the buttress. We then etch the profile of the beam into the backside surface of the wafer, strip the beam masking layer, and then etch the beam and buttress profile together. Due to the sidewall sensitivity of DRIE, the beam profile is maintained through this second etch step. After this second etch step, the beam and buttress are left free standing with open holes on either side of the beam. By doing two steps of lithography, followed by two steps of etching, we save substantial effort and produce more regular and certain structures. I detail these processes and their motivations in the following subsections.

1. Photolithography

We begin our process of backside beam definition by protecting the already-defined magnet structures by spinning photoresist to cover the entire frontside of the wafer. As a result of the thermal oxidation described in section 4.4.c, the backside of the wafer has a $\sim 1 \mu\text{m}$ oxide layer on it. We will use this oxide as a masking layer that resists DRIE. Through detailed testing with various thicknesses of photoresist, oxide, and silicon substrates, we found the etch-rate selectivity of Si to SiO_2 to be $\sim 400:1$, and of Si to photoresist to be $\sim 30:1$. Thus our $\sim 1 \mu\text{m}$ of photoresist works well as a masking layer for the short DRIE through $\sim 5 \mu\text{m}$ of silicon to define the beam, and $\sim 1 \mu\text{m}$ of SiO_2 works for DRIE through $\sim 100 \mu\text{m}$ of silicon. These selectivities depend heavily on the particular DRIE recipe parameters. From a selectivity standpoint, it would be

possible to use less than 1 μm of photoresist for the initial beam etching step, but we have found that chemical changes to the photoresist during DRIE tend to make it difficult to remove. Thus we use a much thicker ($\sim 10 \mu\text{m}$) layer of photoresist so that only its surface becomes hardened or crosslinked, and it remains easy to strip. It is also possible to use PECVD oxide as the inner masking layer, but this process has not yet been characterized as regards etch selectivity.

We begin the patterning process by spinning photoresist over the oxide on the backside of the wafer. Using **Mask 5**, we expose this photoresist using the GCA DSW stepper, then develop it to leave the pattern of the buttress inside an open 400 X 400 μm square. We then etch the oxide with BOE to pattern the oxide, and strip the photoresist. We now have the oxide patterned as a DRIE masking layer for the stress buttress.

We then spin thick photoresist ($\sim 10 \mu\text{m}$) over the backside to define the beam pattern. We expose the photoresist using **Mask 6**, and develop it to leave the beam pattern overlapping the oxide buttress pattern. Figure 4.4.6 shows the lithography steps involved in producing these overlapping DRIE masking layers.

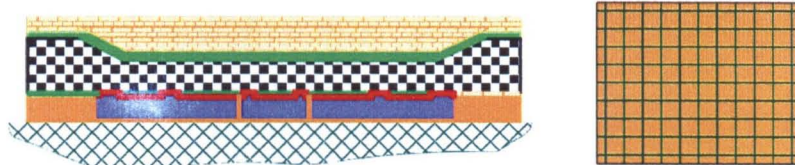
In order for samples to be held by the electrostatic chuck in the DRIE chamber, they must have a smooth and flat bottom surface opposite the DRIE processing surface. We must therefore mount the protected frontside of the wafer to a planar but unpolished silicon dummy wafer with dental wax (melting point = 70 $^{\circ}\text{C}$) using a standard MDL procedure. All wax and residue must be removed from the bottom of the dummy wafer after mounting so that residues do not vaporize and cause the wafer to jump off the chuck during DRIE.

If we were to simply define the stress buttress pattern with photoresist, then DRIE etch, then spin photoresist again, the photoresist would tend to pile up and become non-uniform in the region of the 45 μm squares etched out to define the buttress. This would likely make pattern definition more difficult and less precise. Furthermore, defining both masking layers first, then doing both DRIE steps in quick succession, allows for economy of scheduling when dealing with the high-demand DRIE machine and operator.

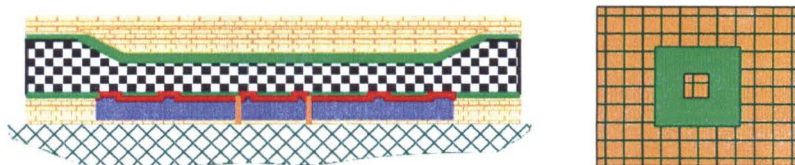
Figure 4.4.6: Photolithography for Beam/Buttress DRIE.

Note: individual die cross-section, dimensions not to scale

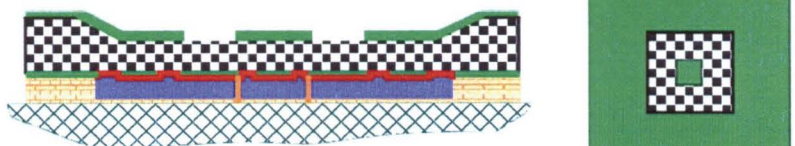
1) Spin PR both sides.
Mount wafer on protect wafer.



2) Mask 5:
Buttress Pattern
Expose/develop PR on backside.



3) Etch oxide (BOE).
Strip PR.



4) Spin PR,
Mask 6:
Beam Pattern
Expose/develop PR on backside.



Key:

silicon

plated magnet

oxide

protect wafer

PR over oxide

photoresist

Backside Plan Views

seed layer

2. **DRIE Etching**

Once we define both the beam and buttress masking layers, we etch the wafer to define the beam, strip the photoresist masking layer, and then etch the buttress and beam pattern to break through the wafer. Our goal for the beam thickness is 2 – 4 μm and depends on the following: 1) magnet thickness and magnetization (negative magnetic force constant), 2) beam width, 3) buttress thickness (mass), and 4) application of capacitive forces to further reduce the effective force constant.

Over an entire wafer, DRIE produces differences in etch rates of 5 - 10%, such that after a 50 μm etch to break through the wafer, we observe beam thickness variations of as much as 5 μm over the wafer. Almost all of the 5 - 10% etch-rate variation is between the center of the wafer, which etches more slowly, and the edges of the wafer. Also, the etch rate tends to be slightly higher ($\sim 1\%$) on the side of the DRIE chamber closest to the turbopump, relative to the opposite side. In order to fabricate beams of the correct thickness, we first define beams that are 6 – 12 μm thick so that etch-rate variations do not cause complete removal of any of the beams. Any beams that are too thick may be thinned at the end of the etch process, even after dicing of the wafer and/or testing. Thus our first DRIE step consists of etching the beam pattern on the wafer for 2 min, assuming an etch rate of 3.3 (± 0.2) $\mu\text{m}/\text{min}$. As changes are made to specific hardware or software in the STS DRIE machine, etch rates may change and must be monitored through all process steps.

Since the photoresist and oxide masking layers are 3 – 10 μm thick, we make comparative profilometry (α -step) measurements before and after beam etching and at several locations on the wafer to ensure that we have attained the correct beam-etch

depth. We then remove the photoresist masking layer to expose the SiO₂ buttress-masking layer. Under normal circumstances, the photoresist stripper will not harm the wax that mounts the device wafer to the dummy wafer, so demounting and remounting are not necessary. If a thin layer of photoresist was used for the masking layer, then soaking the wafer in photoresist stripper may leave cross-linked photoresist residue behind. Any residue may be removed using high-power (up to 250 W) O₂ plasma etching, or “ashing,” which removes organics while leaving all other materials unharmed. High-power ashing heats the wafer, so we can watch for melting of the wafer-mounting wax during ashing and stop to let the chamber and wafer cool, or just stop at 8-10 min intervals to allow for cooling, and observe the photoresist residue under the microscope. If the mounting wax has melted, then repositioning the wafers and cleaning the bottom surface may be necessary.

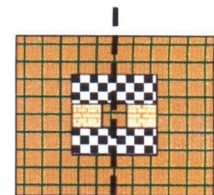
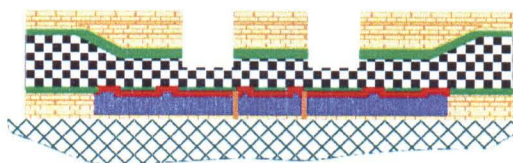
Once we have removed the photoresist masking layer, we DRIE etch to remove the material in the pattern of the buttress mask, and punch through the wafer on either side of the beam, leaving the beam and buttress structure. Figure 4.4.7 shows this process. In order to take into account variations in etch rate using DRIE, as well as substrate wafer thickness variations, we first do a slightly shorter etch than that predicted to achieve break through of the dies to the oxide sacrificial layer on the frontside that separates the magnet from the silicon wafer. In this way, this frontside oxide sacrificial layer also acts as an etch stop. As in the beam-etch step, we make comparative profilometry (α -step) measurements before and after this first etch and at several locations on the wafer to measure the etch depths. For a 50 μm substrate thickness, and an initial beam etch of 6 μm , the first etch should be \sim 12 min to yield a total etch depth

of approximately $(12 \text{ min} * 3.3 \mu\text{m/min}) + 6 \mu\text{m} = 46 \mu\text{m}$. After measuring the actual etch depths across the wafer, we can decide how much more to etch. At this point, we also check in the microscope to see if any of the dies have been broken through to the frontside oxide layer. If we observe partial break through, or translucent silicon that is almost broken through, we can decide to continue etching the silicon using DRIE, or using regular SF_6 RIE, also termed “fluorine RIE,” which has a much slower, $\sim 0.4 \mu\text{m/min}$ etch rate. I discuss further benefits of using regular SF_6 RIE after DRIE at the end of the next section (4.4.F). Since dies of a given wafer may be etched at different rates, and thus may need different amounts of etching to complete, we may also want to dice the wafer and etch separate groups of dies to achieve the desired beam thickness.

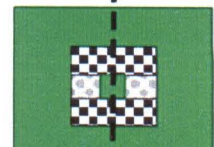
Figure 4.4.7: Beam/Buttress DRIE Process.

Note: individual die cross-section, dimensions not to scale

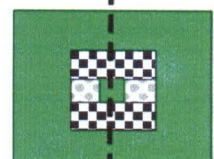
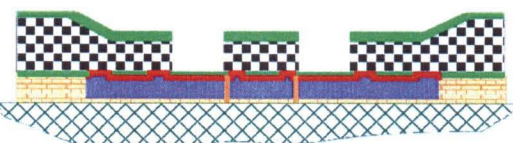
1) Etch (DRIE) silicon
6 - 10 μm to define oscillator beam.



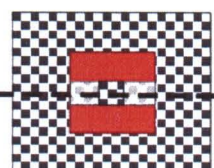
2) Strip PR to reveal oxide (buttress) masking layer.



3) DRIE silicon
40 - 45 μm to define buttress and push down beam pattern.



4) Adjust beam thickness and clean silicon residue (pillars) using SF₆ RIE (not shown).



5) Demount protect wafer, strip PR, and immerse in BOE or 49% HF to remove oxide and release structure.

Backside Plan Views
(Dotted lines denote cross-section cut.)

silicon protect wafer

Key: plated magnet PR over oxide seed layer
 oxide photoresist beam surface

I make a final comment on DRIE here concerning recent process developments by Daniel E. Miller at MDL. In order to simplify patterning of wafer backsides using MDL's 5X stepper, Dan has started using 200 μm wafers as starting material. This appears to allow adequate definition of the oscillator suspension by DRIE through the 200 μm wafer thickness, while circumventing the KOH deep trench etching prior to magnet definition. In order to prevent breakage of these thinner wafers during

processing, Daniel has used Crystal Bond glue (thermally activated, acetone soluble) to mount these substrate wafers to robust 500 μm wafer frames.

4.4.F. Final Release

Two sacrificial layers must be removed from the final device to release the mechanical oscillator to vibrate freely. We dissolve the photoresist layer separating the detector and ring magnets using photoresist stripper, and we have assumed that this is sufficient to remove all residue. It may be useful to follow the stripper by immersion in warm acetone or methylene chloride, or etching in oxygen plasma (ashing). Complete removal of the oxide layer separating the ring magnet from the oscillator beam poses more of a challenge, and residual oxide or free silicon pieces in the etching solution may have prevented free oscillator movement in our recent fabrication attempts. We have used room temperature BOE and 49% HF etchants, each for different time periods, to remove this layer while leaving magnets and silicon substantially unharmed.

So far, we have used 60 μm -wide beams for our oscillators with a $\sim 1.5 \mu\text{m}$ -thick thermally grown oxide sacrificial layer. This arrangement requires etching through 30 μm of tough oxide from either side to free the beams. This means immersion of the devices in BOE or 49% HF for 5 hours or 15 minutes, respectively, to achieve beam release. Longer etching times may be necessary, as the stated etch times assume that the etching of the oxide occurs with constant etch rate, *i.e.*, that fresh etchant rapidly diffuses into the magnet/beam gap to continue the etch process. Long-time etching with these harsh solvents also causes damage to the magnets and silicon beams. Etch rates for these solvents are 800 - 1200 $\text{\AA}/\text{min}$ for 10:1 or 7:1 BOE solutions, respectively, and 2.3 $\mu\text{m}/\text{min}$ for 49% HF [13].

I roughly tested the two solvents to determine maximum etch times, below which the magnets and beams appear undamaged under a microscope. I immersed several completed dies in each solvent for various total times. Using 7:1 BOE solution (7 parts NH₄F, 1 part HF), I found that etch times over 16 hours caused removal of most of the magnets and silicon beams, while etch times below 8 hours consistently left them apparently unharmed. For concentrated HF solution, etch times of more than 2 hours caused some damage, while etch times below 1 hour caused no apparent damage. Given the theoretical etch times necessary, the HF has a better etch rate relative to its rate of damage to the device. Of course, these are extremely dangerous solvents, especially the 49% HF, and must be handled with extreme care. In order to counteract stiction, as discussed in section 4.4.C, critical point drying may be used for solvent removal after etching.

During the DRIE process, tall needles or islands of silicon may form when the fluoropolymer protection layer does not completely etch away on a given etch cycle, and continues to acquire protection layer on a small region or dot of silicon on subsequent cycles. This effect is not always observed when doing DRIE, and may be related to contamination in the chamber or on the surface of the wafer. These islands release from the oxide (sacrificial layer) substrate when the oxide is wet etched away, and they may clog the detector/ring or ring/beam gaps and prevent free vibration of the oscillator after release. By implementing more than one step of oxide etching, followed by rinsing and use of fresh etchant, it may be possible to remove these islands from the etching solution before they have access to the exposed critical gaps in the BOOMERANG oscillator. The first step of etching would be only several minutes long and would be sufficient to

release the silicon islands before the ring-magnet/beam gap is exposed. This short etch may be repeated to remove additional silicon contaminants from the etching solution. A more robust method of island removal prior to sacrificial layer etching would be to blast away these thin islands with a few minutes of regular SF₆ RIE at ~ 100 W. This also thins the beams slightly, but also results in a cleaner beam surface than that left by DRIE.

Use of other sacrificial layer materials or beam geometries may be used to decrease the layer removal time or allow less chemically harsh etching in order to better preserve magnet and beam integrity. Use of PECVD oxide as the sacrificial layer would allow much faster etching due to its more porous nature. Etch rates are on the order of ten times faster for this material, and would allow complete sacrificial layer removal in considerably less time. We are currently testing this approach to sacrificial layer deposition and removal. Another possibility is to use hardbaked photoresist (cross-linked with > 120°C heat) or electrodeposited metal (*e.g.*, copper) for this sacrificial layer. These materials might be removed with less harsh solvents than oxide. The simplest approach to alleviating this problem is to incorporate narrower beams or beams with etch holes in them to allow the solvent to penetrate more quickly. We currently have lithography masks available to fabricate monolithic beams 20, 40, or 60 μm wide. We have been defining 60 μm -wide beams to provide torsional stiffness to counteract magnetic torques, but our observations of functioning oscillator beams with narrower aspect ratios at the 3 mm scale suggest that 40 or possibly 20 μm -wide beams will be sufficient. Our future fabrication runs will use 20 μm -wide beams, thus allowing softer elastic spring constants for a given thickness, and oxide-release etch times 1/3 as long as previous device attempts.

4.4.G. Concluding Remarks on Processing

It is essential that micromachinists carefully and rigorously characterize a device wafer at every step of a microfabrication process so that errors may be perceived when they occur and corrected if possible, or the process terminated before substantial work is wasted. Accurate characterization, followed by informed in-process decision making and process design feedback, is probably the most difficult and valuable part of successful micromachining – it is almost never wasted time. Common characterization methods include, in roughly ascending order of simplicity: visual inspection, optical microscopy, profilometry, ellipsometry, scanning electron microscopy (SEM) and X-ray spectrometry, atomic force microscopy (AFM), and magnetometry [5].

4.5 *Microfabrication Results and Testing of BOOMERANG Oscillators*

We have run through the entire microfabrication process as described, and have had promising device structure results. While approximately 20 oscillators out of 300 have passed visual signs of functionality, we have unsuccessfully attempted to observe oscillator resonances. The most likely candidate for the absence of resonances in apparently perfect oscillators is contamination due to etched pieces of silicon jamming into the oscillator gaps. I present our favorable results below as well as our efforts toward characterizing the BOOMERANG oscillators.

4.5.A Silicon Oscillator Beams Without Magnets

To verify that our mechanical suspension resonance frequency theory holds at the micron scale and to investigate dissipation, we have taken completed detector oscillators and removed the electrodeposited magnets. This leaves just the silicon oscillator suspension

with the stress buttress shown in figure 4.5.1. Using the apparatus described below, I have measured the oscillator properties shown in the caption for figure 4.5.1, and the frequencies and dimensions agree with theoretical calculations to within 5%, as shown in table 4.5.1.

4.5.B Device Structures

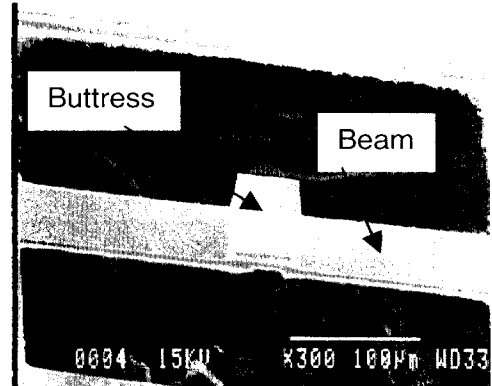
Figure 4.5.2 shows top and bottom views of finished mechanical oscillators. Note

Table 4.5.1: Theoretical Oscillator Frequency Calculations.

These predictions of fundamental resonance frequencies for rectangular, centrally loaded, clamped silicon beams (see section 2.2.A) agree with experimental values to within 5%.

Width	Thickness	Beam Mass	E (Pa)	Length	Buttress Mass	v_h	k (N/m)
6.0E-05	5.9E-06	3.3E-10	1.9E+11	4.0E-04	3.7E-10	1.7E+05	530
6.0E-05	1.7E-06	9.4E-11	1.9E+11	4.0E-04	3.7E-10	2.9E+04	14

Figure 4.5.1: Silicon Beam and Buttress. The beam shown in this SEM picture and defined using DRIE has a resonance frequency of 166 kHz and measures $6.0 \pm 0.2 \mu\text{m}$ thick. We have measured several other oscillators with v_h between 24 and 166 kHz. The most suitable oscillator so far has $v_h = 27 \text{ kHz}$, $\tau_h = 7 \text{ ms}$ at 1 atm, and $\tau_h = 70 \text{ ms}$ at 50 mTorr pressure.



the mis-alignments present in parts A and B, which I show simply to present a more open view of the oscillator geometry. The detector/ring gap and ring slits are completely uncovered, indicating that we have successfully ion milled the seed layer away. Part C shows a polished cross-section taken by Weilong Tang at Integrated Micromachines by filling all voids with epoxy, cutting through the wafer, then polishing it to the desired cross-section. In this cross-section, there appears to be no blocking of the mechanical oscillator suspension with materials that have been incompletely etched.

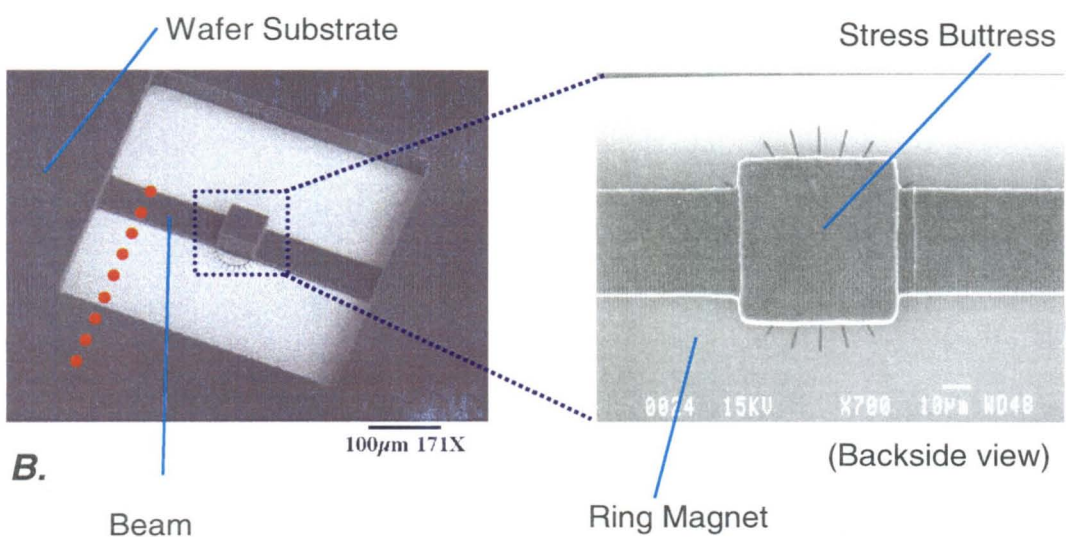
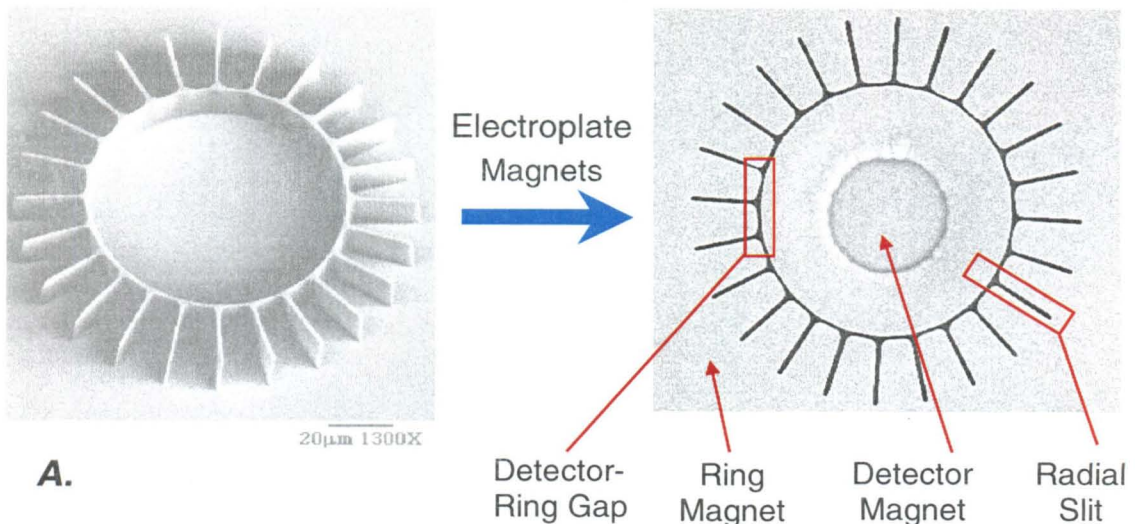


Figure 4.5.2: Microfabricated BOOMERANG Device Structures.

The left SEM picture in part A shows the photoresist mold used to deposit the BOOMERANG magnets into. The right optical micrograph shows the resulting magnet structures with design elements highlighted. Part B shows SEM pictures of the backside of a completed device wafer with DRIE-defined oscillator beam and stress buttress. The optical micrograph in part C shows a cross-section along the heavy dotted line shown in part B. This device was filled with epoxy and then cut and polished to look for obstruction in the gap between the beam and the ring magnet. This diagnostic showed no apparent residual material blocking the gap.

4.5.C MEMS Oscillator Testing Apparatus

As a simple method of measuring micro-oscillator resonances with our existing BOOMERANG spectrometer equipment, I built an apparatus to mount these oscillators on a movable stage under our tried-and-true fiber-optic interferometer. Figure 4.5.3 shows the complete testing apparatus using the familiar interferometer z-stage shown in figure 3.1.2 and an xy-stage to mount the samples.

Since these oscillators are quite small by naked-eye standards, various methods might be used to locate them under the FOI tip for measurement. One straightforward method would involve placing a small optical or IR camera near the FOI tip and pointing diagonally down toward the oscillator stage. With a suitable image readout, one could simply align the oscillator near the FOI tip visually. These cameras are commonly used for coarse alignments and cantilever/sample mounting in other force-microscopy methods [14].

Since this camera method would involve substantial development and some parts investment, I took a simpler path, using the response of the FOI fringe *visibility* to changes in the distance between the tip and sample. By placing the FOI tip outside the

distance where the visibility is optimized, and scanning the sample stage under the tip, the visibility changes dramatically when the FOI tip is over the ring magnet or oscillator beam and the Fabry-Perot cavity lengthens. If we scan the FOI tip to reside over the stress buttress, then the visibility then returns to its original value when the FOI tip was over the surrounding silicon wafer substrate. The inset to figure 4.5.3 depicts this alignment scheme. Once the FOI tip is above the buttress, shaking the sample stage with

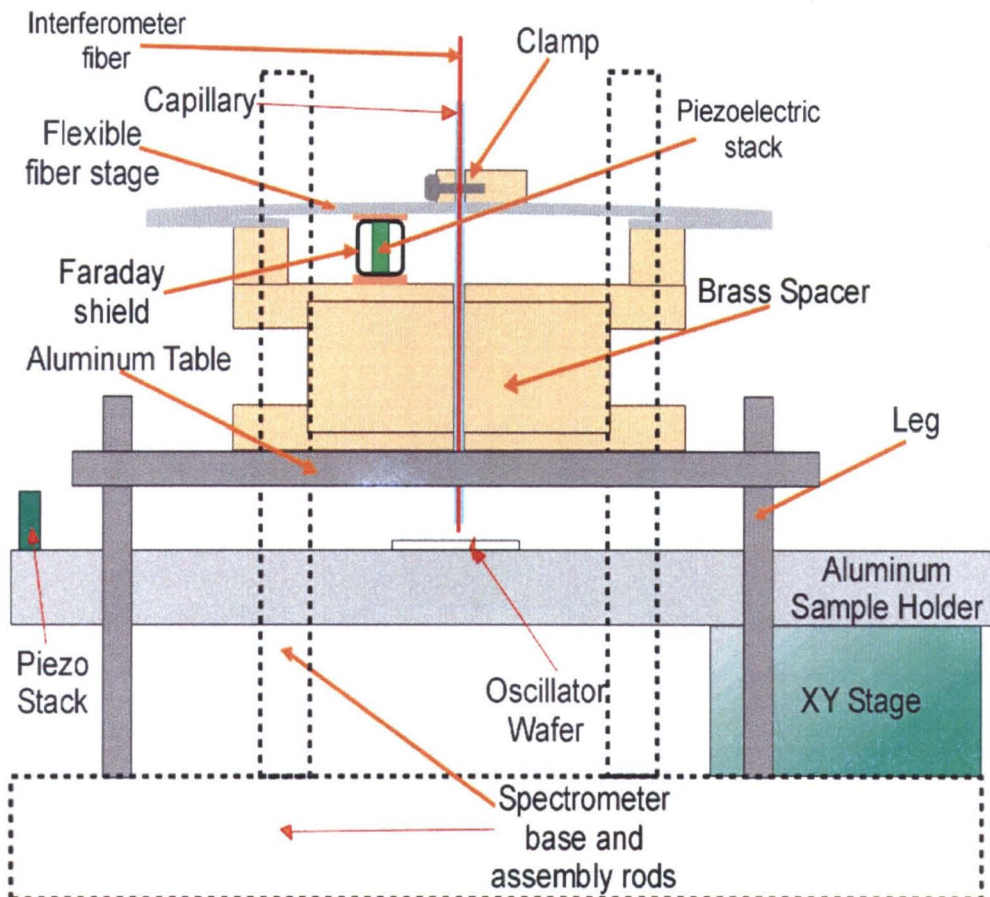


Figure 4.5.3: Cross Section of Micro-Oscillator Testing

Apparatus. Using the existing BOOMERANG prototype interferometer and positioning stage, this apparatus incorporates an xy stage to position the sample under the fiber tip. A second piezoelectric stack transducer driven by a high-voltage amplifier and function generator provides vibrational excitation to the micro-oscillators. The interferometer stage sits on an aluminum table with steel bolts for adjustable-height legs.

the amplifier-driven piezoelectric stack allows scanning over excitation frequencies up to 250 kHz, and we may trace out the oscillator resonances. This method may be complicated by oscillators with different heights for the stress buttress and silicon wafer substrate, but should still be feasible with sufficient operator finesse.

4.6 A Proposed Spectrometer Assembly

Here I describe general designs and forms for a prototype micron-scale BOOMERANG spectrometer. These designs lean toward a single-detector, portable *in-situ* device, but should apply easily to a parallel array of spectrometers. As discussed above in section 1.2.G, use of BOOMERANG as a high-throughput method of NMR chemical analysis is made possible by the parallel nature of device microfabrication. Assuming high-yield conditions are possible in fabrication processes, we may expect to fabricate many spectrometers on a single wafer, possibly with incorporated displacement

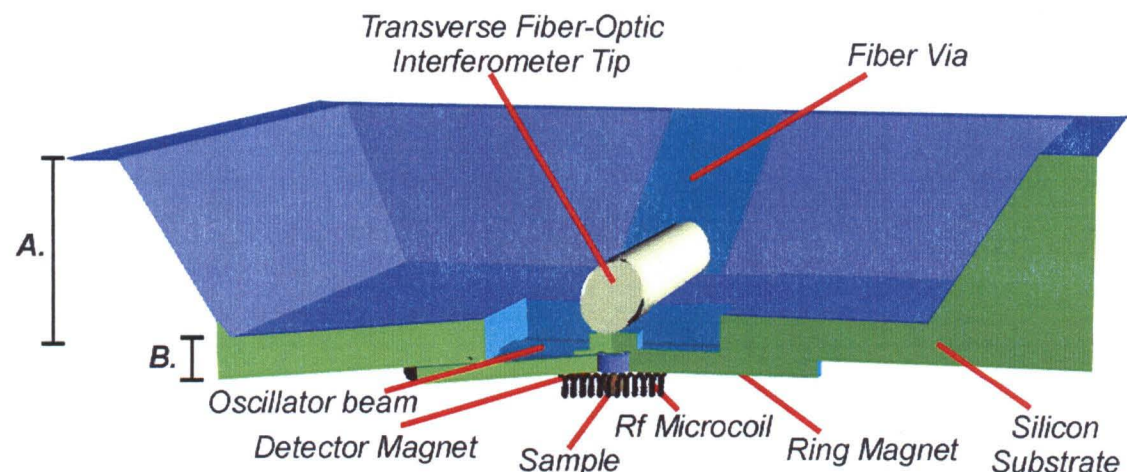


Figure 4.6.1: BOOMERANG Micro-Oscillator Detector. This diagram shows a single wafer die of the to-scale detector oscillator with TFOI tip inserted through a hole or via in the silicon substrate. Measurement A. indicates the KOH trench etch depth (section 4.4.B). Measurement B. indicates the DRIE etch depth to define the oscillator beam.

sensors. For our oscillator magnet and beam designs outlined here, it is a simple matter to close-pack them to allow \sim 10,000 BOOMERANG detectors on a single 4 X 4 cm square chip, yielding a factor of 100 gain in sensitivity over a single detector. This assumes no detailed efforts toward optimization of packing density. Such an array of detectors would easily insert into a high-field cryomagnet bore to allow the highest sensitivity and resolution.

Once we have fabricated our micron-scale detector oscillator, we will incorporate the transverse fiber-optic interferometer (TFOI) as the displacement sensor. Figure 4.6.1 shows a single detector die with incorporated TFOI tip. This TFOI tip would mount to a piezoelectric stage mounted to the die substrate, and would likely take the form of a miniature piezo bimorph bending actuator [15, 16].

Using a suitable spacer plate (*e.g.*, a silicon wafer) with thickness twice the distance of the sample center to detector magnet surface ($2R_{max}$), we would sandwich together two of these dies, one with a fixed-detector-magnet oscillator, with the rf excitation probe (see figure 4.1.2) between them as shown in figure 4.6.2. We may either place this assembly between the poles of a large, variable-field electromagnet (Varian XL 100 NMR magnet), inside a superconducting cryomagnet, or between a pair of permanent magnet poles as shown in figure 4.6.2. We would also enclose this assembly in a suitable vacuum chamber, or make the oscillator die part of a small chamber that encloses only the detector oscillator and TFOI tip. Since the permanent magnet poles might exert destructive forces on the detector magnet during assembly, we will incorporate an adjustable yoke, also shown in figure 4.6.2, to bring the pole magnets together symmetrically.

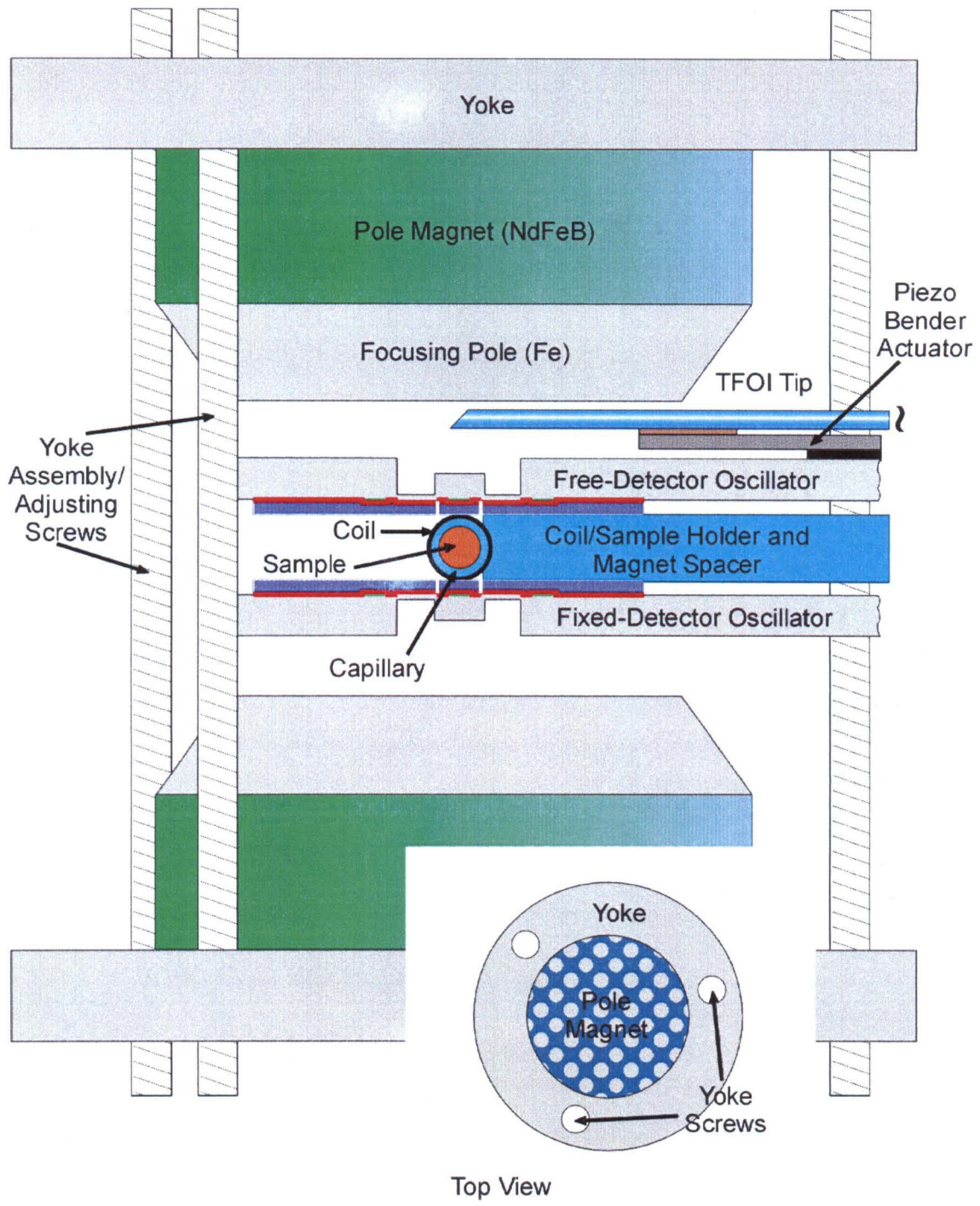


Figure 4.6.2: Cross Section of Micro-BOOMERANG

Spectrometer. Dimensions are not to scale in order to allow adequate depiction of all elements. We may scan the TFOI tip vertically using a piezoelectric bender actuator. We will assemble the permanent pole magnets using an adjustable yoke as shown, which also mounts the detector and rf excitation assembly.

References

1. Hoffman, W.P., H.T. Phan, and P.G. Wapner, *The far-reaching nature of microtube technology*. Mat. Res. Innovat., 1998. **2**: p. 87-96.
2. Wago, K., et al., *Low-temperature magnetic resonance force detection*. Journal of Vacuum Science & Technology B, 1996. **14**(2): p. 1197-1201.
3. Yannoni, C.S., et al., *Force Detection and Imaging in Magnetic Resonance*, in *Encyclopedia of Nuclear Magnetic Resonance*, D.M. Grant and R.K. Harris, Editors. 1996, John Wiley: New York.
4. Streckeisen, P., et al., *Instrumental aspects of magnetic resonance force microscopy*. Applied Physics a-Materials Science & Processing, 1998. **66**: p. S341-S344.
5. Madou, M.J., *Fundamentals of Microfabrication*. 1st ed. 1997, New York: CRC Press.
6. George, T., et al. *MEMS-based force-detected nuclear magnetic resonance spectrometer for in situ planetary exploration*. in *2001 IEEE Aerospace conference*. 2001. Big Sky, Montana.
7. Son, K.-A., *Personal Communication, Re: Resolution of contact aligner*. 2001.
8. Castellani, E.E., J.V. Powers, and L.T. Romankiw, *Nickel-iron (80:20) alloy thin film electroplating method and electrochemical treatment and plating apparatus*, U. S. Patent. 1978: USA.
9. Cullity, B.D., *Introduction to magnetic materials*. 1972, Reading, MA: Addison-Wesley.
10. Tebble, R.S. and D.J. Craik, *Magnetic Materials*. 1969, New York: Wiley-Interscience.
11. Osaka, T., et al., *A soft magnetic CoNiFe film with high saturation magnetic flux density and low coercivity*. Nature, 1998. **392**(6678): p. 796-798.
12. Miller, D.E., *Personal Communication, Re: Dimensions and yield for photoresist mold lithography*. 2002.
13. Williams, K.R. and R.S. Muller, *Etch rates for micromachining processing*. Journal of Microelectromechanical Systems, 1996. **5**(4): p. 256-269.
14. Son, K.-A., *Personal Communication, Re: IR camera for AFM assembly*. 2001.

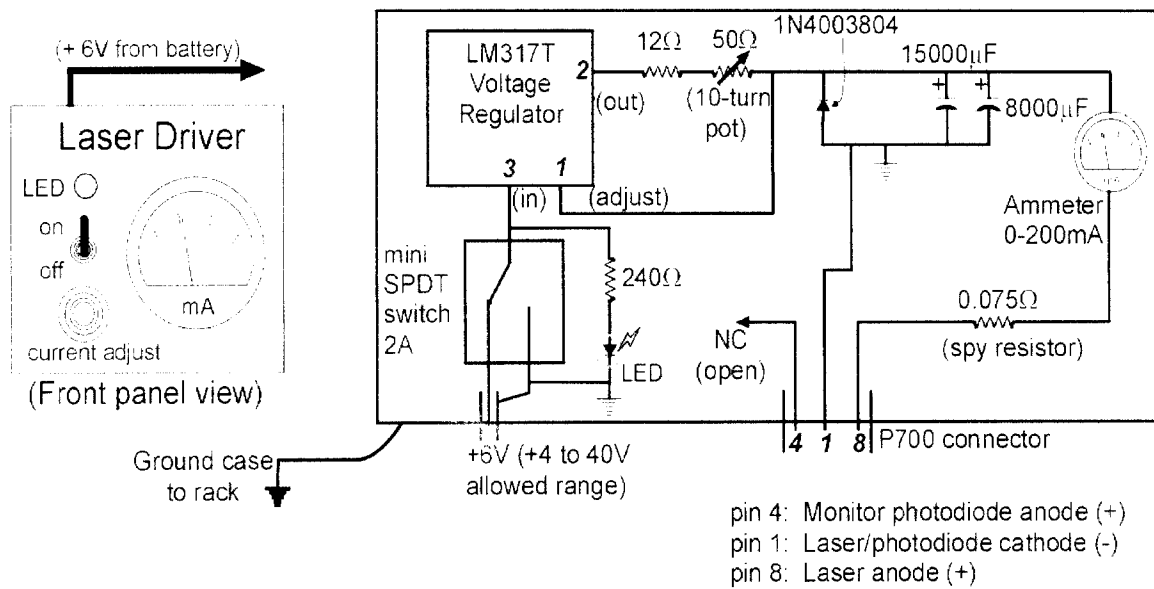
15. *Piezo Systems, Inc., www.piezo.com.* 2002, Cambridge, MA.
16. *Physik Instrumente Gmbh & Co, www.physikinstrumente.com.* 2002, Karlsruhe/Palmbach, Germany.

Appendix A: Additional Experimental Hardware Descriptions and Diagrams

A.1 Constant-Current Laser Driver

This circuit consists of a variable-voltage regulator (LM317T) wired as a constant current source. The circuit will output an adjustable 20 – 100 mA of current, and has a low-pass RC filter and diodes to protect the laser from current spikes. Figure A.1 shows the circuit diagram. See also section 3.1.D.

Figure A.1: Laser Driver Circuit.

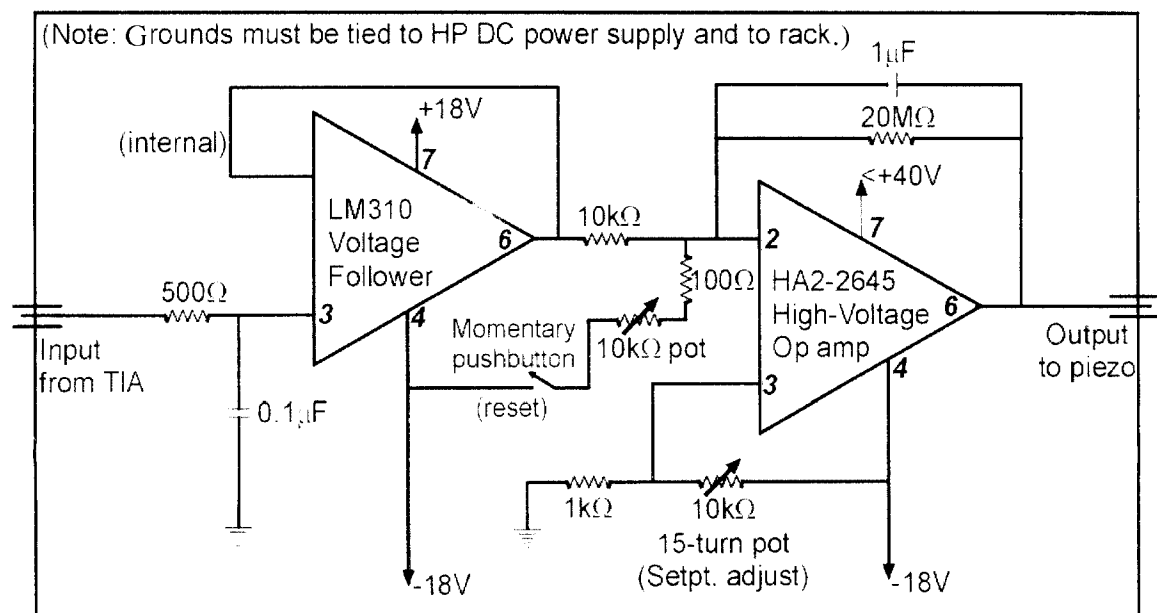
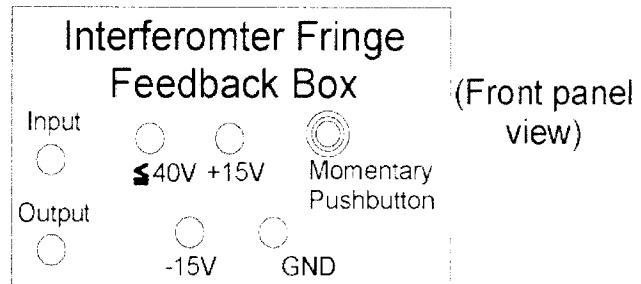


A.2 Interferometer Fringe Feedback Circuit

Figure A.2 shows our interferometer fringe feedback circuit. This device reads the signal from the TIA and outputs a feedback voltage to the piezoelectric stack actuator to maintain the fringe at its most sensitive position at frequencies below ~ 10 Hz. Both the laser driver and fringe feedback circuits consist of common and inexpensive

elements, and run on battery power to minimize noise from ac power sources coupling into the detection. See also section 3.1.D.

Figure A.2: Interferometer Fringe Feedback Circuit.

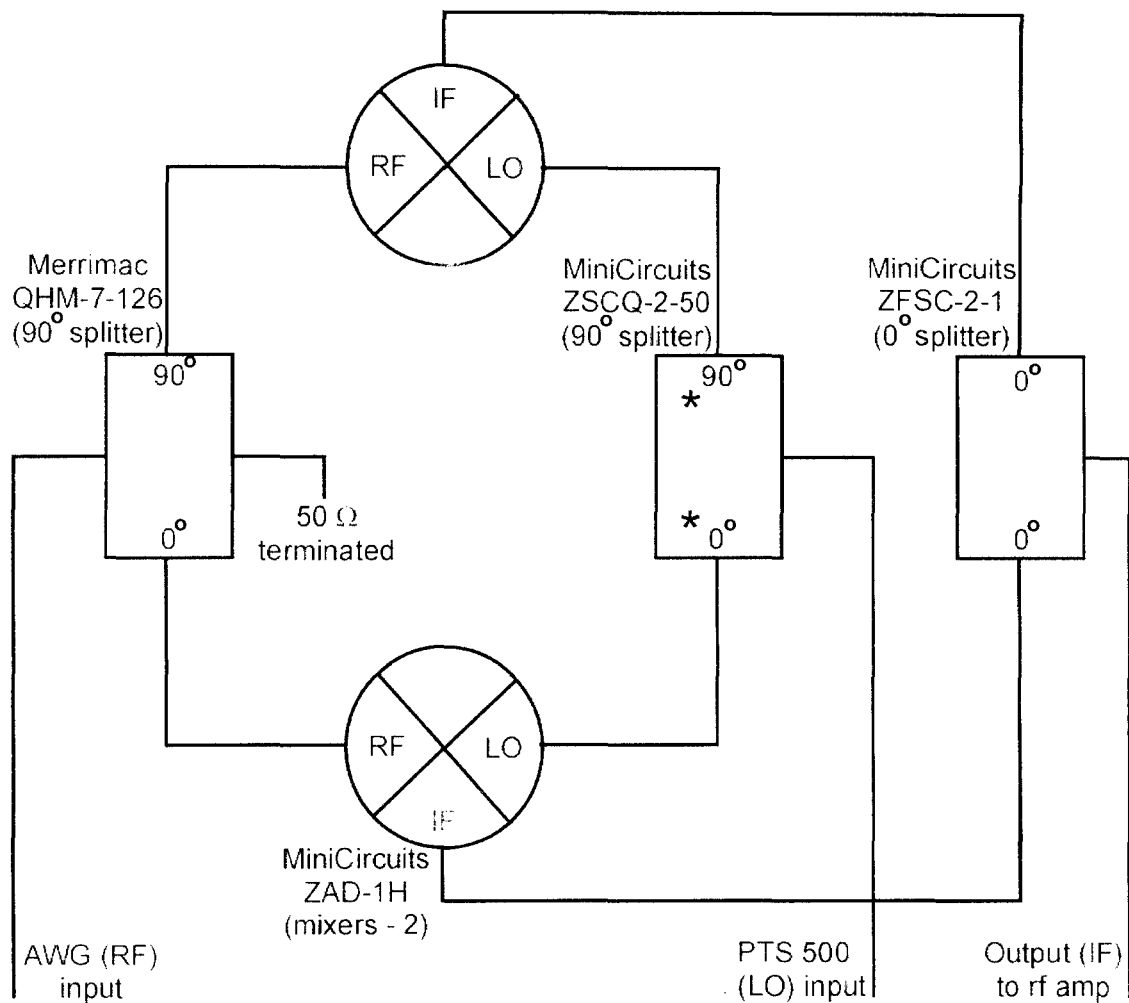


A.3 Single-Sideband Mixer

Figure A.3 diagrams our single-sideband mixer, built entirely from passive components. This circuit outputs frequencies at the “IF” port of dc – 100 MHz, whereas the “RF” and “LO” input ranges are limited to 1 – 50 MHz and 25 – 50 MHz, respectively. Using the configuration shown, only the lower sideband emerges from the output. By reversing the terminals on one of the 90° splitters (marked with *), one may

select the upper sideband. This circuit is enclosed in a shielded box and the external connections are made with BNC cables and bulkhead connectors. See also section 3.1.E.

Figure A.3: Single-Sideband Mixer.

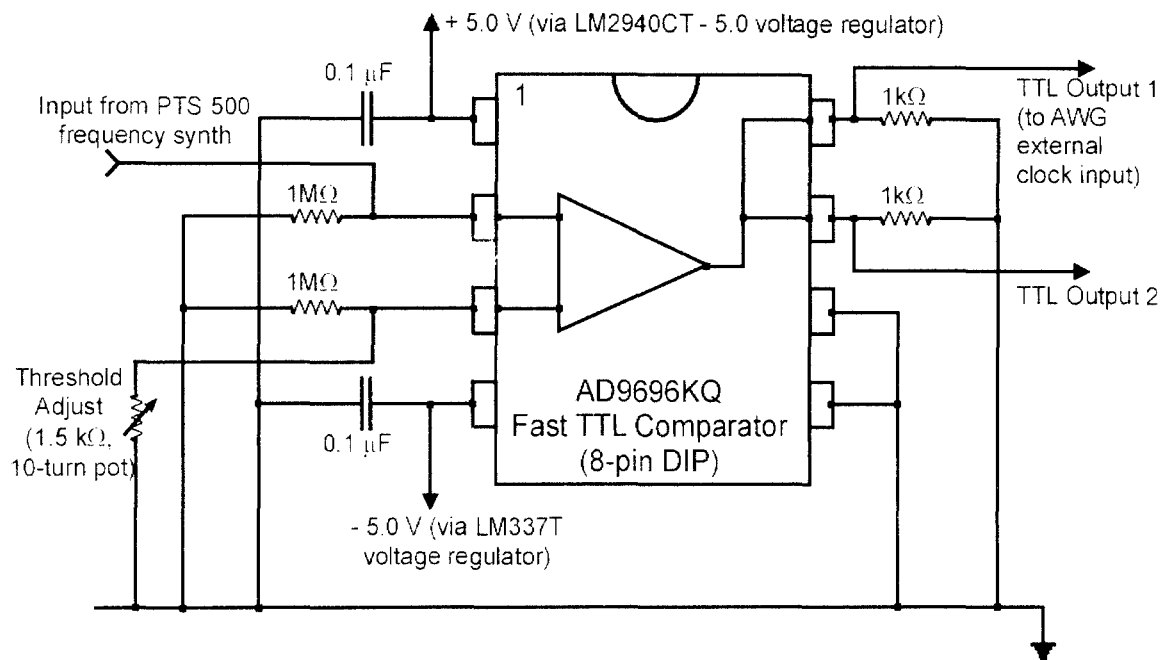


A.4 TTL Comparator Circuit for AWG External Clock

This fast comparator circuit takes a bipolar sinewave as an input and generates a TTL (0/+5V, unipolar) square wave of up to 50 MHz. We use this circuit as a stable external clock source for the AWG-502 D/A board. This circuit is powered by the auto batteries via voltage regulators. This circuit is enclosed in a shielded box and all external

connections are made using BNC cables and bulkhead connectors. See also section 3.1.E.

Figure A.4: External Clock Circuit - Fast TTL Comparator.



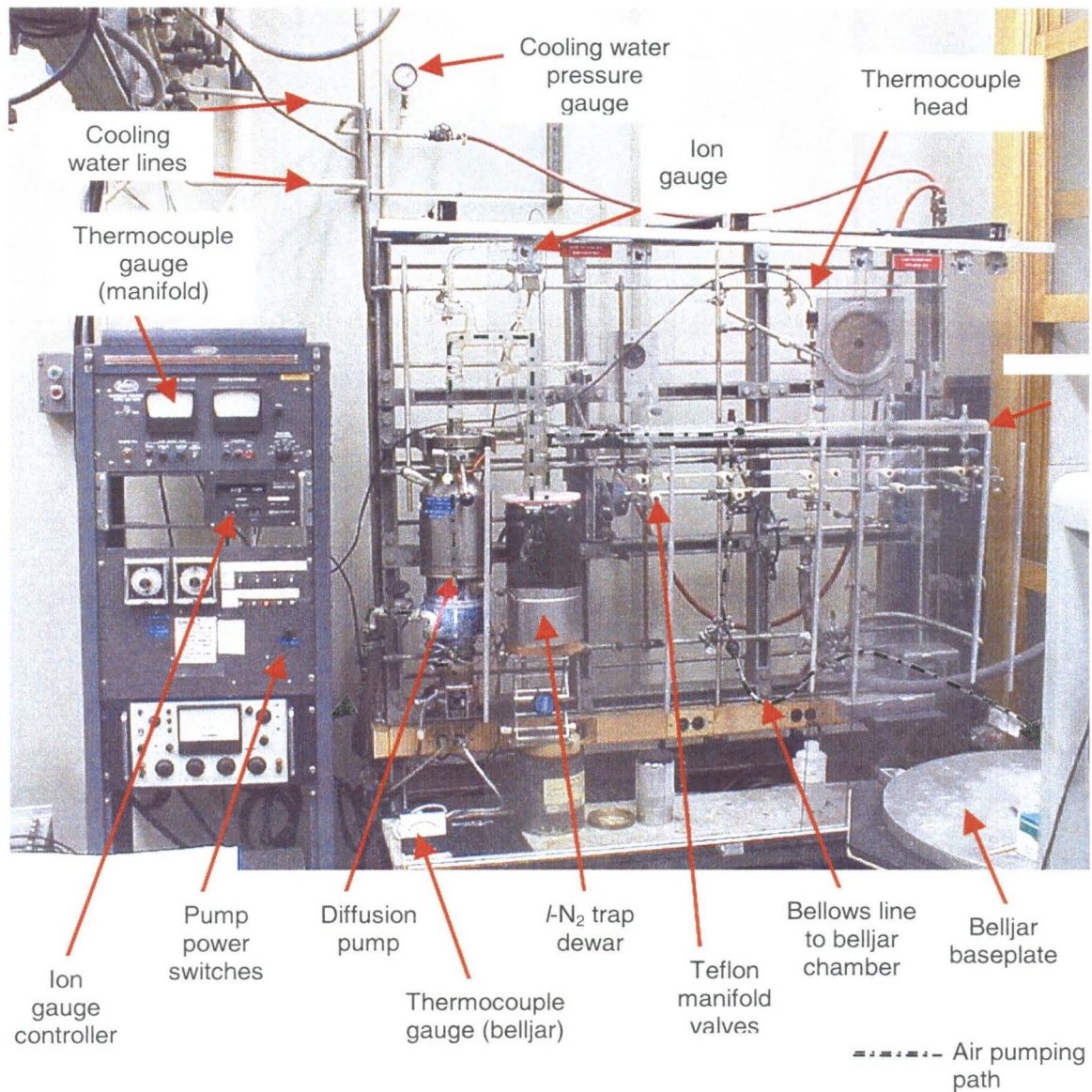
A.5 Vacuum System

Figure A.5 shows the vacuum manifold, used as a convenient conduit for pumping out the BOOMERANG belljar chamber. A 7 mm ID, 1 m long stainless-steel flex hose with a glass-joint end and a 2 3/4" conflat flange end connects one of the o-ringed glass manifold ports to the pipe (3/4 NPT) on the base of the belljar baseplate. A thermocouple-type pressure sensor mounts to the bottom of the baseplate, and measurements of pressures below 10^{-3} Torr are made by the manifold ion gauge. Vacuum epoxy seals all NPT pumping port connections.

The belljar baseplate incorporates several feedthrus to carry optical and electrical signals across the vacuum barrier. A fiber feedthru connects to a “tee” fitting where the

pumping pipe enters the baseplate, and is a compression-type hose fitting that incorporates a viton rubber ferrule with a hole $\sim 2x$ the diameter of the fiber jacketing to seal around the fiber. A floating-ground BNC feedthru on a 2 3/4" conflat flange carries rf to the coil, and isolates the magnet assembly and supports from the rf ground. A 3-port BNC feedthru on a 3 3/8" conflat flange is used to carry the fiber stage piezo actuator voltage and other signals, allowing for coaxial shielding throughout. A 10-pin bare-wire feedthru on a 2 3/4" conflat flange, and with an Amphenol 18-1S screw-on connector (on the air side), can carry assorted signals or power leads, such as thermocouple and heater leads for temperature feedback. See also section 3.1.G.

Figure A.5: Vacuum System for BOOMERANG Spectrometer.



Appendix B: BOOMERANG Microfabrication Process Flow

Starting Material

n-type (100), 1-10 Ω -cm, 4" diameter, 400 μ m thick, double-polished silicon wafer

1. Photolithography for Double-Side Align Marks

Spin AZ 5214 photoresist on both sides of wafer

Spin rate 2.5k rpm for 40 sec, soft bake 95°C, 2 min each coating

Mask 1: Double-side global align marks. Expose one side with Karl Suss MA6 1:1 double-side contact aligner for 7 seconds.

Develop 40 sec in 4:1 DI water/400K Developer

DI water rinse 2 min

Align to initial marks (now pointing down in MA6) and expose other side for 7 seconds using MA6 contact aligner

Develop 40 sec in 4:1 DI water/400K Developer

DI water rinse 2 min

Hard bake at 115°C for 2 min

O_2 plasma ash for 2 min at 0.5 Torr and 100W

2. RIE Align Marks

PlasMaster "fluorine" RIE - SF_6 30 sccm at 100 W and 40 mTorr chamber pressure (~4000 Å /min silicon etch). Etch 4 min each side of wafer

3. Strip Photoresist

Photoresist stripper at 75°C for 10 min

Acetone rinse for 3 min

IPA rinse for 3 min

DI water rinse for 2 min

O_2 plasma ash for 2 – 15 min at 100 - 250 W as needed

4. Pre-Diffusion (RCA) Clean

RCA1: ($H_2O + NH_4OH + H_2O_2$) in 5:3:1 ratio at 80°C for 10 min

DI water rinse in dump rinser for 5 min

RCA2: ($H_2O + HCl + H_2O_2$) in 4:1:1 ratio at 80°C for 10 min

DI water rinse in dump rinser for 5 min

H_2O/HF 10:1 dip (deglazing) for ~ 20 sec
DI water rinse in dump rinser for 5 min
12 MW spin dry

5. Oxidation

Oxide thickness 1.5 -2 μ m

Wet oxidation at 1050°C for 8-15 hrs 0.5 sccm O_2 , one drop of water per 5 sec

6. Photolithography for Trench Oxide Etch

Spin AZ 5214 photoresist on both sides of wafer

Spin rate 2.5k rpm for 40 sec, soft bake 95°C, 2 min each coating

Mask 2: 6x6mm die, trench 350 um deep – KOH etch GCA DSW projection aligner - expose front side of wafer 0.1 sec

Develop 40 sec in 4:1 DI water/400K Developer

DI water rinse for 2 min

Hard bake at 115°C for 2 min

7. Oxide Etch

Paint the edge of the wafer with PR to protect oxide and hard bake at 115°C for 5 min

Protect the frontside and edge of the wafer with blue tape before oxide etching.

10:1 BOE (10:1 NH_4F/HF) ~ 30 min, 1000Å / min

DI water rinse for 2 min and dry

8. Strip Photoresist

Photoresist stripper at 75°C for 10 min

Acetone rinse for 3 min

IPA rinse for 3 min

DI water rinse for 2 min

9. KOH Etch 350 μ m

1.44L 45% KOH + 1.76L $H_2O + 0.05L$ IPA 60°C for ~ 20 hrs or to get desired window thickness (50-200 μ m), 23 μ m/hr, 350 rpm stir bar

10. Remove Oxide

10:1 BOE ~ 30 min, 1000 Å / min
DI water rinse for 2 min and dry

11. Pre-Diffusion (RCA) Clean

RCA1: (H₂O + NH₄OH + H₂O₂) in 5:3:1 ratio at 80°C for 10 min
DI water rinse in dump rinser for 5 min
RCA2: (H₂O + HCl + H₂O₂) in 4:1:1 ratio at 80°C for 10 min
DI water rinse in dump rinser for 5 min
H₂O/HF 10:1 dip (deglassing) for ~ 20 sec
DI water rinse in dump rinser for 5 min
12 MW spin dry

12. Oxidation

Oxide thickness 1.5 - 2 µm
Wet oxidation at 1050°C for 8-15 hrs
0.5 sccm O₂, one drop of water per 5 sec
ALTERNATE - PECVD oxide deposition:
Frontside – 20W rf, 250°C substrate, SiH₄
150 sccm, N₂O 400 sccm, ~ 50 min at 380 Å/min dep rate.

13. Photolithography for Oxide Sacrificial Layer Pattern

Spin AZ 5214 photoresist on both sides of wafer
Spin rate 2.5k rpm for 40 sec, soft bake 95°C, 2 min each coating
Mask 3: Oxide sacrificial layer pattern (concentric rings) GCA DSW projection aligner - expose front side of wafer 1 sec
Develop 2 min in 4:1 DI water/400K Developer
DI water rinse 2 min
Hard bake at 120°C for 20 min

14. Oxide Etching

PlasMaster RIE CF₄/O₂ 40/8 sccm at 200 W and 40 mTorr chamber pressure for ~25 min (~600 Å /min)
ALTERNATE - BOE ~ 17 min
DI water rinse for 2 min and dry

15. Strip Photoresist

Photoresist stripper at 75°C for 10 min
Acetone rinse for 3 min
IPA rinse for 3 min
DI water rinse for 2 min
O₂ plasma ash for 2 – 15 min at 100 - 250 W as needed

16. Seed Layer Deposition

TSC or Sloan e-beam evaporation of Cr/Au (200/1000 Å, 100/500 may also be OK)
Deposit rate Cr - 2 Å/sec, Au - 5 Å/sec

17. Photolithography for Magnet Electroplating

Spin AZ 5740 photoresist on front side of wafer

Spin rate 2k rpm for 1 min,
Soft bake - ramp up to 100°C in convection oven (ramp at 200°C/hr)
Bake for 45 min and Ramp down

Wait until next day to allow rehydration of PR

Puddle chlorobenzene onto wafer and let stand for 1 min

Mask 4: PR mold for magnet plating
GCA DSW stepper - expose front side of wafer 10 sec

Mask 3: Oxide sacrificial layer pattern (concentric rings) GCA DSW projection aligner - expose front side of wafer 3 sec (ensures complete development of thick PR on magnet anchor sites)

Develop 45 min in 3:1 DI water/400K Developer

DI water rinse for 2 min

18. Electrodeposit Magnets

Thickness 6 - 12 µm (depending on PR depth)
material – 20:80 Fe/Ni, 50:50 Fe:Ni, 60:40 Co:Ni, or CoNiFe.... ?

19. Strip Photoresist

Photoresist stripper at 75°C for 10 min
DI water rinse for 2 min

20. Remove Seed Layer

Ion Mill at 250 V / 75 mA beam settings for 20 min, then adjust sample stage angle slightly and run again for 15 min; repeat a third time
Au etch rate = 140 Å/min, Cr etch rate = permalloy etch rate = 60 Å /min

21. Protect Front Side

Spin AZ 5214 photoresist on front side of wafer

Spin rate 2.5k rpm for 40 sec, soft bake 95°C, 2 min

22. Photolithography for Back Side Oxide Etching to Define Buttress

Spin AZ 5214 photoresist on back side of wafer

Spin rate 2k rpm, soft bake 100°C for 20 min

Mask 5: Buttress define

GCA 4800 stepper - expose back side of wafer 0.4 sec

Develop 40 sec in 4:1 DI water/400K Developer

DI water rinse for 2 min

Hard bake at 115°C for 2 min

23. Oxide Etch

10:1 BOE ~ 30 min (time depends on oxide type)

DI water rinse for 2 min and dry

24. Strip Photoresist

Photoresist stripper at 75°C for 10 min

Acetone rinse for 3 min

IPA rinse for 3 min

DI water rinse for 2 min

25. Photolithography for Si Beam Etch

Spin AZ 5740 photoresist on back side of wafer

Spin rate 3k rpm, soft bake 100°C for 20 min

Mask 6: Oscillator beam define

GCA 4800 stepper - expose back side of wafer 0.6 sec

Develop 2 min in 4:1 DI water/400K Developer

DI water rinse for 2 min

O₂ plasma ash for 2 min at 0.5 Torr and 100W

26. Wax Mount Wafer

Use orange dental wax and unpolished dummy wafer from STS operator, 130°C on Al foil on hotplate.

Thoroughly clean edges/bottom with razor and IPA before DRIE

27. Deep RIE to Define Beams (5 - 8 μ m)

STS DRIE etch 1.5 – 4 min (5 – 13 μ m)

Micron50 recipe - 70 W platen power, SF₆ 130 sccm for 8 sec, C₄F₈ 85 sccm for 5 sec, 600 W rf power
May need 90 W platen power if polymer islands form

28. Strip Photoresist

Photoresist stripper at 75°C for 10 min

Acetone rinse for 3 min

IPA rinse for 3 min

DI water rinse for 2 min

O₂ plasma ash for 2 – 15 min at 100 - 250 W as needed

29. Deep RIE to Define Ballasts (45 μ m)

12 - 15 min total etch time - STS recipe: micron50

Iterate – do 11 min etch, then look with alpha step and microscope before further etching

30. Wax Demount and Strip Photoresist

Remove dummy wafer at 130°C on hotplate

Photoresist stripper at 75°C for 10 -30 min

Acetone rinse for 3 min

IPA rinse for 3 min

DI water rinse for 2 min

Remove residual wax with 50°C TCE or alternative (Durasolv)

31. Dice

32. Remove Sacrificial Oxide

7:1 BOE tested up to ~ 8 hr w/o magnet damage, prediction for release is 5 hr for 60 μ m-wide beams

ALTERNATE - 49% HF tested up to ~ 1 hr, prediction is 14 min

If PECVD oxide is used for sacrificial layer, then etch rates will be ~ 10X faster.